UNDERSTANDING URBAN MICROMETEOROLOGY AND ITS IMPACT ON THE HEAT ISLAND OF GREATER KANPUR

A Thesis Submitted

In Partial Fulfillment of the Requirements

for the Degree Of

Master of Technology

in

Environmental Engineering and Management

by

Tirthankar Chakraborty

13117017

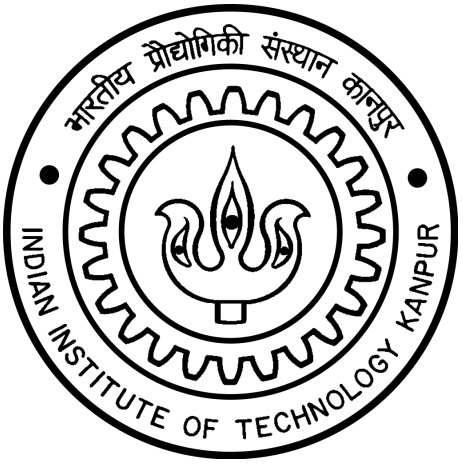

to the

Civil Engineering Department

Indian Institute of Technology Kanpur

May 2015

Declaration of Authorship

I, *Tirthankar Chakraborty*, declare that this thesis titled, *'Understanding Urban Micrometeorology and its Impact on the Heat Island of Greater Kanpur'* and the work presented in it are my own. I confirm that:

- This work was done wholly or mainly while in candidature for a research degree at this University.
- Where any part of this thesis has previously been submitted for a degree or any other qualification at this University or any other institution, this has been clearly stated.
- Where I have consulted the published work of others, this is always clearly attributed.
- Where I have quoted from the work of others, the source is always given. With the exception of such quotations, this thesis is entirely my own work.
- I have acknowledged all main sources of help.
- Where the thesis is based on work done by myself jointly with others, I have made clear exactly what was done by others and what I have contributed myself.

Signed: Tirthankar Chakraborty

Date: 5/5/2015

Certificate

It is certified that the work contained in the thesis titled, *'Understanding Urban Micrometeorology and its Impact on the Heat Island of Greater Kanpur'* by *Tirthankar Chakraborty* has been carried out under my supervision and that this work has not been submitted elsewhere for a degree.

Dr. S.N. Tripathi
Professor
Department of Civil Engineering
Indian Institute of Technology, Kanpur

"Research is formalized curiosity. It is poking and prying with a purpose."

Zora Neale Hurston

INDIAN INSTITUTE OF TECHNOLOGY KANPUR

Environmental Engineering and Management

Abstract

UNDERSTANDING URBAN MICROMETEOROLOGY AND ITS IMPACT ON THE HEAT ISLAND OF GREATER KANPUR

by Tirthankar Chakraborty

The urban heat island (UHI) effect for Kanpur, one of the largest cities in India, is studied and the major factors dictating its intensity determined for pre-monsoon and monsoon. In situ measurements show existence of a canopy heat island (UHI_{canopy}), with the night time temperature anomaly dominating for all seasons. The spatial coverage of the night time canopy and surface heat island ($UHI_{surface}$) effects are investigated through seasonal mobile campaigns and satellite data respectively. The urban micrometeorological parameters, like the surface fluxes and radiation components, are investigated in reference to a rural site, using site data and the NOAH Land Surface Model, to understand the differences in the energy budget with land use change. The results show that the UHI_{canopy} forms at night, mainly due to the difference in longwave radiation (both outgoing and incoming) between the urban and the rural sites. Though the correlation between the longwave radiation difference and the UHI_{canopy} persists throughout the day, albeit at a weaker level, the day time UHI_{canopy} is primarily a remnant of a night time phenomenon, with slight variations attributable to higher advection during the day and the difference in the resistance to convection between the urban and the rural site. The inter-seasonality of the UHI_{canopy} and $UHI_{surface}$ are largely controlled by the seasonal change in the land use of the rural site.

Acknowledgements

I would like to take this opportunity to thank those whose counsel and goodwill has facilitated this long and exciting journey.

First and foremost, I would like to sincerely thank my thesis supervisor, Prof. Sachchidanand Tripathi, whose knowledge, guidance and perpetual enthusiasm towards research has kept me motivated throughout this period. The kind of freedom he gave me during my thesis work was extremely conducive to my success and has rejuvenated my interest in research in general.

Thanks are also due to Prof. Shivam Tripathi for his illuminating recommendations and for helping me acquire the soil data required for my study. Additionally, I would like to express my gratitude towards the Hydraulics lab, the Earth Science lab and the Geoinformatics lab for providing both instruments and data used in this study; and also to Pravin Verma and Harishankar for maintaining the Weather Stations and helping out immensely during the mobile measurements.

A vote of thanks to all EEM faculty members for making my two years at IIT, Kanpur a memorable experience. In particular, Prof. Anubha Goel has been extremely encouraging, and I sincerely appreciate her counsel and support.

My heartfelt thanks to all the seniors in our group for providing their valuable suggestions and guiding me when I was stuck on a problem. A special mention to Mr. Chandan Sarangi, without whom my thesis would have been a fragment of its current self.

Our group acknowledges the Department of Science and Technology and the Ministry of Earth Sciences, Government of India for funding the work.

Last, but certainly not least, I would like to express my appreciation and gratitude towards my family, who fully supported my decision to pursue a career in research.

PS: I would also like to thank myself, for working a lot from time to time; and retract the self-acknowledgement for obsessively playing video games at other times.

Contents

List of Figures

List of Tables

Abbreviations

AATSR	Advanced Along-Track Scanning Radiometer
AWS	Automatic Weather Station
BREB	Bowen Ratio Energy Balance
CESM	Community Earth System Model
DBS	Dayanand Brajendra Swarup College (urban site)
EMC	Environmental Modeling Center
IGBP	International Geosphere Biosphere Programme
IITK	Indian Institute of Technology Kanpur (sub-urban site)
IMD	Indian Meteorological Department
JNV	Jawahar Navodaya Vidyalaya (rural site)
LST	Land Surface Temperature
MODIS	Moderate Resolution Imaging Spectroradiometer
NCEP	National Centers for Environmental prediction
NESDIS	National Environmental Satellite Data and Information Service
NWS	National Weather Service
ORA	Office of Research and Applications
OSU	Oregan State University
RMSE	Root-mean-square error
SSiB	Simplified Simple Boisphere model
SWB	Simple Water Balance model
UCAR	University Corporation for Atmospheric Research
UHI	Urban Heat Island
$\mathbf{UHI_{canopy}}$	Canopy heat island
$\mathbf{UHI_{surface}}$	Surface heat island
USGS	United States Geological Survey
WMO	World Meteorological Organization

Physical Constants

Thermal conductivity of liquid water	K_{liq}	=	0.57 W/m/K (NOAH)
Thermal conductivity of ice	K_{ice}	=	2.2 W/m/K (NOAH)
Thermal conductivity of quartz	K_{qtz}	=	7.7 W/m/K (NOAH)
Thermal conductivity of other soil components	K_o	=	2 W/m/K (NOAH)
Specific heat capacity of solids in soil	C_{soil}	=	$2 \times 10^6 J/m^3/$ (NOAH)
Specific heat capacity of water	C_{liq}	=	$4.2 \times 10^6 J/m^3/$ (NOAH)
Specific heat capacity of air	C_a	=	$1004.5 J/m^3/K$ (NOAH)
Ratio of molecular weight of water vapour to that of air	ε	=	0.622
Latent heat of vaporization of water	λ	=	$2.26 \times 10^6 J/Kg$
Specific heat capacity of dry air	C_{pd}	=	1006 J/kg/K

Symbols

T_s	Land surface temperature or skin temperature	°C or K
C	1st coefficient derived from MODTRAN 4 simulations	dimensionless
A_1	2nd coefficient derived from MODTRAN 4 simulations	dimensionless
A_2	3rd coefficient derived from MODTRAN 4 simulations	dimensionless
A_3	4th coefficient derived from MODTRAN 4 simulations	dimensionless
B_1	5th coefficient derived from MODTRAN 4 simulations	dimensionless
B_2	6th coefficient derived from MODTRAN 4 simulations	dimensionless
B_3	7th coefficient derived from MODTRAN 4 simulations	dimensionless
T_i	Top of the atmosphere brightness temperature in ith channel	°C or K
T_j	Top of the atmosphere brightness temperature in jth channel	°C or K
e_i	Land surface emissivity in ith channel	dimensionless
e_j	Land surface emissivity in jth channel	dimensionless
e	Averaged land surface emissivity in the two channels	dimensionless
Δe	Land surface emissivity difference between the two channels	dimensionless
H	Sensible heat flux	W/m^2
LE	Latent heat flux	W/m^2
R_{net}	Net radiation flux	W/m^2
G	Ground flux	W/m^2
C_h	Surface exchange coefficient for heat	m/s
ρ	Density of air	kg/m^3
C_p	Specific heat capacity of air at constant pressure	$J/m^3/K$
u	Wind speed	m/s
T_a	Air temperature	°C or K
Θ_a	Potential temperature of air	°C or K
K_h	Thermal conductivity of soil	W/m/K

T_{s1}	Temperature of the first soil layer	°C or K
K_e	Kersten number	dimensionless
K_{sat}	Thermal conductivity of saturated soil	W/m/K
K_{dry}	Thermal conductivity of dry soil	W/m/K
γ_d	Density of dry soil	kg/m^3
sm	Moisture content of soil	m^3/m^3
sm_{sat}	Moisture content of saturated soil	m^3/m^3
sm_{liq}	Liquid water content in soil	m^3/m^3
sm_{ice}	Frozen water content in soil	m^3/m^3
qtz	Fractional quartz content in soil	dimensionless
E_{dir}	Direct evaporation from soil	W/m^2
E_c	Evaporation from canopy	W/m^2
E_t	Transpiration	W/m^2
E_{snow}	Direct sublimation from snowpack	W/m^2
E_p	Potential evapo-transpiration	W/m^2
Δ	Slope of saturated vapour pressure curve	Pa/K
C_q	Surface exchange coefficient for water vapour	m/s
q_{sat}	Specific humidity of saturated air	kg/kg
q	Specific humidity of air	kg/kg
f_c	Vegetation fraction	dimensionless
sm_1	Moisture content of 1st soil layer	m^3/m^3
sm_{dry}	Wilting point of soil	m^3/m^3
f_x	Empirical factor for calculation of direct soil evaporation	dimensionless
cmc	Actual canopy moisture content	kg/m^2
cmc_{max}	Maximum canopy moisture content	kg/m^2
f_{sn}	Fractional snow coverage	dimensionless
P_c	Plant coefficient	dimensionless
R_r	Empirical function for plant coefficient formulation	dimensionless
R_c	Canopy resistance	s/m
R_{cmin}	Minimum stomatal resistance	s/m
$R_{c,min}$	Minimum stomatal resistance	s/m
LAI	Leaf Area Index	m^2/m^2
RC_{rad}	RC factor in terms of incoming solar radiation	dimensionless
RC_{temp}	RC factor in terms of temperature	dimensionless

RC_{hum}	RC factor in terms of humidity	dimensionless
RC_{soil}	RC factor in terms of soil moisture	dimensionless
$R_{c,max}$	Maximum stomatal resistance	s/m
S_i	Incoming shortwave radiation	W/m^2
R_{gl}	Optimum transpiration solar radiation	W/m^2
T_{opt}	Optimum transpiration air temperature	°C or K
h_s	Optimum transpiration relative humidity	%
n_{root}	Number of root layers	dimensionless
sm_i	Moisture content of ith root layer	m^3/m^3
$sm_{i,wlt}$	Wilting point of ith root layer	m^3/m^3
sm_{ref}	Threshold moisture content for transpiration stress	m^3/m^3
f_i	Fraction of root depth in ith layer	dimensionless
D	Soil water diffusivity	m^2/s
K	Hydraulic conductivity of soil	m/s
S	Source of sink term for soil moisture	$/s$
C	Specific heat capacity of soil	$J/m^3/K$
f_{soil}	Volumetric fraction of solids in soil	m^3/m^3
f_{liq}	Volumetric fraction of water in soil	m^3/m^3
f_a	Volumetric fraction of air in soil	m^3/m^3
k_h	Eddy diffusivity for heat	m^2/s
T	Temperature	°C or K
z	Height	m
E	Water vapour flux density	$kg/m^2/s$
k_v	Eddy diffusivity for vapour	m^2/s
ρ_v	Vapour density	kg/m^3
P	Atmospheric pressure	Pa
P_v	Vapour pressure	Pa
RH	Relative humidity	%
T_a	Air or canopy temperature	°C or K
P_{vs}	Saturated vapour pressure	Pa
β	Bowen ratio	dimensionless
γ	Psychrometric constant	Pa/K

Dedicated to the hours spent and the knowledge gained...

Chapter 1

Introduction

1.1 Problem background

The positive temperature difference between a city and its hinterland - the UHI effect - is one of the most pervasive topics in urban climatology. Though the research area has been active for well over a century, the complexities of micrometeorological interactions, heterogeneity of urban zones and a multitude of factors that may affect such temperature anomalies have made understanding and modelling the phenomenon challenging.

Researchers attribute the higher temperatures in urban zones to several factors: a lack of vegetation, which reduces evaporative dissipation of heat; the lower albedo of urban surfaces, which increases the net incoming solar radiation; the higher specific thermal mass of concrete and asphalt, which leads to more reradiated heat during night time; and the addition of anthropogenic heat from human activities. Most studies report the UHI magnitude for different cities and remain qualitative in their explanations, which cannot be used to develop proper mitigation techniques.

1.2 Problem statement

1.2.1 Objective of study

A systematic study on the effect of micrometeorological interactions on the thermal anomaly of an urban area in the modified humid subtropical climate zone has not been attempted in the past. Kanpur city represents a typical case of such an urban conglomerate. Thus, the main purpose of this study is to quantify the temporal and spatial variation of the UHI_{canopy} and $UHI_{surface}$ over Greater Kanpur and understand the micrometeorological factors responsible for this phenomenon.

1.2.1.1 Research questions

What is the magnitude of the urban heat island effect over Kanpur city? What are the main factors responsible for this phenomenon? Specifically, how well can micrometeorological interactions explain the diurnality and inter-seasonality of this effect?

1.2.1.2 Sub questions

How well does the NOAH Land Surface Model simulate the hydrological and micrometeorological parameters over two distinct land types in the Indo-Gangetic basin? How does the urban-rural and intra-urban energy partitioning vary?

1.3 Thesis overview

A comprehensive review of the urban heat island literature, and studies on urban climatology pertaining to this topic, have been given in chapter 2, both for India and the world.

The metadata relevant to the study area and the sites used in the work has been detailed in chapter 3.

Chapter 4 gives a thorough overview of the instruments and data processing techniques used in the study. It also explains the importance of the surface energy balance on meteorological parameters, and provides the descriptions of the model (NOAH) and method (BREB) used to estimate this for the study area.

The results are presented and the different aspects of the work are discussed in chapter 5.

Finally, chapter 6 gives a synopsis of the study, its limitations and its future possibilities.

Chapter 2

Literature review

2.1 Urban heat island effect - World

The urban heat island (UHI) effect, the localized thermal anomaly over urban areas compared to nearby rural ones, is a well-known consequence of urbanization on local climate. The phenomenon was first coined over a century back [45], and has, since then, evolved into one of the principal research areas in urban climatology. The difference in air temperature between the urban and rural zone is usually referred to as the $\mathrm{UHI}_{\mathrm{canopy}}$, while the surface temperature difference, usually studied using remotely sensed data, is termed as the $\mathrm{UHI}_{\mathrm{surface}}$.

The current review tries to bring together the important studies relevant to the field, as performed throughout the world. The review of the world's UHI effect will exclude studies not written in English and unpublished works. Multiple UHI studies on the same city will also be avoided, as will simple reports on the UHI magnitude, unless the study brings into effect a different methodology or a conclusion that changed the field significantly. Studies pertaining to Indian cities will be in the next section

of the review, unless they are more general studies investigating the consequences of urbanization. Some studies representing distinct methodologies used to understand the UHI effect and its factors are also discussed.

The bulk of the studies on the UHI phenomenon are qualitative, with most studies reporting on the magnitude of the UHI, may that be the UHI_{canopy} or the $UHI_{surface}$. The pioneering work on the subject, as mentioned earlier, was by Luke Howard in 1833, where the temperature in and around the city of London was found to be distinctly higher than that of the surrounding countryside. Since then, UHI studies have been published on hundreds of cities around the globe, with studies for almost every major city of North America, Europe and East Asia [18, 24, 37, 47, 56, 121, 124, 129]. The majority of these studies, however, have been constrained to simple observations of the urban-rural temperature differences through various methods, from weather station observations, to mobile surveys to satellite imagery. This has led to an exponential growth in the field of urban climatology, with not enough improvement in the underlying science dictating the phenomenon. Furthermore, proper quantification of the factors generating the UHI for a city has been difficult, owing to a number of competing influences to be considered [11]. Consequently, the relative importance of said influences has not been quantified as a general rule for all city types, partly because of the significance of urban morphology and background climate on UHI formation, a fact established by several empirical studies [44, 52, 55, 75, 115, 125].

After Howard's revolutionary work, it was Oak who pointed out the importance of the investigation of processes that influence the UHI, rather than descriptive studies, which were dominating the literature at that time [83]. He also gave a comprehensive report on the possible factors influencing the UHI [86]. Additionally, the future direction of the research in the field was chalked out in the paper. The study on

the UHI, and urban climatology in general, has brought together a wide variety of disciplines, including, but not limited to, physics, meteorology, climatology, geosciences, geography, ecology, hydrology, environmental science, engineering, building and landscape architecture, building science, social science and town planning. This has created an inconsistency in the UHI literature, with different terminologies being used to describe the same effect along with many disparities in methodology. The issue of the UHI also involves several scales, both temporal and spatial. In a future study, Oak pointed out the importance of the unification of the terminology, symbols and methodology in the field [87]. Stewart's systematic critique of the literature [116] demonstrated that approximately half of the UHI magnitude reports lack robustness. A significant number of studies do not control for weather factors and do not provide sufficient metadata about the instrumentation and field characteristics during the study period, thus indicating poor scientific practice. In the same vein, Peterson and Owen established the importance of the metadata used in UHI studies [98].

The urban climatology literature is vast, with thousands of studies on hundreds of cities in the world. The UHI has been quantified for the almost all major cities in the western world. A chronological summary of the major reviews in urban climatology, at both the world and regional level, is given in the Table below (Table 2.1).

Some recent meta-analyses and studies comprising of multiple cities have indicated some general factors that may be causing the thermal anomaly (both at the canopy and at the surface level) over cities. A study involving 419 global cities was performed using MODIS datasets, and the diurnal and seasonal variation in the $UHI_{surface}$ was investigated in the context of biophysical and socio-economic factors [96]. The researchers found that the day time $UHI_{surface}$ was, on average, higher than the night time values, with no significant correlation between the two. The distribution

of the night time $UHI_{surface}$ was correlated to the difference in albedo and night time light between the urban and the suburban areas. The distribution of day time $UHI_{surface}$ was negatively correlated with the vegetation cover difference between the two areas. The researchers concluded that increasing vegetation cover could be an effective means to control the UHI effect. Another study published in Nature attempted a numerical understanding of the factors responsible for the phenomenon, challenged conventional wisdom, and made significant contributions in determining the most effective techniques for moderating the effects of UHI [137]. For the study, the researchers used satellite data over 65 cities in the United States and Canada and the Community Earth System Model (CESM) to evaluate the effects of the various factors on the UHI magnitude for days and nights. The results contradicted the accepted notion that a lack of evaporation was the primary cause of urban heating. Instead, the model showed that the heating and cooling of an urban area during the day is primarily a function of its aerodynamic smoothness, which may be higher or lower than the surrounding rural landscape depending on the city. If a city is aerodynamically smoother than its surroundings, the convection rate is lower, thus reducing the heat dissipation from the city core; while an aerodynamically rougher city will cool faster than the countryside. The paper addressed several discrepancies in the urban climatology literature, which was previously replete with cases where the urban area was cooler than nearby rural areas during the day. Earlier, this was justified by referring to the non-representative nature of weather stations or the effect of urban cool pockets (like city parks, which are cooler than the surrounding cityscape). The reasons given in this paper are more consistent and have been verified using long-term data. To assess the effect of different mitigation techniques on the temperature anomaly, the Community Earth System Model was run for a 60-year period and reduction in the UHI magnitude was observed for different initial conditions. The researchers concluded that changing the heat capacity of

urban materials or the atmospheric roughness would require a complete overhaul of the urban structure, which is not feasible. Using different materials in building roofs to increase the urban albedo demonstrated the greatest impact at the least cost. Another metastudy investigated the UHI for 101 Asian cities by examining 88 articles and papers [106]. The researchers found that the main factors influencing UHI magnitude, as seen in the aggregate of the studies analyzed, were synoptic conditions, precipitation and humidity, cloud cover and wind speed, city size, urban morphology and coastal effects. Even though huge contributions have been made in recent years towards the understanding of this complex phenomenon, there is a need to determine the validity of these explanations in other geographic locations.

The ramifications of the UHI effect are varied and case sensitive. The summary below is not meant to be exhaustive but to provide a representative cross-section of the literature. The most pertinent effect of the UHI is on power demand, the nature of which depends on the city in question. A wide array of studies have been performed to evaluate the possible effects of urban climate on energy demands. For London, researchers found that the annual urban heat stress increased urban cooling load by 25%, while reducing annual urban heating load by 22% [57]. Similarly, in Greece, the annual cooling load was doubled, accompanied by a 30% drop in the annual urban cooling load [107]. Another adverse effect of the UHI is its relation and interaction with pollution islands, which can further increase contribution of human activity to both local and global emissions [28, 46, 51]. In hot and arid communities, the localized temperature surge can exacerbate heat-stress related deaths and significantly increase water consumption among residents [41, 43]. The UHI effect has also been linked to precipitation [54, 62], though that correlation has been hard to establish. Niyogi and his group investigated the impact of urban and land vegetation

interactions on the evolution of mesoscale convective systems and found a significant correlation between the two in their model simulation [81]. Similarly, a recent study on forty urban conglomerates in India from IIT, Bombay found that though there is a tendency towards decreasing precipitation in the country, extreme rainfall events are enhanced around urban areas [108]. The effect of the UHI effect on global warming has, however, been found to be small [49]. The bulk of the studies suggest that an understanding of the UHI phenomenon, especially the factors leading to its formation, can not only improve scientific understanding of micrometeorology and urban climatology, but also help inform public policy making in order to mitigate these harmful effects. With 54% of the world's population living in urban regions in 2014, which is expected to increase to 66% by 2050, a strategy to restrict these consequences of urbanization can benefit a lot of people in the years to come [126].

TABLE 2.1: Major reviews in urban climatology

Year	Topic
1979 [85]	Review of urban climatology, 1973–76
1980 [84]	Bibliography of urban climate literature, 1977–80
1981 [59]	Multiple topics in urban climatology
1981 [60]	Multiple topics in urban climatology
1983 [32]	Urban climates
1983 [64]	Bibliography on the climate of metropolitan areas
1984 [61]	Multiple topics in urban climatology
1986 [88]	Urban climatology in the context of tropical areas
1990 [112]	Progress report including urban climates
1990–91 [133]	Emphasis on Japanese urban climate work
1991 [19]	Section on urban climatology
1992 [25]	Climate change in urban areas
1995 [21]	Wind patterns in cities
1995 [38]	Review of Israeli urban climate work
1998 [8]	Review of urban climate studies from 1996 and 1997
1998 [118]	Urban climate processes and their mitigation
1998 [65]	Urban effects on precipitation
2000 [9]	Review of urban climate studies from 1998
2000 [103]	Atmospheric turbulence in urban areas
2001 [10]	Review of urban climate studies from 1999 and 2000
2003 [11]	A Review of Turbulence, Exchanges of Energy and Water, and the Urban Heat Island
2007 [104]	Review of urban climate studies in subtropical regions
2008 [102]	A review on the generation, determination and mitigation of Urban Heat Island
2012 [105]	Review and assessment of urban heat island research in Singapore
2013 [132]	Review of World Urban Heat Islands and their link to Increased Mortality
2013 [35]	A review of strategies to mitigate adverse effects of urban heat islands
2014 [80]	A review of the assessment of urban heat island using satellite remotely sensed imagery
2015 [106]	Analyzing the heat island magnitude and characteristics in one hundred Asian and Australian cities and regions

2.2 Urban heat island effect - India

For India, the review has tried to include every available study explicitly examining the UHI effect for different cities in the country.

The number of studies on the UHI effect in India have been few and far between. Moreover, a high percentage of studies, especially the earlier ones, were constrained to reporting on the UHI magnitude using different methods. The first traceable study on the UHI effect in the country was conducted for Pune and Bombay in 1973 [68, 76, 89]. The next batch of studies were conducted in the 1980s over the national capital territory of India, Delhi [13, 77, 90]. These studies were descriptive in nature, relying on different data sources to quantify the UHI of the metropolis; and established the existence of warm and cool pockets in the urban fabric. The UHI intensities observed were variable, somewhere between 0.6 °C and 11 °C and the magnitude and extent of the warm pockets was suggested to be a function of the urban morphology, urban wind speed, cloudiness and vegetation cover. Some more preliminary observations on the UHI of many cities in India, including Calcutta, Mumbai, Bhopal and Vijaywada, were presented at the World Meteorological Organization's conference on urban climatology [88]. The next study was performed for the city of Madras [119]. In this study, surface temperature, wind speed and humidity data were collected within the city using mobile measurements. A total of 77 data points were used and the experiments were run for 8 days over three different routes. The study showed that the isotherms had a tendency to follow the coast and that the heat pockets had lower humidity values. A similar study was performed for the city of Pune a decade later, with mobile surveys conducted over 9 routes for 2 consecutive days to find a precise representation of the spatial distribution of the temperature anomaly [29]. The study established that the UHI was dominant during the night. Following this, satellite imagery became the norm for studying UHI in India, with the first studies

describing the night time spatial thermal anomalies for Hyderabad using Advanced Along-Track Scanning Radiometer (AATSR) datasets [12, 23]. The studies also evaluated that the satellite-derived surface temperatures were close to the ground measurements.

The next decade saw an upsurge in UHI studies in the country, with a number of studies centered around the national capital territory of India. A study in the city of Visakhapatnam found that the winter season had a higher UHI magnitude compared to pre-monsoon and monsoon [31]. Similarly, a later study in Chennai confirmed the same seasonality of the effect [30]; a stark contrast to the studies done for Indian cities in Northern India, where pre-monsoon shows the highest UHI magnitude [17, 74, 92, 110]. Noteworthy contributions have been made towards the quantification of the UHI effect of Delhi in the past five years, primarily due to Professor Mohan and her group. Long term trends in Delhi's air temperature over different land use types, as well as the spatial variability of air temperature over Delhi have been well-established, both through micrometeorological measurements, as well as satellite data [22, 70–74, 93]. Furthermore, some important conclusions have been derived from these studies. Delhi is cooler than the countryside during the day and warmer at night. The UHI of Delhi is strongly affected by the particular matter concentrations in the region, as well as the AOD. The variability in the spatial distribution of Delhi's UHI was also found to be quite high and dependent on the land type of the immediate surface. The same period also saw observations on the UHI effect around Bangalore [101], Kochi [122, 123], Thiruvananthapuram [7] and Jaipur [42]. A synopsis of the UHI magnitude measured for different cities in the country is given in Table 2.2.

TABLE 2.2: UHI intensities for Indian cities

City	Urban heat island magnitude	Reference
Bangalore	4°C	[101]
Chennai	3.35 °C to 4 °C	[30]
Delhi	4°C to 10.7 °C	[13, 22, 70–74, 77, 90, 93]
Guwahati	Maximum of 2.29	[17]
Hyderabad	NA	[12, 23]
Jaipur	NA	[42]
Kanpur	Maximum of 8.8 °C (pre-monsoon) Maximum of 6°C (monsoon)	Present study
Kochi	2.5°C to 4.6°C	[122, 123]
Kolkata	4°C	[88]
Mumbai	4.3°C	[76]
Pune	2°C to 10°C	[29, 68, 89]
Thiruvananthapuram	2.4°C	[7]
Vishakhapatnam	2°C to 4°C	[31]

Though the UHI literature is vast, the number of studies performed on the topic in India have been minimal, with most of them still concentrating on reporting the UHI magnitudes. Moreover, a systematic understanding of the factors influencing the phenomenon in the country is missing. Modelling studies where the thermal anomaly is investigated in the context of land-surface interactions is another open area. Lastly, no study has been attempted on the UHI of Kanpur city, which is an important metropolis in the country and a representative area in the Indo-Gangetic Basin. Thus, the current study is important, both in the context of quantifying the UHI of the city, and also to understand how urbanization affects the near-surface atmospheric dynamics in this climatic zone.

Chapter 3

Site description

3.1 Kanpur city

Kanpur city (26.5°N 80.3°E), with an area of 605 km^2 and a population of 2.5 million people [127], is one of the most polluted cities in India. Situated on the bank of the Ganges, the city contains some of the largest tanneries in the world, which has led to its nickname, "Leather City of the World". Kanpur experiences a humid subtropical climate, modified by monsoonal effects, with long and scorching pre-monsoons (March to June), a prolonged rainy (monsoon) season (July to September) and short winters (December to February) [109]. Temperatures can fluctuate wildly, going from almost 0.0 °C during winters to 47.0 °C during pre-monsoons [48]. The humidity remains high for majority of the year, but may reach values as low as 10% during early pre-monsoon. Kanpur was one of the major centers of the industrial revolution in India. During the last century, the city has developed with little planning, and represents a typical case of extreme urbanization.

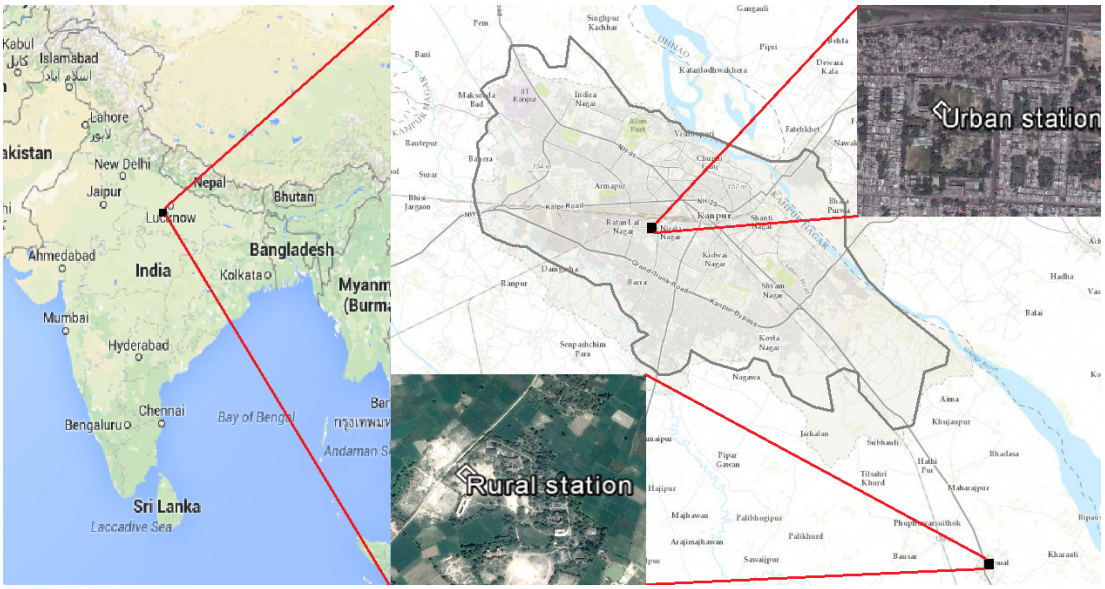

FIGURE 3.1: Location of Automatic Weather Stations

In the present study, two Automatic Weather Stations, one in the urban core (DBS) and another in a rural area (JNV), are used to measure air temperature, humidity, precipitation, wind speed, wind direction, the four components of solar radiation, surface albedo, skin temperature, soil temperature and soil moisture. The relative position of the two sites with respect to the city along with their land use type are given in Figure 3.1. Pressure measurements are available from another nearby weather station (26.52°N 80.23°E) and assumed to be valid for both the sites, since the site is within 40 kms of the two stations used for the study. Both the sites comprise of similar, grassy surfaces to negate the influence of the immediate surface type on the measured variables. However, the areas surrounding the weather stations are different, with the DBS site representing a typical urban conglomerate while the rural site representing a farmland. This disparity can give a good idea about how the land-atmosphere interactions differ for the two distinct cases and how that affects urban climate, specifically how it controls the city's UHI.

3.1.1 DBS

The urban site is situated on the playground of the Dayanand Brajendra Swarup College (DBS), which is in the heart of the city and is surrounded by a dense residential section. The surface underneath the AWS is grassy. It is understandable that the location of the urban site, given the immediate grassy surface underneath the weather station will lead to slight errors in the UHI_{canopy} magnitude of the city as a whole, since the grassy surface cannot perfectly represent the heterogeneous urban landscape. This is not a major issue since the study is concerned with the trends in the UHI effect (both diurnal and seasonal). Additionally, the sites were chosen to acquire all the parameters required to run the NOAH LSM. The spatial study partly compensates for this constraint in site selection and gives a complete picture of the seasonal night time UHI_{canopy} and the seasonal day time and night time $UHI_{surface}$ over the urban conglomerate. The soil type of the urban region is silty clay.

3.1.2 JNV

The rural site is 32 kms away from the city core, and is situated in a field in a rural school, Jawahar Navodaya Vidyalaya (JNV). The surface and soil type are both similar to that of the urban site.

Chapter 4

Methodology

4.1 Temporal study

4.1.1 Data collection

The Automatic Weather Stations at each site are identical. A schematic of the AWS at each site is given in Figure 4.1. The sensors mounted on the AWS send the summarized measured data at programmable intervals of 0.1/1/2/5/10/15 minutes. At these sites, the sensors are programmed to measure data every 15 minutes and data was collected from August, 2013 to February, 2015 for the purpose of the present study. The digital serial output from the sensors are interfaced with a micro-controller, which then gets stored in a data logger, from where it can either be manually retrieved or sent to a central server through GPRS. In case of non-availability of GPRS signal, SMS is used to broadcast the output. In the extreme case of no mobile signal, data is stored in the internal 1 GB memory unit. The standalone wireless AWS unit is powered by solar panels. Solid alkaline batteries

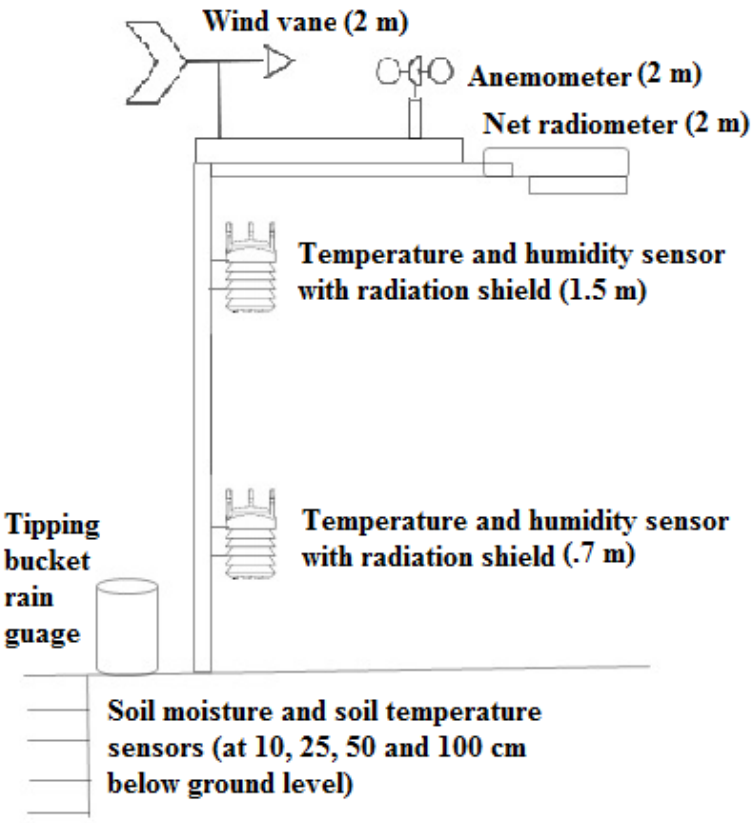

FIGURE 4.1: Schematic of Automatic Weather Stations

are used at the sites to ensure consistent power supply. The sensors can function for a week if the batteries are fully charged.

4.1.2 Instrumentation

Two iNGEN iTMS101 temperature sensors were used to measure air temperature at the two heights (0.7 m and 1.5 m) for each site. The sensors are silicon bandgap sensors with a resolution of .01 °C and an accuracy of ±0.2 °C when kept inside radiation shields, which they were at these sites. The sensors have a response time of 1 second and an operational range of -40°C to +120°C.

Two iNGEN iHMS101 solid state thin film capacitive relative humidity sensors were used at each site with an accuracy of ±3% with a resolution of 0.03%. Like the temperature sensors, the response time for the RH sensors is 1 second.

A standard tipping bucket rain gauge, with a resolution of .2 mm, measured the precipitation.

Wind speed and wind direction measurements were performed at 2 m from the ground surface. The iNGEN iWMS1013 optically scanned cup anemometer (wind speed sensor), used at each site, has an operating range of 0 to 60 m/s, a resolution of 0.1 m/s and an accuracy of ±0.5 m/s.

The iWMS1021 propeller wind vanes used at each site have an accuracy of ±5° , with a resolution of 1° .

Soil temperature and soil moisture were measured at 4 depths (10 cm, 25 cm, 50 cm and 80 cm) at both sites. Four WatchDog 3667 external soil temperature sensors, with an accuracy of ± 1° C, measured the soil temperature.

Four WaterScout SM 100 soil moisture sensor, with an accuracy of ±3% volumetric water content (VWC) and a resolution of 0.1% were set up at each AWS. Unlike the temperature, humidity, wind and precipitation sensors, the data for the soil sensors cannot be retrieved automatically; so, were retrieved manually every three months.

Two Kipp & Zonen CNR4 Net Radiometers, mounted at heights of 2 m, were used to measure the four components of solar radiation, the skin temperature and the surface albedo. The device consists of a pair of pyranometers, one facing upward and the other downward. Two pyrgeometers are also present in a similar configuration. The pyranometers measure shortwave radiation, while the pyrgeometer modules measure longwave radiation. The CNR4 has integrated sun shields to moderate thermal

effects on both longwave and shortwave radiation measurements. The albedo of the surface is calculated from the ratio of outgoing and incoming shortwave radiation, while the Stefan–Boltzmann law is used to derive the skin temperature from the emitted longwave radiation. The device has a shortwave spectral range of 300 to 2800 nm, a long wave spectral range of 4500 to 42000 nm and a sensitivity of 5 to 20 μ V/W/m^2.

4.1.3 Data processing

Though the sensors provided by iNGEN technologies have a relatively small percentage error for temperature ($\pm$ 0.2%) and humidity($\pm$ 3%), the sensor sensitivity does deviate with time. Thus, periodic calibrations become important, both to assess the performance of the field sensors and to correct the data, if necessary. To calibrate the temperature and humidity sensors, Vaisala HMT 330s have been used. For the upper sensors, calibrations were done almost every month from January to September. Corrections were made for each month based on that month's or a nearby month's calibration equation. For the periods before and after this period, the overall calibration equations were used to correct the data. For the lower sensors, only one calibration was done, in August. An overview of all calibrations done for the study are given in Appendix A.

The study for pre-monsoon and monsoon was done using only 2014's data, since it had been calibrated and corrected more rigorously. For post-monsoon and winter, since overall calibration equations were used, data was used from both 2013 and 2014. For surface temperature, data was only available for 2014.

The tipping bucket rain guages were manually calibrated by pouring a pre-defined volume of water into the bucket and comparing that with the sensor output.

The CNR4 Net Radiometer is factory-calibrated from Kipp & Zonen at the time of its manufacturing with necessary corrections applied to individual units to derive its sensitivity.

4.2 Spatial study

4.2.1 Measurement campaigns

4.2.1.1 Data collection

Mobile observations were carried out in the months of May (pre-monsoon), June (pre-monsoon), September (monsoon) and January (winter) to measure the air temperature in and around Kanpur city. A total of four campaigns were undertaken, one on 23rd March, 2014, one on 6th June, 2014, one on the cloudy, monsoon night of 5th September, 2014 and one during winter on January, 28th, 2015. Two vehicles were driven at a constant speed of 40 km/hr, while measuring temperature, humidity and GPS data every 90 seconds. The measurement campaigns were carried out at night, from 10 pm to 6 am, when the temporal variation in temperature is minimal. The routes were chosen such that the horizontal and vertical extent of the city got covered (Appendix B). For three reasons, day time campaigns were not attempted. Firstly, the temporal variation in temperature during the day is vast, thus making it hard to filter out the effect of this on the spatial representation. Secondly, the temporal analysis showed that the day time UHI effect is low compared to night time. Thus, more motivation was there to study the night time aspect of the phenomenon. Lastly, day time measurements can be affected by vehicle exhausts and traffic, thus making it unfeasible.

4.2.1.2 Instrumentation

To measure the temperature and RH during the mobile campaigns, two Vaisala HMT330s were used. The temperature module has an accuracy of ±0.2°C, while the thin film capacitor RH module has an uncertainty of ±1.0 %RH.

A Garmin GPS device is used to measure the latitude and longitude of locations during the measurement campaigns.

4.2.1.3 Data processing

The Vaisala HMT330s are factory calibrated and do not need further calibration. However, since one Vaisala sensor was older than the other, the two sensors were correlated and the older was corrected based on this correlation (Appendix C). This was done to ensure consistency in the data set. The measurement campaigns were performed for almost 8 hours for each night. Thus, the temporal variation in night time air temperature, though minimal, must be taken into account before using the data. To abate this effect, the data set was corrected based on temperature trends from the fixed stations for each campaign. For regions traversed within the urban boundary, the urban station data were used, while the rural station data were used for those outside the city.

4.2.2 MODIS derived surface temperature

4.2.2.1 Overview of satellite remote sensing and the MODIS sensor

Satellite imagery has made collection and analysis of data for large spatial scales accessible and easy. Before the advent of the use of satellites to collect data, scientists

had struggled with the data requirements for studies on regions without ground-based observations, especially those in developing countries and in uninhabitable locations. This has particularly affected those scientists involved in atmospheric, oceanic and land studies. The availability of different satellite remote sensors that collect data all over the globe on a regular basis has made these a primary source of uninterrupted, consistent information on a vast variety of temporal and spatial scales. The potential of these satellites in various disciplines has been well-realized, and they have been incorporated in many areas of research and application, from the atmospheric sciences, to environmental sciences, to infrastructure planning, to many others.

The Moderate-resolution Imaging Spectroradiometer (MODIS) is a scientific sensor on board the Terra and Aqua satellites launched by NASA in the early 2000s. The sensors are designed to provide global observations every two days at a spatial resolution of 250 m to 1 km. They have 36 spectral bands, between 0.405 μm and 14.385μm. The first two bands have a resolution of 250 m; bands 3 to 7 have a resolution of 500 m, while the rest have a resolution of 1000 m. The sensors have a swath width of 2330 km with an accuracy of $\pm$50 m at nadir. The Terra satellite passes over the equator in the morning from the north to the south, while Aqua passes from the south to the north in the afternoon (Fig 4.2) [79].

The generalized split-window algorithm [131] is used to retrieve the Land Surface Temperature (LST). The formulation is given by:

$$T_s = C + (A_1 + A_2\frac{1-e}{e} + A_3\frac{\Delta e}{e^2})\frac{T_i + T_j}{2} + (B_1 + B_2\frac{1-e}{e} + B_3\frac{\Delta e}{e^2})\frac{T_i - T_j}{2} \quad (4.1)$$

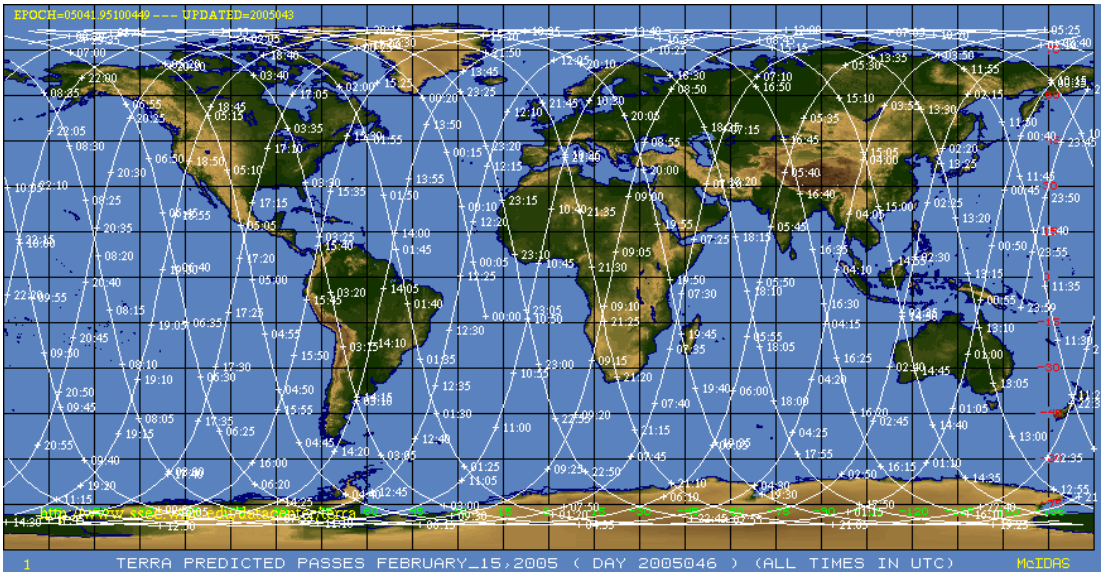

(A) Terra

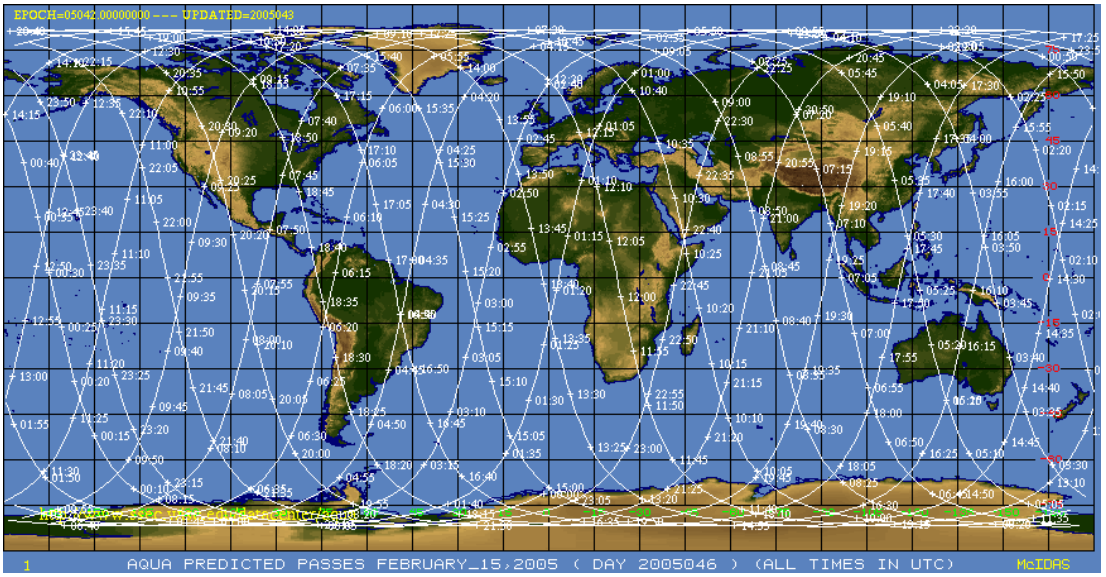

(B) Aqua

FIGURE 4.2: Orbital tracks for Terra and Aqua satellites

Here, e and Δe are land surface emissivities determined from land cover [120], given by:

$$e = 0.5(e_i + e_j) \tag{4.2}$$

and

$$\Delta e = e_i - e_j \tag{4.3}$$

The coefficients A, B and C depend on the zenith viewing angle, which can range from 0° to 60°. Additionally, they depend on air temperature range and column water vapour. These coefficients are found using regression analysis of the data simulated by the atmospheric radiative transfer model, MODTRAN4, for a multitude of surface and atmospheric conditions and integrated into the algorithm. T_i and T_j are the top of the atmosphere brightness temperature in the ith and jth channel.

In addition, an accurate split window algorithm can be developed if this regression is performed for a particular zone and if the simulated data is of good quality.

4.2.2.2 Data collection

In this study, version 5, 8-day averaged day time and night time LST from Terra and Aqua satellites are used, strictly from the same time-period as the mobile campaigns. For the pre-monsoon, data were extracted for 17th May to 24th may, 2014 and from 2nd June to 9th June, 2014. For monsoon, data were extracted for 29th August to 5th September, 2014. Finally, for winter, data were extracted for 25th of January to 1st of February, 2015.

The LST data products are archived in Hierarchical Data Format - Earth Observing System (GDF-EOS), which is a standard for such Data Information System products.

4.2.2.3 Data processing

The Land Surface Temperature (LST) is retrieved from thermal infrared (TIR) data during clear sky conditions, because during cloudy conditions, the TIR signal cannot penetrate the clouds to reach the satellites. This was the case during the monsoon campaign, and thus, only a portion of the region shows data. The cloudy section is not considered in the analysis. LST is determined from the longwave radiation emitted by the surface as observed by MODIS's instantaneous viewing angle. Since atmospheric temperature and water vapour affect the outgoing radiation, values for these can improve LST retrieval.

Before retrieval, to remove the cloudy data, the clear-sky pixels are defined using MODIS cloudmask. For version 5 data, the one used in the study, the clear-sky pixels are defined at a confidence of >= 95% over land <= 2000 m, at a confidence of >=66% over land >2000 m and at a confidence of >=66% over lakes. The effect of slope is considered and the cloud-contaminated LSTs are removed. The emissivities are estimated from bands 31 and 32 from land cover types and the version 5 data is validated up to stage 2, which means that their validity has been assessed over a large variety of locations and time periods using ground observations.

The 8 day products (MOD11A2) are composed of daily 1-kilometer LST products (MOD11A1), which are retrieved and stored on a similarly sized sinusoidal grid as averaged values, in a 1200 row by 1200 column matrix. Before conversion to 8 day products, the 1-kilometer LST products are stored in larger grids than these MODIS pixels as MOD11B1 products. The larger grid size used in this case is 5.56 km x 5.56 km.

Since MODIS provides atmospherically corrected, surface reflectance products, further corrections are not necessary.

4.3 Quantification of the factors responsible for the urban heat island effect

4.3.1 Overview of the surface energy balance

During the day, the sun heats up the Earth's surface. The solar energy reaches the Earth as both shortwave radiation, as well as longwave radiation. A part of this solar radiation is reflected back to space due to clouds, atmospheric particles as well as the surface. Another part is absorbed and re-radiated by the same atmospheric and terrestrial elements, both towards the surface and away from it. Averaged over a year, the incoming and outgoing energy for the top of the boundary layer, the atmosphere as well as the surface are balanced. A pictorial representation of the Earth's energy budget, with globally averaged values of the percentage of energy in each process, is given in Figure 4.3 [78].

The present study primarily concerns the energy balance for the surface and the canopy layer. The surface is considered to be an infinitesimal plane, with no possible storage term. A part of the shortwave radiation coming from the sun is reflected back, which is a function of the surface's albedo. The surface albedo, the ratio of outgoing shortwave radiation to incoming shortwave radiation, varies significantly for different surface types. It can have a value as high as 0.9 for white surfaces like ice to values as low as 0.05 for dark surfaces like asphalt. The longwave radiation, both from the sun, and the part reradiated by the atmosphere also accompany the shortwave radiation. Since the Earth's surface is not actually an infinitesimal plane with no storage term, the addition of heat causes it to warm up. Thus, the hot surface radiates longwave radiation. The total energy received as a result of these processes is known as the net radiation, and can vary significantly based on surface

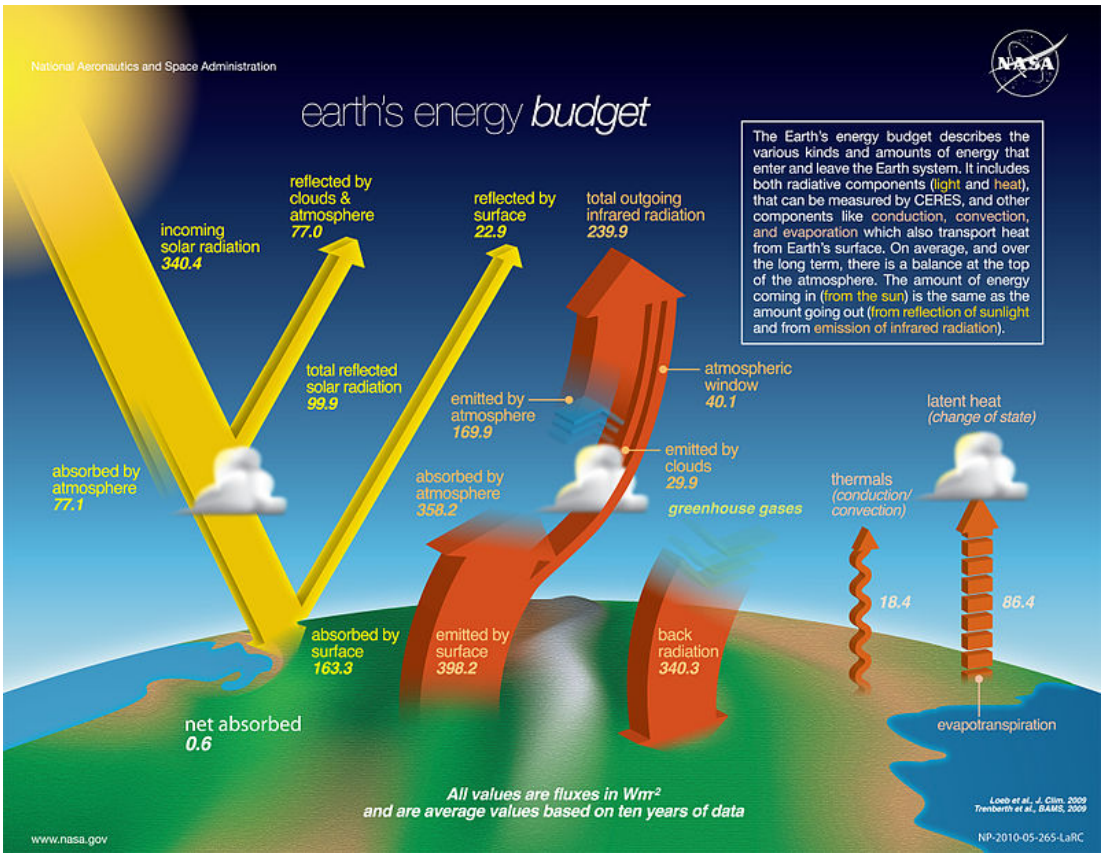

FIGURE 4.3: Earth's energy budget

albedo, thermal mass, emissivity and specific heat of the materials comprising that surface, as well as regional effects like latitude and altitude.

The net radiation received by a surface is known as the available energy and this energy is dissipated from the surface layer using three main processes. A part of the energy is conducted into the soil, due to the thermal gradient between the surface and the deeper layers. This is known as the ground flux, and in most cases, includes a storage term as well as a flux term. The ground flux is relatively small compared to the other two means of energy dissipation, the sensible heat flux and the latent heat flux. The sensible heat flux is an aggregate trem comprising of the convection and conduction from the Earth's surface to the air above it. For the air touching the ground surface, conduction can be considered. However, the conduction term

essentially disappears with height and the sensible heat flux primarily consists of the convection term, which is the vertical transfer of heat via rising air parcels. The final process of heat dissipation is through latent heat flux. The latent heat flux depicts the energy exchange through evaporation, transpiration as well as sublimation from the Earth's surface. Soil evaporation may involve the vaporisation of both the water resting on the Earth's surface as well that present within the first layer of the surface soil. In addition, the water intercepted by leaves and other vegetation above the soil surface tends to contribute to the latent heat flux through canopy evaporation. Another factor affecting the latent heat flux is transpiration, which is the release of water vapour through leaves. Plant roots absorb water from the soil. This water is released by the plant through small openings on their leaves, known as stomata. This can have a significant effect on the total latent heat flux depending on the vegetation cover of the region. The final component of the latent heat flux is direct sublimation of snow into water vapour. However, in the present study, this was not a point of concern.

These dissipation terms are more relevant for day time. During the night time, there is no shortwave radiation. Thus the atmospheric dynamics is primarily driven by the exchange of longwave radiation between the surface and the atmosphere. This, in turn, leads to a lower available energy, and, in turn, negligible dissipation terms.

The major difference between the sensible heat flux and latent heat flux is how it transfers the heat. Since the sensible heat flux implies the transfer of sensible heat, it increases the temperature of the boundary layer. On the other hand, the latent heat flux depends on the phase change of water or ice into their vapour state, while keeping their temperature constant. Thus, an increase in latent heat flux does not lead to a heating of the atmosphere, but an increase in its water content. On

the contrary, the cooling down of the surface due to removal of heat reduces the temperature of the air touching it.

The energy balance of the canopy layer is slightly more complicated because of a wide number of factors affecting it. The shortwave radiation is not easily absorbed by the atmosphere, while the longwave radiation (both incoming and outgoing) gets partly absorbed due to the presence of greenhouse gases like water vapour, carbon dioxide and methane in the atmosphere. So, one of the primary sources of energy into the canopy layer is the radiation of longwave energy. Additionally, conduction and convection also act as sources, since they increase sensible heat in that layer. However, sensible heat flux is also a sink term for a particular layer of air, since convection forces the warm air parcels upwards. Thus, the relation between air temperature at a particular height and sensible heat flux is highly non-linear. On the other hand, as mentioned earlier, latent heat flux has a slight cooling effect on the air temperature.

How the surface energy dissipation terms are partitioned can have widespread effects on both the air immediately above it as well as the regional weather. The fluxes from the surface act as the lower boundary condition in global circulation as well as regional weather models and thus, have a significant effect on the results from such model simulations. A few instances of the complex land-atmosphere feedback are given below:

As given in Figure 4.4, a decrease in surface albedo due to land use changes increases the incoming solar radiation absorption, thus increasing net radiation, which, in turn, increases the available energy for partitioning of the fluxes. This increases both latent and sensible heat flux. An increased sensible heat flux increases boundary layer heating, while an increased latent heat flux increases water vapour in the atmosphere, which, together, lead to an increase in convective clouds, which can

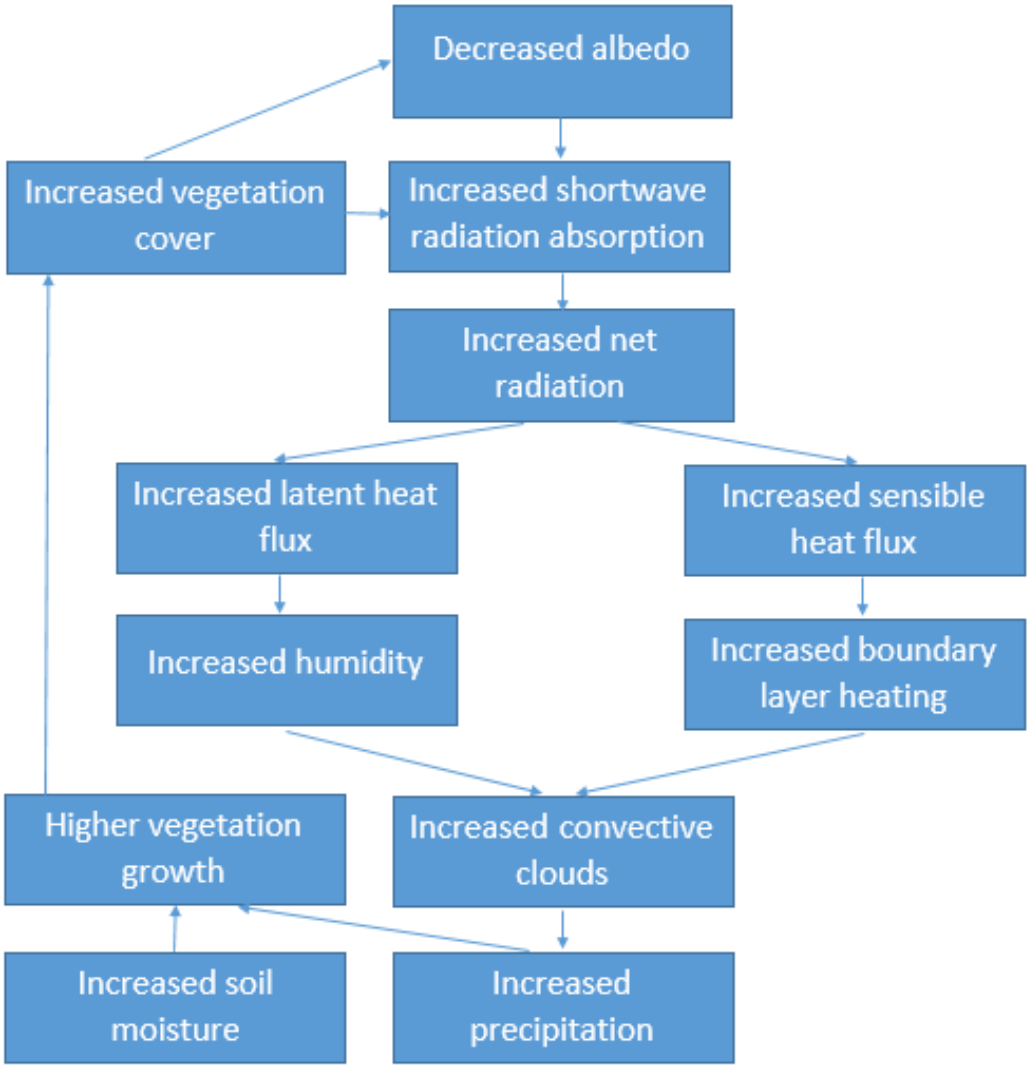

FIGURE 4.4: Land-atmophere feedback 1

block the solar radiation and reduce the net radiation in the region. On the other hand, higher convective precipitation may increase both soil moisture and vegetation, which increases vegetation cover and eventually enhances the albedo [16].

The roughness length over a surface is the height at which the wind speed theoretically becomes zero according to the log-wind profile. This theoretical construct represents how rough a surface is. A decrease in the roughness length increases the aerodynamic resistance, which limits the dissipation of both sensible and latent

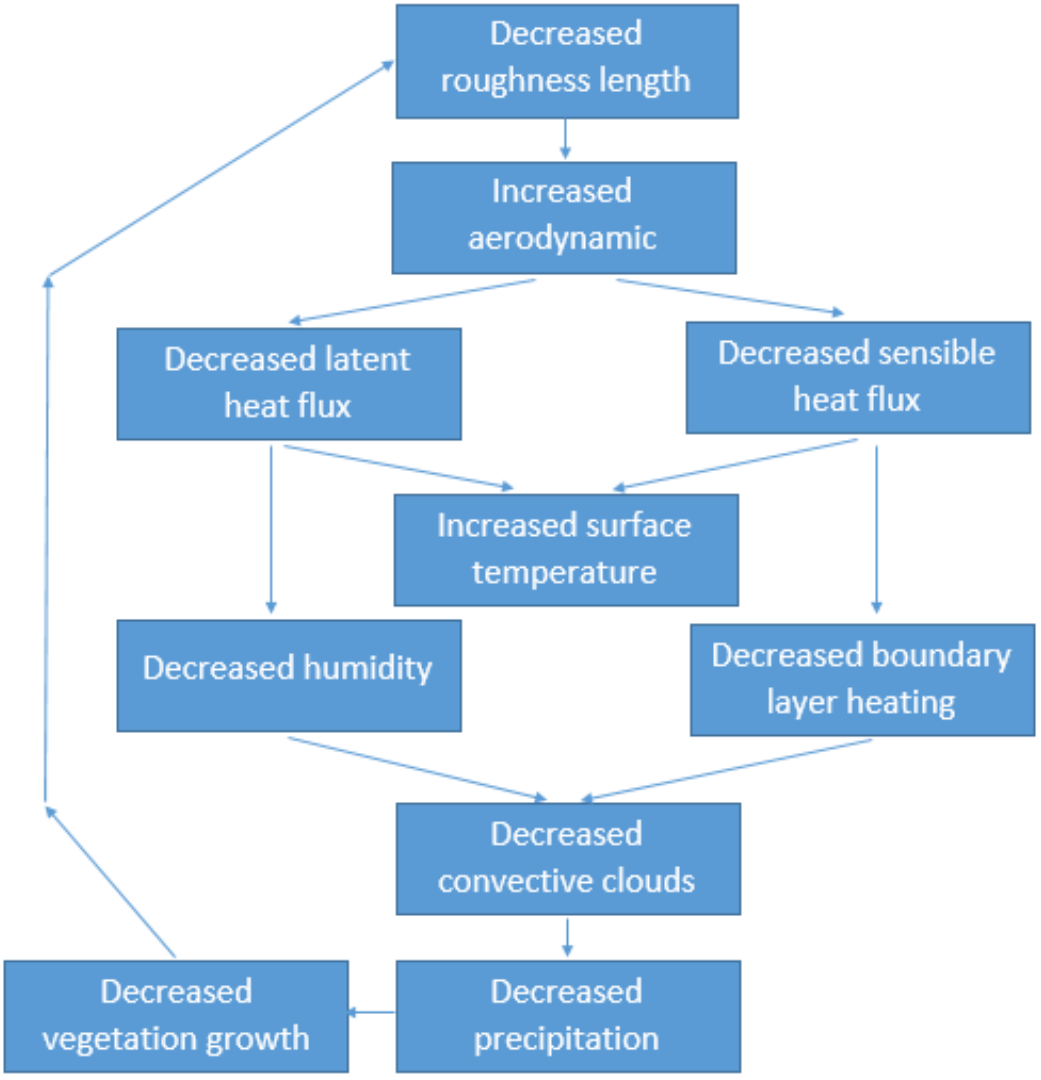

FIGURE 4.5: Land-atmophere feedback 2

heat from the surface, and thus, increases surface temperature by forcing the accumulation of the heat. A decrease in latent heat flux reduces water vapour, while a decrease in sensible heat flux reduces boundary layer heating, which, in tandem, reduce formation of convective clouds. This tends to reduce precipitation, thus limiting plant growth and reducing the canopy height and roughness length [Fig 4.5] [99].

Figure 4.6 shows that an increase in the soil moisture content of a region, for the

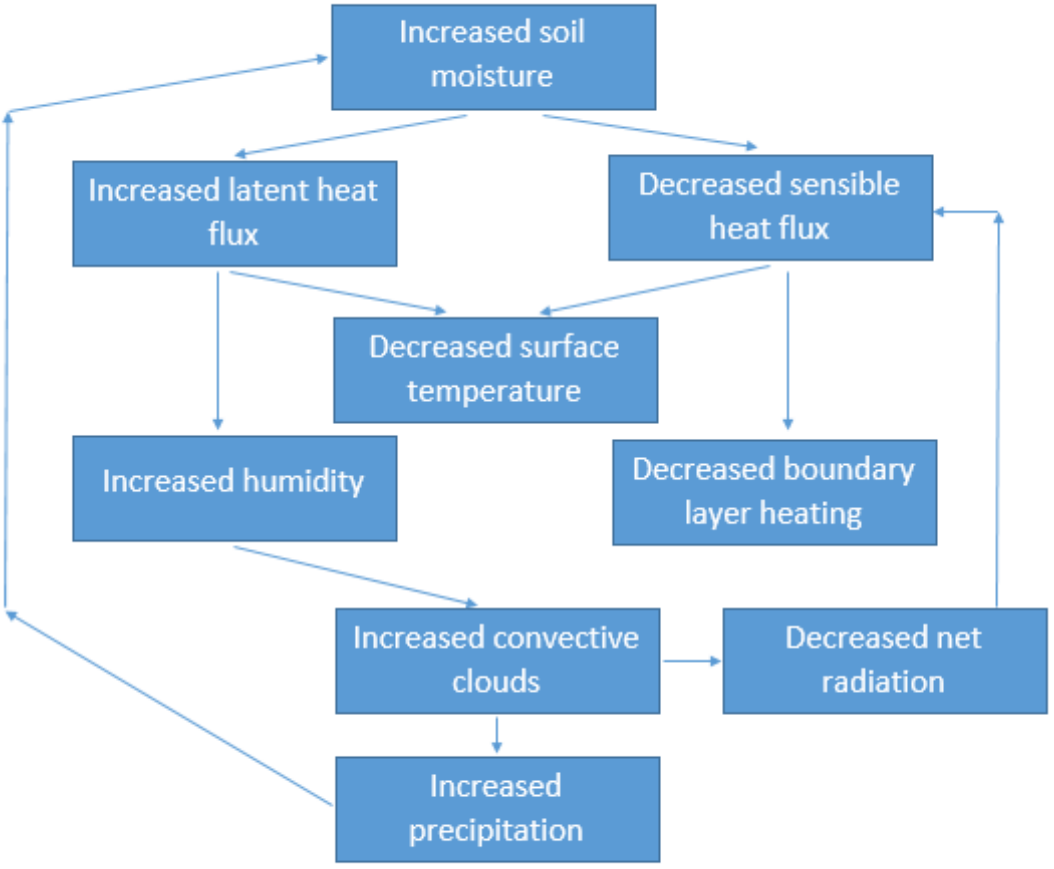

FIGURE 4.6: Land-atmophere feedback 3

same available energy, decreases sensible heat flux and increases the latent heat flux. The leads to reduction of the surface temperature, and low boundary layer heating. Higher latent heat flux leads to more water vapour, which, in turn, leads to more convective clouds, which block solar insolation and reduce net radiation, which, again, decreases the sensible heat flux. The increase in clouds also tends to cause more precipitation, which results in higher soil moisture [16].

It is evident from the above theoretical examples that land-atmosphere interactions have a significant effect on regional weather elements, including the present topic of interest, surface and air temperature, and differences between these parameters

for two distinct land use types. Surface ennergy fluxes are important components of these land-atmosphere interactions. However, though the radiative components were measured at both sites, the fluxes were not. The next subsections give overviews of two techniques used in the present study to estimate these parameters.

4.3.1.1 NOAH LSM

In 1990, the Environmental Modeling center (EMC) of the National Centers for Environmental prediction (NCEP) collaborated with the National Weather Service Hydrology Lab and the National Environmental Satellite Data and Information Service (NESDIS) Office of Research and Applications (ORA) to develop a Land Surface model for incorporation in the NCEP operational weather and climate prediction models. An inter-comparison of four models, the simple bucket model, the Oregon State University (OSU) LSM, the Simplified Simple Biosphere model (SSiB) and the Simple Water Balance model (SWB), was performed [27]. The superior performance of the OSU model led to its refinement and implementation in the NCEP regional and global coupled weather and climate model. Since then, the model, later named NOAH, has undergone a host of improvements and additions. The new name was chosen in 2000 to signify the contributions from the main agencies responsible for the model's formation and improvements. They were: National Centers for Environmental Prediction (NCEP), the department of Atmospheric Sciences of the Oregon State University, the Air Force and the Hydrologic Research Lab at NWS.

In its current iteration, the model uses one canopy layer and four soil layers, along with a diurnally dependent potential temperature approach [66], a simple canopy model [91], a multi-layered soil model [67], a bare soil evaporation scheme [82], a time integration scheme [53], a refined snowmelt algorithm [58] and thermal roughness length defined by Chen [26]. NOAH is a widely used land-surface module for the

Weather Research and Forecasting (WRF) regional weather model, which has been used for research and predictions throughout the world. Other than the simulation of snowmelts, NOAH has been shown to perform better than other land-surface models [111] and has been used as the default land-surface scheme for a host of WRF-based studies performed in India [69, 100]. However, there is a dearth of validation studies on NOAH for Indian conditions. Previous studies on validation of NOAH in the country have either concentrated on short durations (5 to 15 days) [94, 95, 130] or ignored important micrometerological parameters like skin temperature and net radiation [15]. Thus, an additional motivation of the present study is to validate the model for the two distinct land use types, which could be extended to understand the mesoscale performance of NOAH in its coupled mode, as well as the regional models which rely on its results. The model simulations will then be used to understand the UHI effect over Kanpur city.

The basic equation for the surface energy balance in the NOAH LSM is given by:

$$R_{net} = H + LE + G \tag{4.4}$$

where R_{net} is the net radiation, H is the sensible heat flux, LE is the latent heat flux and G is the soil heat flux. The bulk heat transfer equation [36] is used to estimate the sensible heat flux:

$$H = \rho C_p C_h u(T_s - \Theta_{air}) \tag{4.5}$$

where ρ is the air density, C_p is the specific heat capacity, C_h is the surface exchange coefficient for heat, which, in turn, is derived from the thermal roughness length, u is the wind speed, T_s is the surface temperature and Θ_a is the potential temperatures

for air. T_s is determined using the simple linear surface balance scheme [66]:

$$T_s = \frac{R_{net} - LE - G}{\rho C_p C_h u} + T_a \tag{4.6}$$

Similarly, the soil heat flux is estimated using Fourier's Law:

$$G = K_h \frac{T_s - T_{s1}}{dz} \tag{4.7}$$

where K_h is soil thermal conductivity, T_{s1} is the temperature at the first soil layer and dz is the depth of said layer. The thermal conductivity is calculated from an aggregate calculation of the conductivity of the soil components depending on the degree of saturation [97]. The equation is:

$$K_h = K_e(K_{sat} - K_{dry}) + K_{dry} \tag{4.8}$$

where K_{dry} is the dry thermal conductivity, given by:

$$K_{dry} = \frac{.135\gamma_d + 64.7}{2700 - .947\gamma_d} \tag{4.9}$$

and K_e is the Kersten number, representing degree of saturation, which is given by:

$$K_e = log\frac{sm}{sm_{sat}} + 1 \tag{4.10}$$

Here, γ_d is formulated as:

$$\gamma_d = (1 - sm_{sat})2700 \tag{4.11}$$

K_{sat} is calculated as a function of the soil's liquid, ice and soil content.

$$K_{sat} = K_{soil}^{1-sm_{sat}} K_{liq}^{sm_{liq}} K_{ice}^{1-sm_{ice}} \tag{4.12}$$

where K_{soi} is the thermal conductivity of the dry soil, given as:

$$K_{soil} = K_{qtz}^{qtz} K_o^{1-qtz} \tag{4.13}$$

K_{liq}, K_{ice}, K_{qtz} and K_o are the thermal conductivities of water, ice, quartz and other soil content respectively, sm_{liq} and sm_{ice} are the liquid and frozen water contents respectively, qtz is the fractional qtz content (a function of soil type).

The latent heat flux is taken as the summation of direct soil evaporation (E_{dir}), canopy evaporation (E_c), transpiration (E_t) and sublimation from snowpack (E_{snow}), all dependent on the Penman-derived potential evaporation formulation (E_p) [66], given by:

$$E_p = \frac{\Delta(R_{net} - G) + \rho\lambda C_q u(q_{sat} - q)}{1 + \Delta} \tag{4.14}$$

$$Edir = (1 - f_c)(\frac{sm_1 - sm_{dry}}{sm_{sat} - sm_{dry}})^{f_x} E_p \tag{4.15}$$

$$Ec = f_c E_p (\frac{cmc}{cmc_{max}})^{0.5} \tag{4.16}$$

$$Et = f_c E_p P_c (1 - (\frac{cmc}{cmc_{max}})^{0.5}) \tag{4.17}$$

$$E_{snow} = E_p f_{sn} \tag{4.18}$$

where Δ is the slope of the saturated vapour pressure curve, λ is the latent heat of evaporation, C_q is the surface exchange coefficient for moisture, q_{sat} is saturated specific humidity, q is the specific humidity, f_c is the vegetation fraction, sm_1 is the soil moisture at the first soil layer, sm_{dry} is the wilting point, sm_{sat} is the saturated soil moisture, f_x is an empirical factor, cmc is the actual canopy moisture content, cmc_{max} is the maximum canopy moisture content, P_c is the plant coefficient and f_{sn} is the fractional snow coverage.

The plant coefficient is calculated following the equation given by Jacquemin and Noilhan [82]:

$$P_c = \frac{1 + \frac{\Delta}{R_r}}{1 + R_c C_h + \frac{\Delta}{R_r}} \tag{4.19}$$

where R_r is a function of air temperature, pressure and C_h and R_c is the stomatal resistance defined as:

$$R_c = \frac{R_{c,min}}{LAI RC_{rad} RC_{temp} RC_{hum} RC_{soil}} \tag{4.20}$$

$$RC_{rad} = \frac{ff + \frac{R_{c,min}}{R_{c,max}}}{ff + 1} \tag{4.21}$$

$$where ff = 1.10 \frac{S_i}{LAI R_{gl}} \tag{4.22}$$

$$RC_{temp} = 1 - .0016(T_{opt} - T_a)^2 \tag{4.23}$$

$$RC_{hum} = \frac{1}{1 + h_s(q_{sat} - q)} \tag{4.24}$$

$$RC_{soil} = \sum_{i=1}^{n_{root}} \frac{sm_i - sm_{i,wlt}}{sm_{ref} - sm_{i,wlt}} f_{root}^i \tag{4.25}$$

where LAI is the Leaf Area Index, $R_{c,min}$ is the minimum stomatal resistance and $R_{c,max}$ is the maximum stomatal resistance, all of which depend on the vegetation type, RC_{rad}, RC_{temp}, RC_{hum} and RC_{soil} are the RC factors in terms of incoming solar radiation S_i, temperature, humidity and soil moisture respectively, R_{gl}, T_{opt} and h_s are semi-empirical parameters for optimum transpiration with respect to incoming solar radiation, air temperature and humidity respectively, sm_{ref} is the threshold moisture content at which transpiration becomes stressed, f_i is the fraction of root zone represented by the i_{th} layer, n_{root} depicts the number of root layers, sm_i is the soil moisture content of the i_{th} layer and $sm_{i,wlt}$ is the wilting point of the i_{th} layer.

The soil moisture, which is required for estimation of the direct soil evaporation, is found by solving the diffusion form of Richard's equation:

$$\frac{\delta sm}{\delta t} = \frac{\delta}{\delta z}(D\frac{\delta sm}{\delta z}) + \frac{\delta K}{\delta z} \pm S \tag{4.26}$$

where D is the soil water diffusivity, K is the hydraulic conductivity and S is the source/sink term, in the form of precipitation, transpiration, etc. Similarly, the soil temperature, which is necessary for estimation of the ground flux, is determined by solving the thermal diffusion equationl:

$$\frac{\delta T}{\delta t} = \frac{1}{C}\frac{\delta}{\delta z}K_h\frac{\delta T}{\delta z} \tag{4.27}$$

where C is the specific heat capacity of the soil and K_h is the thermal conductivity of the soil, both of which are functions of the soil type chosen in the lookup table.

The specific heat capacity of the soil is found using:

$$C = f_{soil}C_{soil}f_{liq}C_{liq}f_aC_a \tag{4.28}$$

where f_{soil}, f_{liq} and f_a are the volume fractions and C_{soil}, C_{liq} and C_a are the specific heat capacities for solid soil, water and air respectively.

Further detailed information on the lineage and formulations of the model can be found at Ek, et al [33]. Additionally, a list of the parameterization schemes used in NOAH, the parameterizations used in the present study, as well as the list of vegetation and soil type in the model are attached in Appendix D.

The version of NOAH used in the study was the uncoupled 1D NOAH LSM version 3.4.1. The model takes air temperature, humidity, wind speed, wind direction, surface pressure, precipitation, incoming shortwave radiation and incoming longwave

radiation as forcing variables. All the data were available at 15 minute intervals and the model output was also taken at the same interval. The model was initialized using soil moisture and soil temperature at 4 depths and the skin temperature value from CNR4.

Both sites have silty clay soil. 'Urban and built-up land' vegetation type was taken for the urban site, while 'dryland, cropland and pasture' vegetation type was used for the rural site. The evaluation was performed for three seasons, pre-monsoon, monsoon and post-monsoon, at daily frequency. The parameters were not evaluated for winter since a lot of night time data were missing at both sites due to the insufficient charging via solar panels due to heavy fog.

4.3.1.2 Bowen ratio method

The Bowen Ratio Energy Balance method (BREB) is a robust and cheap micrometeorological technique that can be used to estimate sensible and latent heat fluxes over different surfaces. Though the method is simple and an indirect estimation of the fluxes, many studies have shown that the method has a good amount of agreement with the more advanced techniques used for measurement of the turbulent fluxes (like eddy covariance technique [114]).

The BREB method determines the latent and sensible heat fluxes by using net radiation, soil flux, temperature gradient and humidity gradient measurements. It is simple since the calculations are relatively straight-forward, with no information required about the aerodynamic properties of the surfaces being studied, and no problem of scale. The method can be used to quantify fluxes for different temporal and spatial scales with almost equal efficiency. However, the technique is sensitive to sensor accuracy, since it relies on two sensor measurements, thus doubling the

errors associated with it and cannot give proper results during turbulent advection. The method depends on several assumptions [34]. The transport of both vapour and sensible heat is assumed to be one-dimensional and no horizontal gradients are taken into account. The surface below the instruments is assumed to be homogeneous as far as source/sinks are concerned and the exchange coefficients for heat and water vapour are taken as equal. A detailed overview of the formulations used in this method are given below.

The sensible and latent heat fluxes are considered analogous to molecular diffusion. From there, we get:

$$H = \rho C_p k_h \frac{\delta T}{\delta z} \tag{4.29}$$

and

$$E = k_v \frac{\delta \rho_v}{\delta z} \tag{4.30}$$

where H is the sensible heat flux, ρ is the air density, C_p is the specific heat capacity of air, k_h is the eddy diffusivity for heat, $\frac{\delta T}{\delta z}$ is the gradient of air temperature with height, E is the water vapour flux, k_v is the eddy diffusivity for water vapour and $\frac{\delta \rho_v}{\delta z}$ is the vapour density gradient.

The universal gas law can be applied to convert the equation to the form:

$$LE = \frac{\rho \lambda \varepsilon}{P} \frac{\delta P_v}{z} \tag{4.31}$$

where λ is the latent heat of vaporization, ε is the ratio of molecular weight of water vapour to that of air=.622, P is the atmospheric pressure and $\frac{\delta P_v}{\delta z}$ is the water vapour pressure gradient.

In discretized form, the equations become:

$$H = \rho C_p k_h \frac{T_1 - T_2}{z_1 - z_2} \tag{4.32}$$

and

$$LE = \frac{\rho \lambda \varepsilon}{P} \frac{P_{v1} - P_{v2}}{z_1 - z_2} \tag{4.33}$$

where subscripts (1) and (2) refer to the parameters are two separate heights from the ground surface.

The Bowen ratio (β) is defined as:

$$\beta = \frac{\rho C_p k_h \frac{T_1 - T_2}{z_1 - z_2}}{\frac{\rho \lambda \varepsilon}{P} \frac{P_{v1} - P_{v2}}{z_1 - z_2}} \tag{4.34}$$

Since the eddy diffusivities for both heat and vapour are considered equal, the equation reduces to:

$$\beta = \gamma \frac{T_1 - T_2}{P_{v1} - P_{v2}} \tag{4.35}$$

where γ is the Psychrometric constant, and given by:

$$\gamma = \frac{C_p P}{\lambda \epsilon} \tag{4.36}$$

The specific heat at constant pressure is given by:

$$C_p = C_{pd}(1 + .849\varepsilon \frac{P_v}{P}) \tag{4.37}$$

where C_{pd} is the specific heat capacity of dry air (constant) and P_v is the vapour pressure in the atmosphere, which is given by: and

$$P_v = \frac{RHP_{vs}}{100} \tag{4.38}$$

where RH is the Relative Humidity. The saturated vapour pressure (P_{vs}) is defined as:

$$P_{vs} = 6.112e^{6816\frac{1}{273.15}-\frac{1}{T_a+273.15}+5.131log\frac{273.15}{T_a+273.15}} \tag{4.39}$$

The sensible and latent fluxes are written as functions of the Bowen ratio, given by:

$$H = \beta\frac{R_{net}-G}{1+\beta} \tag{4.40}$$

and

$$LE = \frac{R_{net}-G}{1+\beta} \tag{4.41}$$

where G is the ground flux.

BREB method, though a flexible technique, was not used for the entire study period. This was for three reasons. Firstly, the second sensors required for the BREB method were set-up in August, 2014. Thus, our attempt to understand the inter-seasonality between the two seasons of pre-monsoon and monsoon could not be accomplished using this technique. Secondly, we did not have heat flux plates at the site. Lastly, for the lower sensor, only one calibration was performed, at the end of August. Thus, we could not be confident about the performance of the lower sensors throughout the study period. Hence, the fluxes measured by this method could not be used for correlation studies.

Instead, the BREB method was used for additional experiments to understand how the surface type influences the energy partitioning, especially the effect of the intra-urban variations on energy dissipation. An experiment was set-up using CNR4 and two Vaisala HMT330s at two heights over asphalt for two days. The results from this temporary Bowen ratio station was compared with the values obtained from the urban park and the rural field. The ground flux was parameterized as 10% of the net radiation, which is a reasonable estimation [117].

4.3.2 Radiation components

Since radiation is an important factor for both the canopy as well as the surface temperature, it was used to understand the diurnality and inter-seasonality of the UHI_{canopy} and $UHI_{surface}$. However, because of the lack of proper calibration and correction of the sensors after September and the lack of night time radiation data for the second half of post-monsoon and the entirety of winter season, only the inter-seasonality between the pre-monsoon and monsoon season was studied using the radiation and modelled data.

4.3.3 Urban wind speed

The influence of wind on air temperature at a location is well-established, with advection being a principle sink for temperature. In this study, the effect of urban advection on the UHI_{canopy} was investigated using box plot analysis for a time period of one and a half years (October, 2013 to February, 2015).

4.3.4 Data processing

The effect of the land use pattern (urban vs rural) on the radiation components was determined for each season by analyzing the relative magnitude of the components at each site during the study period. As mentioned earlier, the day time and night time atmospheric dynamics are disparate. To determine the factor behind the night time canopy heat island, only the longwave radiation data were considered. The difference in outgoing and incoming longwave radiation between the urban and rural station was correlated with the heat island intensity for each season. For day time, both the sensible heat flux and the radiation differences were used for the analysis.

For June, July and part of August, radiation data were not available at the rural site due to an incidence of vandalism. For this period, as well as for another 20 days at the end of March when rural radiation data was missing, the NOAH model was forced using measurements from a nearby sub-urban site (IITK) after proper calibration and correction using data from the rest of the year (Appendix E). However, this data was not used for the regression analysis between the radiation difference and the UHI_{canopy}.

4.4 Summary

A wide variety of instruments have been used to quantify the UHI effect and tease out the main reasons behind the phenomenon. The specifications of all the instruments used in the study are attached in Appendix F. Furthermore, experimental campaigns and satellite data have been used to quantify the spatial aspect of the UHI_{canopy} and $UHI_{surface}$ respectively. Two main techniques have been used to understand the surface energy partitioning at the two sites, the Bowen ratio method and the NOAH Land Surface model. The use of these instruments, techniques and models have given great insights into the complex land-atmosphere interactions and the different factors driving the near-surface atmospheric dynamics.

Chapter 5

Results and discussion

5.1 UHI quantification

5.1.1 Temporal study

Kanpur city shows a diurnality in mean UHI_{canopy} and $UHI_{surface}$, with higher night time UHI_{canopy} for all seasons (Fig. 5.1). The UHI_{canopy} reaches a maximum value at around midnight (local time), with an average value of 3.6±1.08 °C for pre-monsoon, 2±0.96 °C for monsoon, 2.78±.85 °C for post-monsoon and 2.6±1.2°C for winter. A minimum UHI_{canopy} value of 1.44±1.18 °C is seen for pre-monsoon, while monsoon shows a least mean UHI_{canopy} of .5±1.33 °C. For post-monsoon, the minimum value is .8±.67°C. Winter also shows a low minimum UHI_{canopy} of .65±.82°C. The standard deviation of the UHI_{canopy} is higher during monsoon and winter, suggesting the intereference of cloudy days and foggy periods respectively on the UHI_{canopy} magnitude. The seasonal, diurnal trend of $UHI_{surface}$ varies, with day time $UHI_{surface}$ higher than night time $UHI_{surface}$ for pre-monsoon, but showing the opposite effect during the other seasons (Fig. 5.2). The first part of the day has an almost

non-existence $UHI_{surface}$ in all seasons, except for monsoon, which shows consistently high $UHI_{surface}$ values throughout the day. Additionally, though the UHI_{canopy} magnitude is higher during pre-monsoon and lowest during monsoon, $UHI_{surface}$ magnitude shows the least values during pre-monsoon, which may have something to do with the dryness of the season. $UHI_{surface}$ shows lower day time variation for monsoon, post-monsoon and winter and maximum mean $UHI_{surface}$ magnitude is 3.4±3.24 °C during pre-monsoon, 5±0.68 °C during monsoon, 5.36±2.55°C during post-monsoon and 5.6±2.76°C during winter. However, for post-monsoon and winter, the night time data for surface temperature was missing. The lower UHI_{canopy} during the wet period has also been seen in previous studies [50]. UHI values for different cities in India, including this study, are given in Table 2.2. Kanpur and Delhi, both incidentally situated in the Indo-Gangetic basin, show comparable UHI intensities. Cities outside this zone generally show a lower UHI.

The UHI_{canopy} is highest during pre-monsoon for both day time and night time (Fig. 5.1). On the contrary, the $UHI_{surface}$ shows the least values during this season (Fig. 5.2).

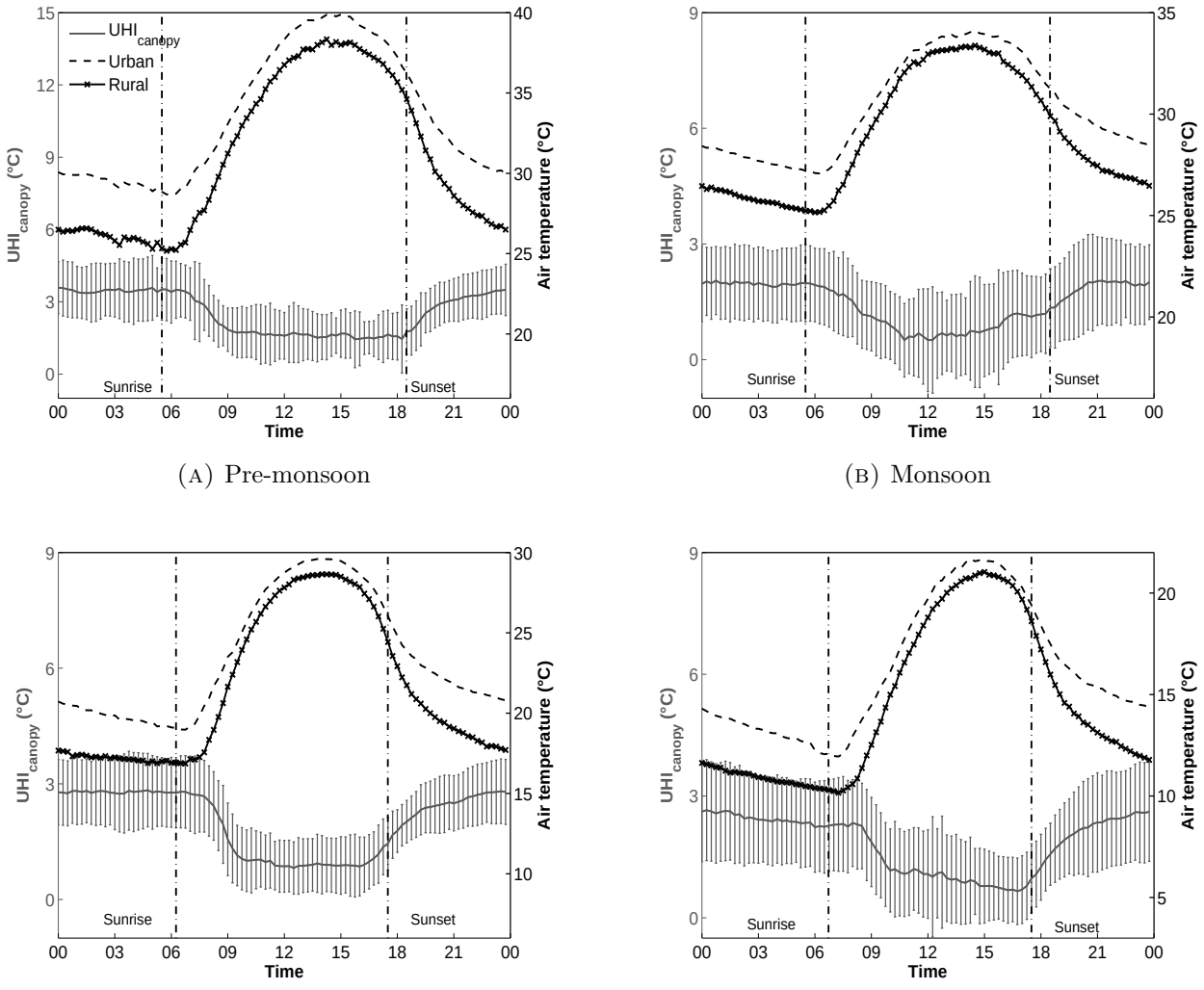

(A) Pre-monsoon

(B) Monsoon

(C) Post-monsoon

(D) Winter

FIGURE 5.1: Diurnal variation in UHI_{canopy}

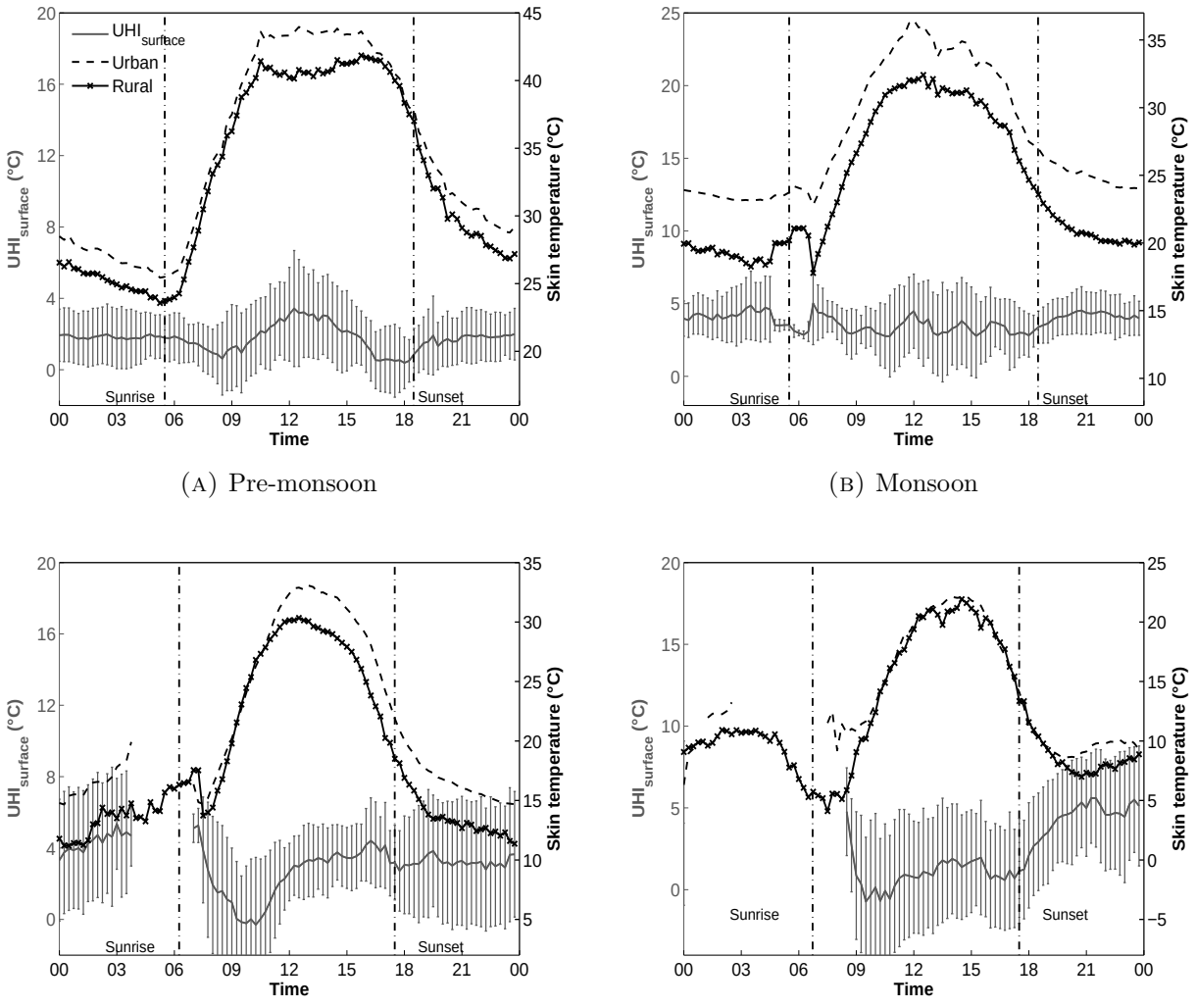

(A) Pre-monsoon

(B) Monsoon

(C) Post-monsoon

(D) Winter

FIGURE 5.2: Diurnal variation in $UHI_{surface}$

5.1.2 Spatial study

The results of the mobile measurement campaigns over Greater Kanpur are computed by averaging over 4 km x 4 km grids and show a significant UHI_{canopy} around the city core, where the city core is indicated by the region within the two vertical lines (Fig. 5.3). The satellite derived surface temperature shows a pattern similar to that of the air temperature. Higher values are observed in the spatial studies compared to the values derived from the fixed stations for the same season (Fig. 5.3, 5.4). The urban fabric is highly heterogeneous, with different kinds of surface materials; from grassy urban parks, to concrete sidewalks and buildings, to asphalt pavements. Since asphalt and concrete have a higher heat capacity than soil, and the MODIS plots used have a resolution of 1 km x 1 km, the night time $UHI_{surface}$ averaged over the heterogeneous urban surface will evidently be higher than the $UHI_{surface}$ between two grassy surfaces. The result from the second measurement campaign during pre-monsoon shows similar gradient and magnitude of the UHI_{canopy} (Fig. 5.4). A third measurement campaign was performed during a cloudy monsoon night (Fig. 5.5). The monsoon measurement campaign shows lower UHI_{canopy} (around 2 °C) when compared to the values obtained for pre-monsoon, which could be due to the presence of clouds [75]. This also corroborates the inter-seasonality observed in the temporal variation of the UHI_{canopy}. Moreover, since the monsoons in the region tend to be more cloudy compared to the pre-monsoons, cloudiness could be one of the factors responsible for the lower UHI_{canopy} during monsoon. Complete satellite-derived surface temperature estimates were unavailable during the cloudy period. The partial results are shown in Figure 5.5. The final campaign was conducted during the winter season (Fig. 5.6) and both the UHI_{canopy} and $UHI_{surface}$ values during this period were found to be low.

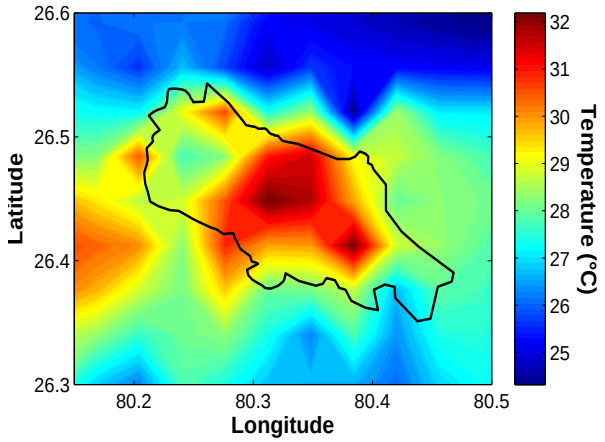

(A) UHI_{canopy} on 23rd May, 2014

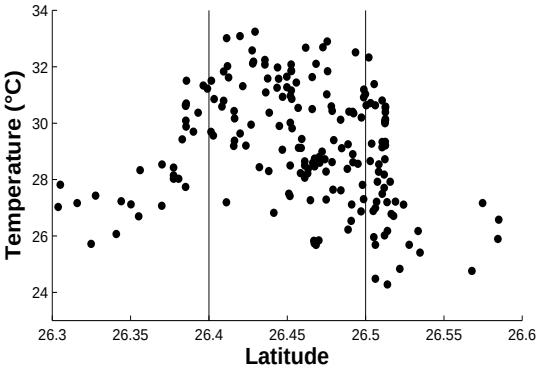

(B) Canopy temperature vs latitude

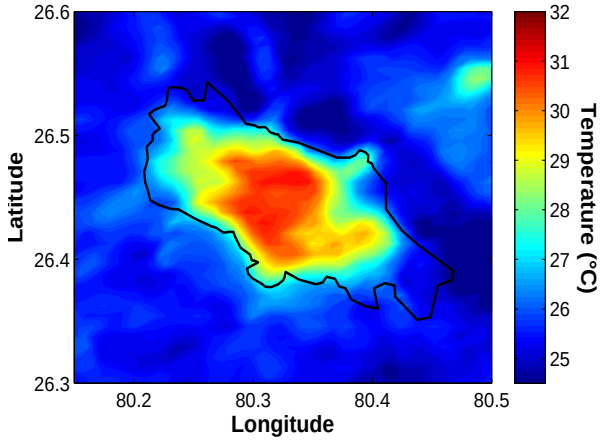

(C) $UHI_{surface}$ during 17th May to 24th May, 2014

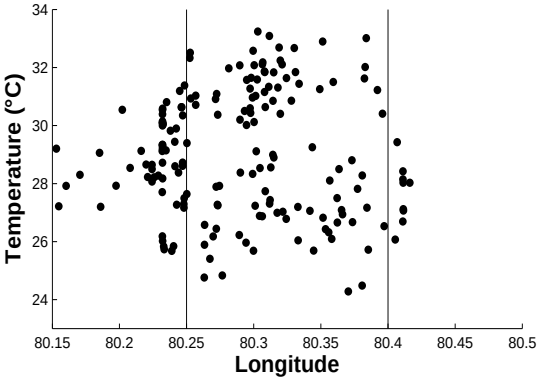

(D) Canopy temperature vs longitude

FIGURE 5.3: Spatial variation in night time UHI for pre-monsoon [1]

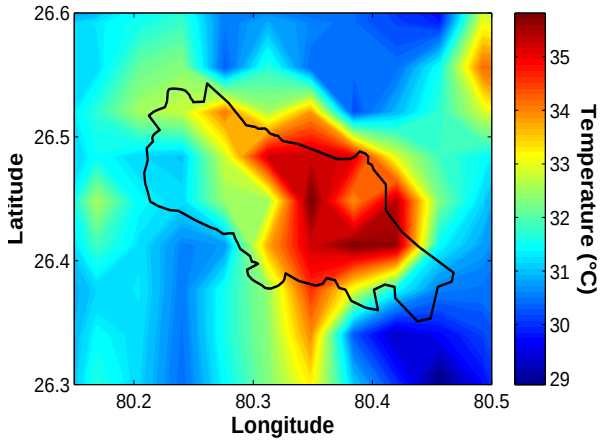

(A) UHI_{canopy} on 6th June, 2014

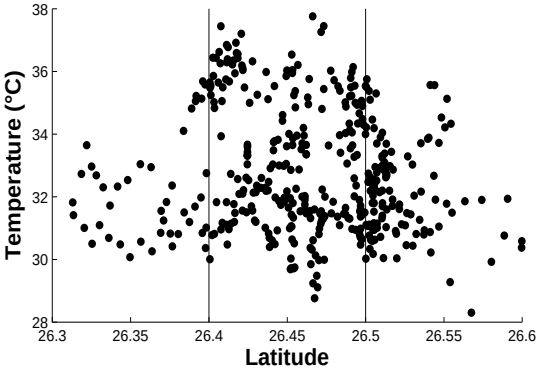

(B) Canopy temperature vs latitude

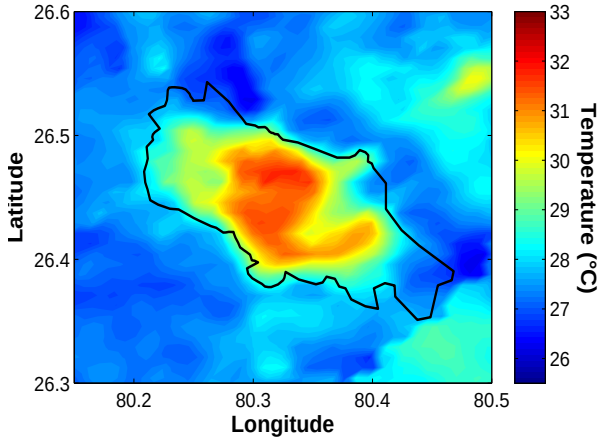

(C) $UHI_{surface}$ during 2nd June to 9th June, 2014

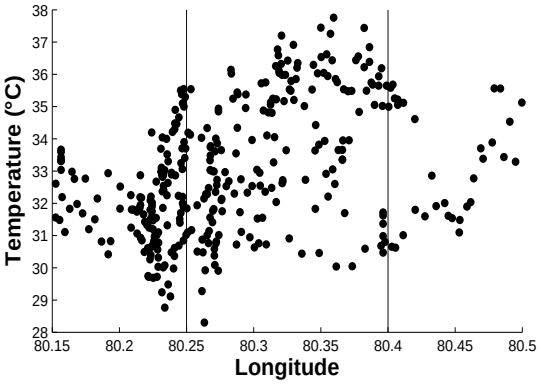

(D) Canopy temperature vs longitude

FIGURE 5.4: Spatial variation in night time UHI for pre-monsoon [2]

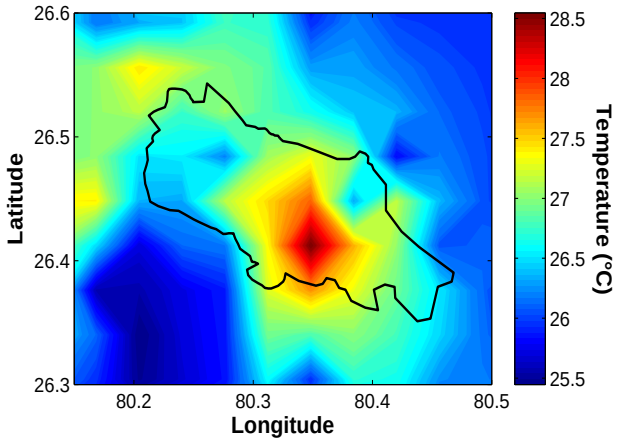

(A) UHI_{canopy} on 5th September, 2014

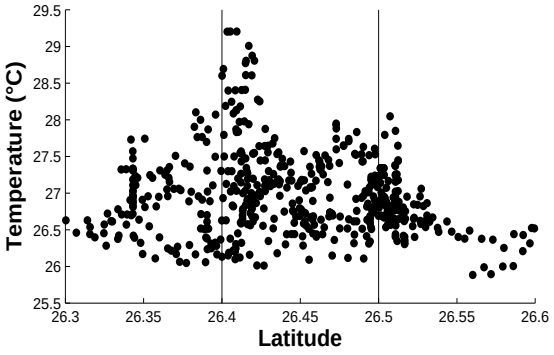

(B) Canopy temperature vs latitude

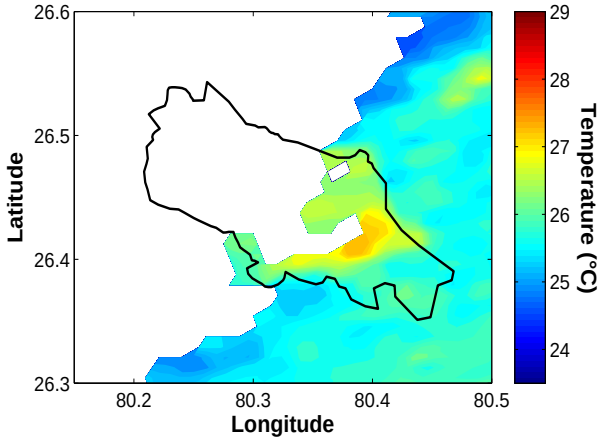

(C) $UHI_{surface}$ during 29th August to 5th September, 2014

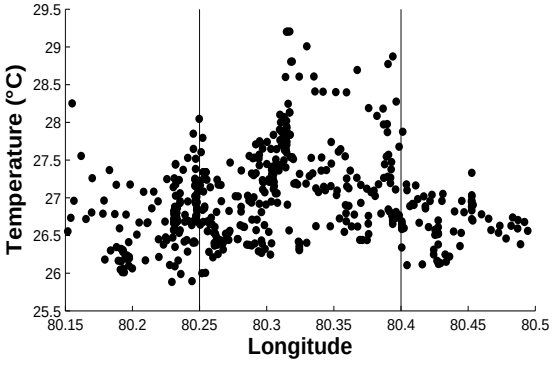

(D) Canopy temperature vs longitude

FIGURE 5.5: Spatial variation in night time UHI for monsoon

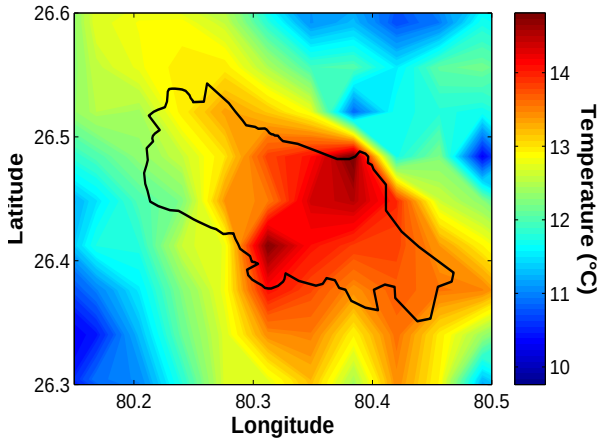

(A) UHI_{canopy} on 28th January, 2015

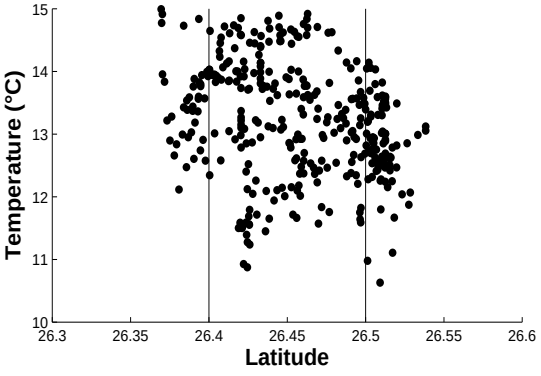

(B) Canopy temperature vs latitude

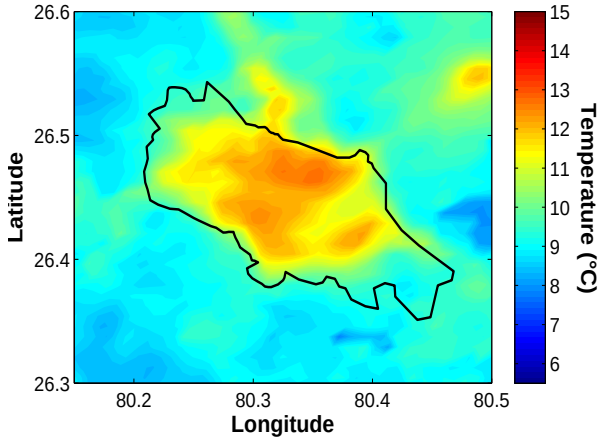

(C) $UHI_{surface}$ during 25th January to 1st February, 2015

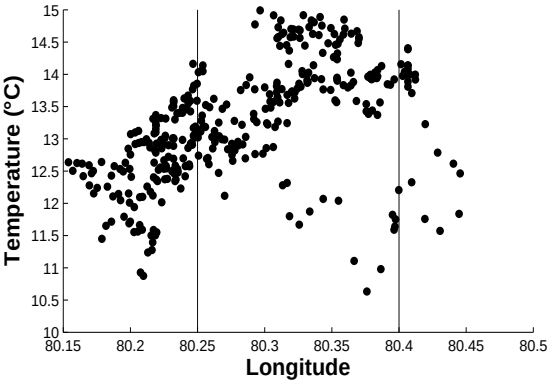

(D) Canopy temperature vs longitude

FIGURE 5.6: Spatial variation in night time UHI for winter

The day time $UHI_{surface}$ patterns differ from the night time patterns (Fig. 5.7). During pre-monsoon, the city consists of cool pockets, and overall, the city surface is cooler than the countryside. This trend has also been found for Delhi in previous studies [92, 93]. Winter season shows an opposite trend, with lower day time $UHI_{surface}$. The results from the day time spatial analysis of $UHI_{surface}$ is close to the results of the temporal study. The Terra satellite passes over the region at around 10:15 in the morning, which is the part of the day when the $UHI_{surface}$ is close to zero (Fig. 5.2). Though earlier studies have concluded that MODIS underestimates the surface temperature of non-forested areas [63, 135], though mainly in case of C5 products, the parity between the ground based observations and MODIS results suggests that this could also be due to the faster heating rate in rural areas, which negates any $UHI_{surface}$ during the first half of the day. As the day advances, and the solar energy starts declining, the rural area also starts cooling down faster due to its lower thermal mass, and the $UHI_{surface}$ emerges again.

To test this, the day time LST was also plotted from the MODIS Aqua satellite-derived datasets, as the Aqua satellite passes over the region at a later time (after 1330 hrs). If this hypothesis is correct, the urban cool islands should disappear, or at least get reduced, in this dataset. This is clearly seen from comparing Figure 5.7 and Figure 5.8. For pre-monsoon, in the Terra data, the urban cool island of 2°C is seen during May and a 4°C urban cool island is seen in June. In the Aqua data, these two cool islands virtually disappear. The only exception is the part to the north of the city boundary, which is probably colder due to the presence of the river Ganga. For winter, the $UHI_{surface}$ increases from the time of the Terra pass to the Aqua pass. This is also seen in the temporal analysis (Fig. 5.2). However, there is still a difference in magnitude between the satellite-derived data and the ground observations for pre-monsoon. This could be either a consequence of the

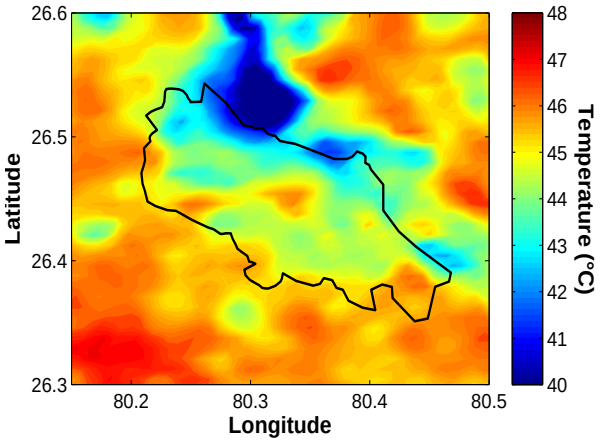

(A) 17th May to 24th May, 2014

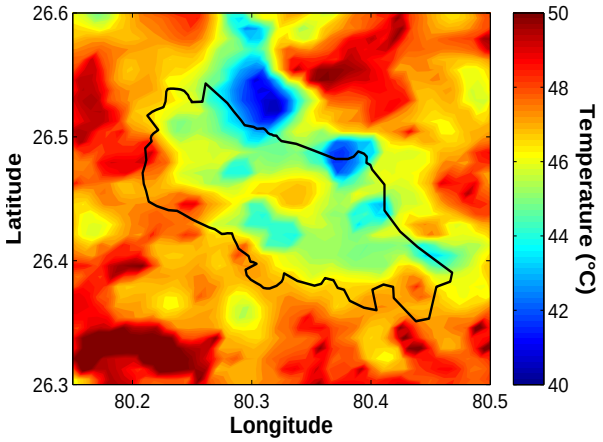

(B) 2nd June to 9th June, 2014

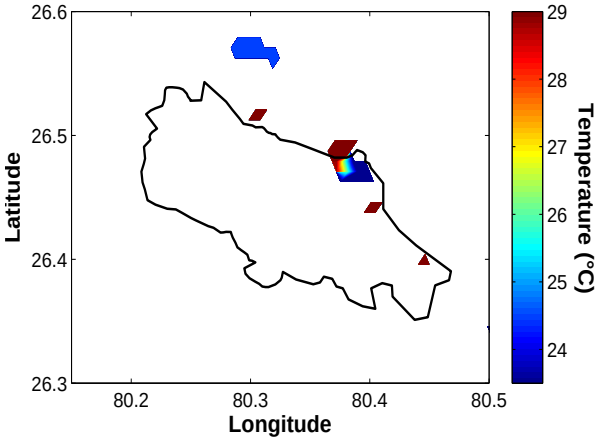

(C) 29th August to 5th September, 2014

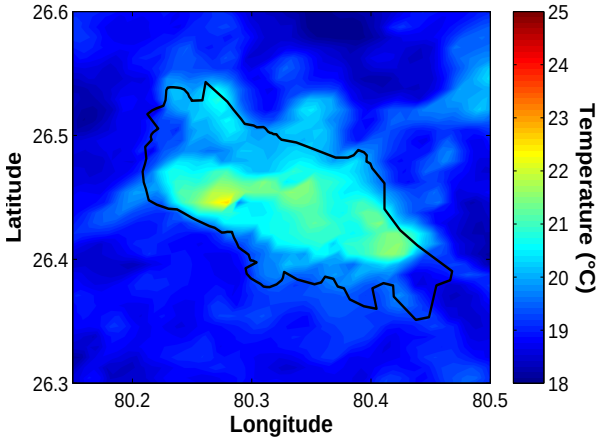

(D) 25th January to 1st February, 2015

FIGURE 5.7: Spatial pattern of land surface temperature from MODIS Terra 8-day dataset

averaging inherent in the MODIS datasets or a systematic underestimation of the surface temperature in this season.

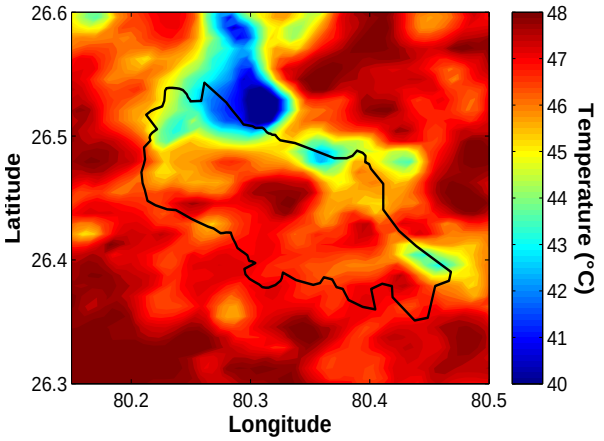

(A) 17th May to 24th May, 2014

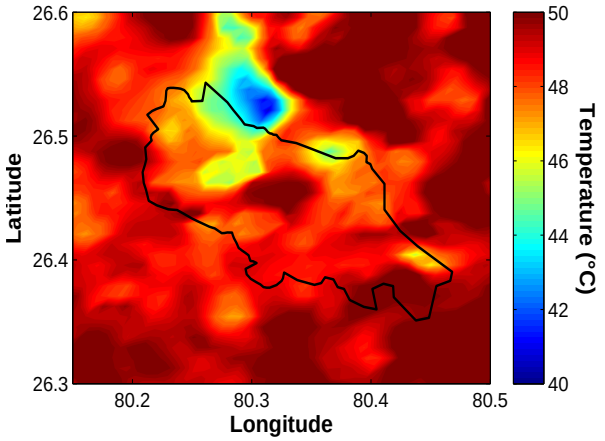

(B) 2nd June to 9th June, 2014

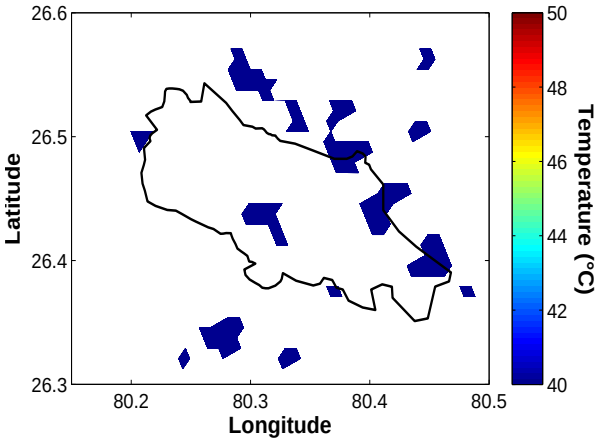

(C) 29th August to 5th September, 2014

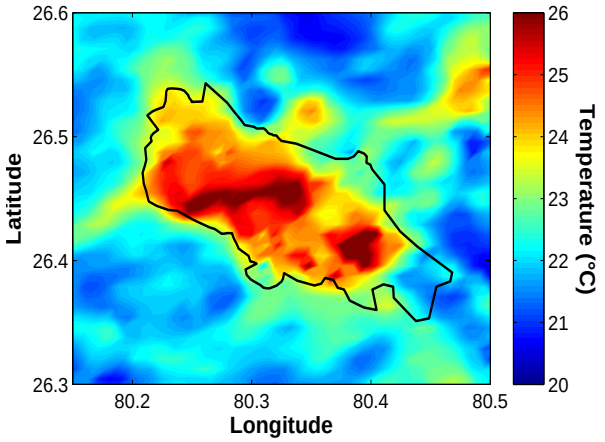

(D) 25th January to 1st February, 2015

FIGURE 5.8: Spatial pattern of land surface temperature from MODIS Aqua 8-day dataset

5.2 Contribution of factors to heat island formation and its inter-seasonality

5.2.1 Radiation components and the $UHI_{surface}$

Figure 5.9 shows the diurnal variation of the four components of the radiative balance for the rural area for three seasons as well as the urban-rural differences in each of those terms. Here, the downward R_{net}, incoming shortwave radiation and incoming longwave radiation and the upward outgoing shortwave radiation and outgoing longwave radiation are taken as positive. In pre-monsoon, the incoming shortwave radiation reaches a maximum mean value of 750±27.5W/m^2 at around 1130 hrs, while the outgoing shortwave radiation is 169±50W/m^2 at the same time. The incoming longwave radiation varies from a minimum of 411±24W/m^2 at 0600 hrs to a maximum value of 484±29W/m^2 at 1345 hrs. The outgoing longwave radiation is higher than the incoming longwave radiation, and varies from a minimum of 442±22W/m^2 at around 0600 hrs to 558±25W/m^2 at around 1545 hrs. All components of the radiative balance show relatively smooth trends during pre-monsoon, which reflects the clear sky conditions that prevail during this season.

During monsoon, the diurnal trend of incoming shortwave radiation is broken near midday, possibly due to interference by clouds (Fig. 5.9). Maximum incoming and outgoing shortwave radiation of 724±247W/m^2 and 150±58.6W/m^2 respectively are seen at around 1145 hrs. The high standard deviation in incoming shortwave radiation is indicative of the influence of the large number of cloudy days during this season. The longwave components show a trend similar to that of pre-monsoon. The incoming longwave radiation varies from a mean minimum of 384±27W/m^2 at 0530

hrs to a maximum value of 438±13W/m^2 at 1230 hrs, while the outgoing longwave radiation ranges from 405±18W/m^2 at 0530 hrs to 497±27W/m^2 at 1230 hrs.

During post-monsoon, the highest mean value of incoming shortwave radiation is 600±108W/m^2 at 1145 hrs; the low value indicating the large distance of the Earth from the Sun during this season. The highest mean outgoing shortwave is The incoming 81±28W/m^2 at 1200 hrs. The incoming longwave radiation varies from 346±27W/m^2 at 2345 hrs to 391±22W/m^2 at 1315 hrs, while the outgoing longwave radiation varies from 368±32W/m^2 at 1450 hrs to 481±18W/m^2 at 1230 hrs.

During pre-monsoon, the albedo difference between the urban and the rural area (midday albedo of 0.17 at urban site versus 0.24 at rural site; Fig. 5.9) increases the net energy absorbed by the city by increasing the shortwave radiation absorbed by the urban surface. This excess energy increases the surface temperature. For both pre-monsoon and post-monsoon seasons, the diurnal variation of $UHI_{surface}$ closely follows the urban-rural net radiation difference (Fig. 5.10). Urban structures have a high thermal mass, both due to their size and the high density materials used to construct them. This property allows the urban structures to absorb heat without appreciable change in temperature. Thus, even if the same amount of energy is incident on both an urban and a rural area, the heating rate of the urban area will be lower. Consequently, the urban surface also cools more slowly [39]. During night time, the net radiative energy stored during the day starts getting dissipated at a faster rate in the rural site, leading to a high night time $UHI_{surface}$ via faster cooling of the rural surface. But the total energy released by the urban site is higher, mainly due to the day time imbalance in R_{net}. This can be seen in the negative urban-rural R_{net} difference of approximately 10W/m^2 during pre-monsoon nights (Fig. 5.10). There is no appreciable difference in the incoming longwave or incoming shortwave radiation between the urban and the rural site during this season (Fig. **??**). However,

the urban-rural outgoing longwave radiation peaks during midday, which is a direct consequence of the peak $UHI_{surface}$ at this time (Fig. 5.10).

Unlike pre-monsoon, during monsoon, the incoming solar radiation is higher at the rural site during the first half of the day (Fig. 5.10). This could be due to two reasons. Firstly, urban centers tend to be cloudier than rural sites, which reduces solar insolation [134]. Secondly, as the urban area is a continuous source of high anthropogenic emissions, aerosol buildup after rainfall events over the city is fast compared to nearby rural regions. The increased radiative forcing due to high aerosol loading at urban sites has been seen in previous studies and may explain the observed disparity in the urban-rural R_{net} differences between the two seasons [20]. The increased cloudiness and high pollution load in the urban areas also leads to a high incoming longwave radiation, while the high $UHI_{surface}$ during this season explains the significant urban-rural outgoing longwave radiation difference seen in Figure 5.9. The diurnal trend in $UHI_{surface}$ does not explicitly follow the trend in R_{net} difference. This suggests that the $UHI_{surface}$ is largely controlled by how much energy gets dissipated from the surface during this season. The high latent heat flux at the rural site may lead to a large drop in the rural surface temperature, compared to the urban site, establishing this high $UHI_{surface}$ (maximum of 5°C). This can also be inferred from the sudden jump in $UHI_{surface}$ seen just after 0600 hrs during monsoon (Fig. 5.10), which coincides with the time when latent heat flux starts being a major dissipation term at the rural site (Fig. 5.26). The sun's energy facilitates evaporation of water from the moist rural surfaces at dawn during this season.

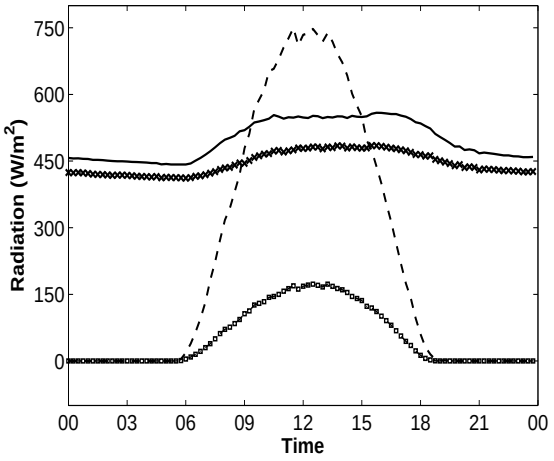

(A) Pre-monsoon-rural site

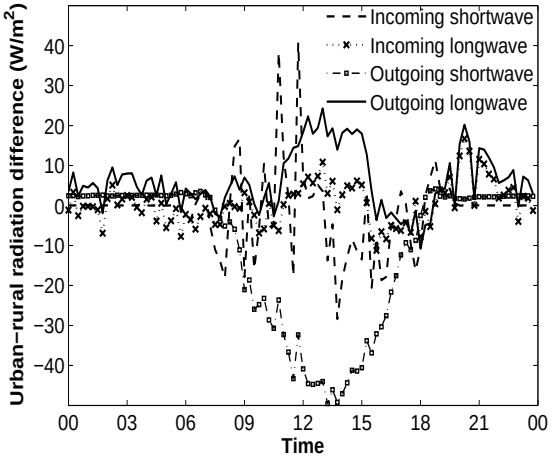

(B) Urban-rural differences in radiation components-pre-monsoon

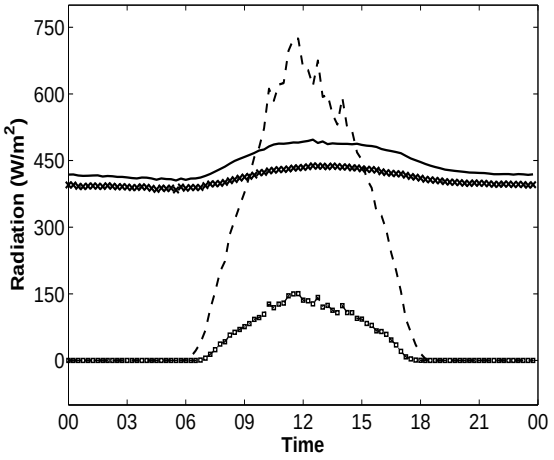

(C) Monsoon-rural site

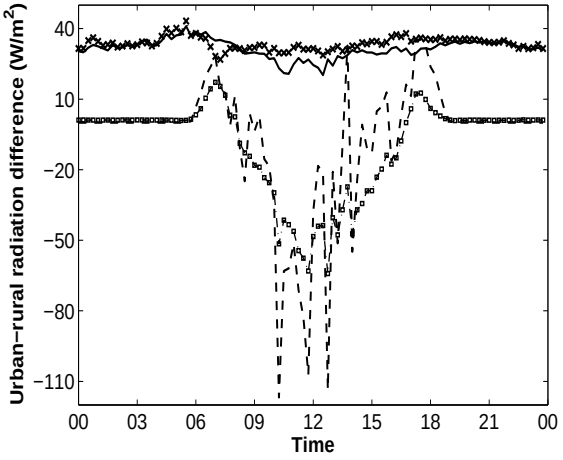

(D) Urban-rural differences in radiation components-monsoon

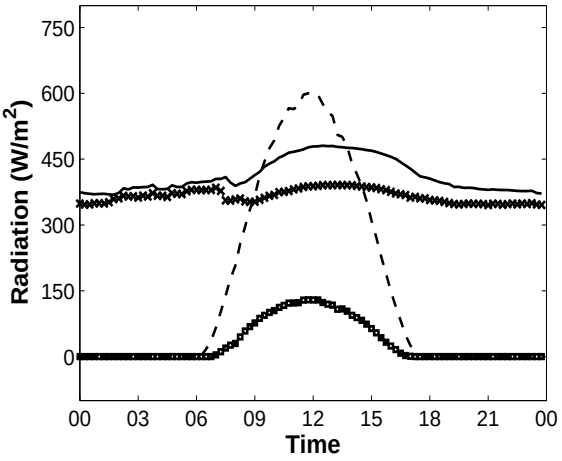

(E) Post-monsoon-rural site

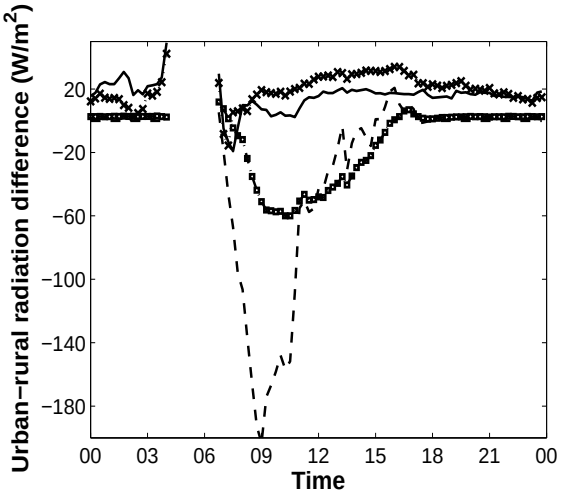

(F) Urban-rural differences in radiation components-post-monsoon

FIGURE 5.9: Inter-comparison of diurnal variation of radiation components at the two sites

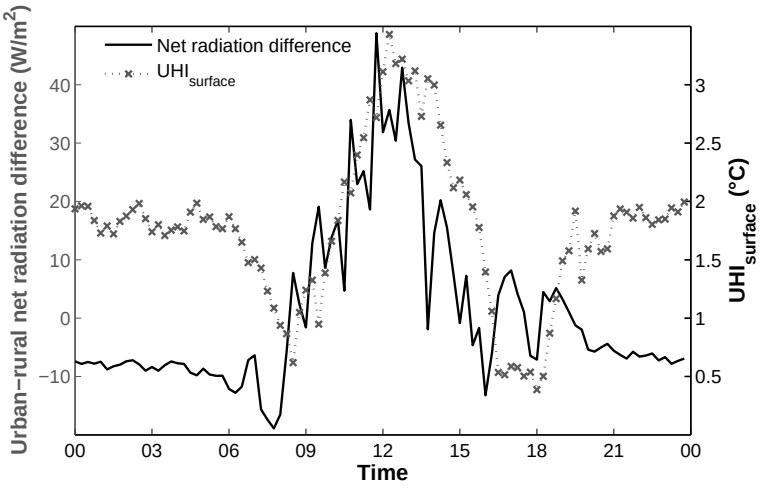

(A) Pre-monsoon

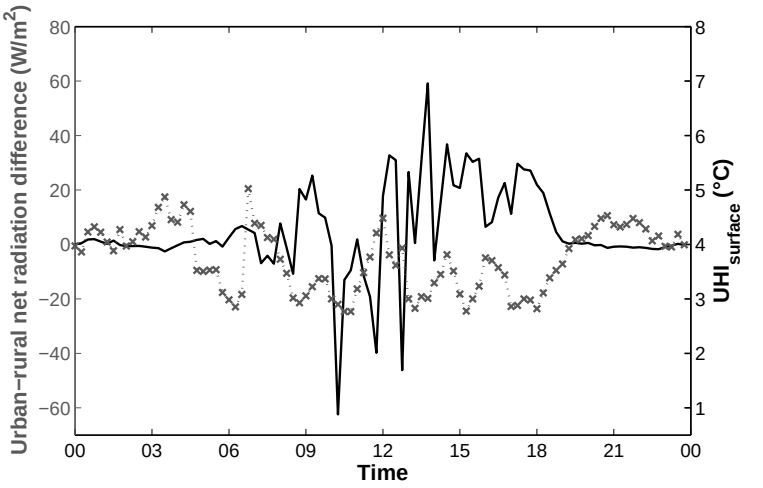

(B) Monsoon

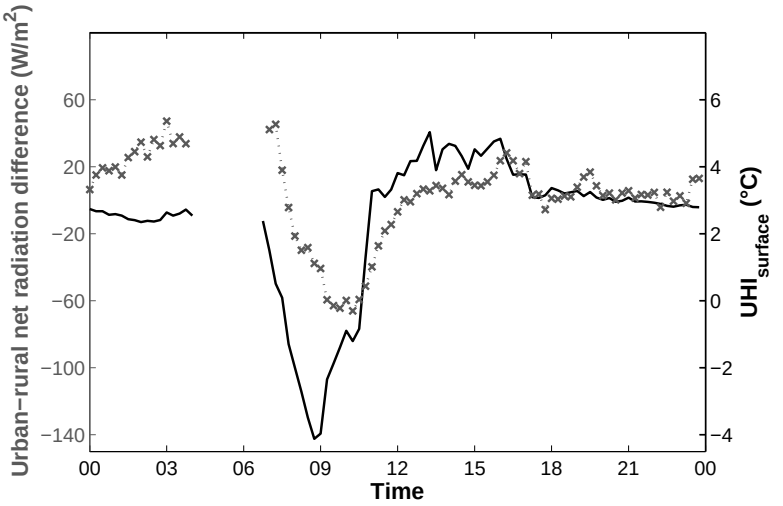

(C) Post-monsoon

FIGURE 5.10: Net radiation difference and $UHI_{surface}$

5.2.2 Urban wind speed and the UHI_{canopy}

Wind speed has an important influence on the air temperature, with advection reducing the build-up of heat and moderating temperature variances [113]. Urban wind speed was taken as a proxy for the advection of heat within the city, and was correlated with the urban-rural temperature difference using box plots. To make this analysis robust, this analysis was done for each of six wind direction ranges (0° to 60°, 60° to 120°, 120° to 180°, 180° to 240°, 240° to 300° and 300° to 360°). The correlation between UHI_{canopy} and urban wind speed shows an inverse relation for all six cases (Fig. 5.11). This is expected since higher urban advection removes the excess heat, thus bringing down the urban air temperature, and, consequently, the UHI_{canopy}. High wind speeds also seem to limit the highest and lowest possible (negative) UHI_{canopy}, while calm conditions show a higher variability in possible UHI_{canopy}. This is evident from the UHI_{canopy} standard deviations (σ_1) for the first and last bins in each wind direction range. The urban advection may also be responsible for the diurnality in the UHI_{canopy}. It is evident from Figure 5.12 that the wind speed is higher during day time compared to the night time, which could explain the diurnality seen in the UHI_{canopy}.

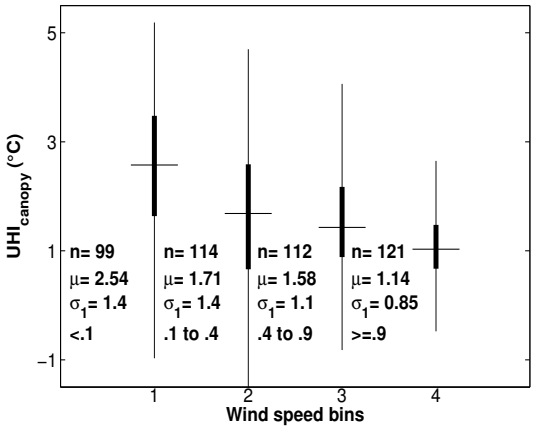

(A) Between 0° and 60°

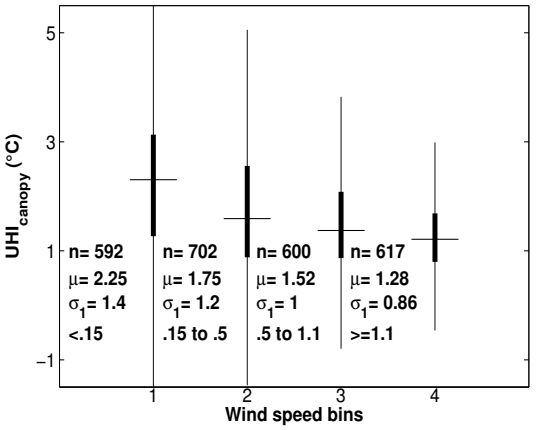

(B) Between 60° and 120°

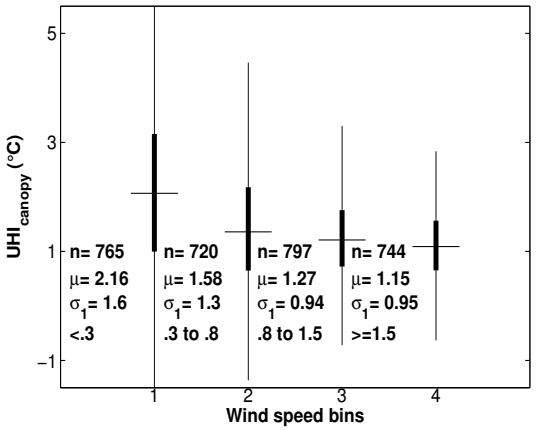

(C) Between 120° and 180°

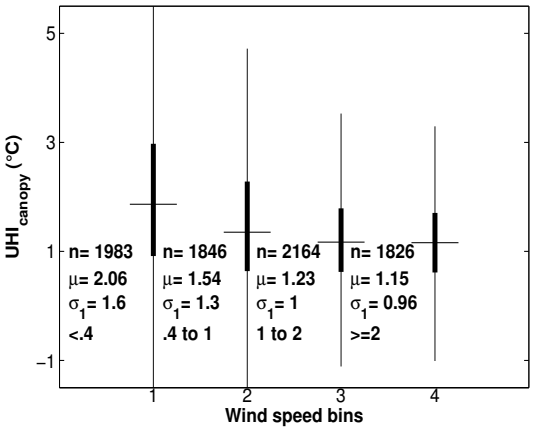

(D) Between 180° and 240°

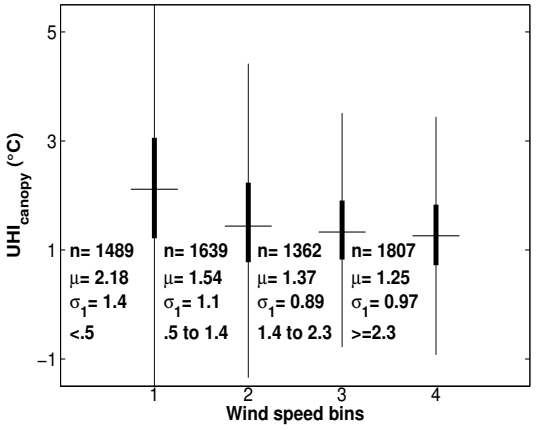

(E) Between 240° and 300°

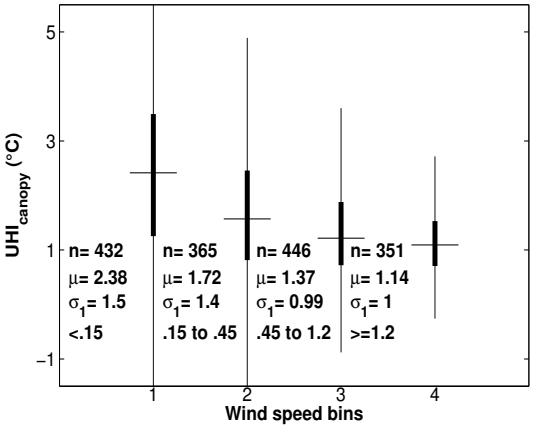

(F) Between 300° and 360°

FIGURE 5.11: Dependence of UHI_{canopy} on urban wind speed

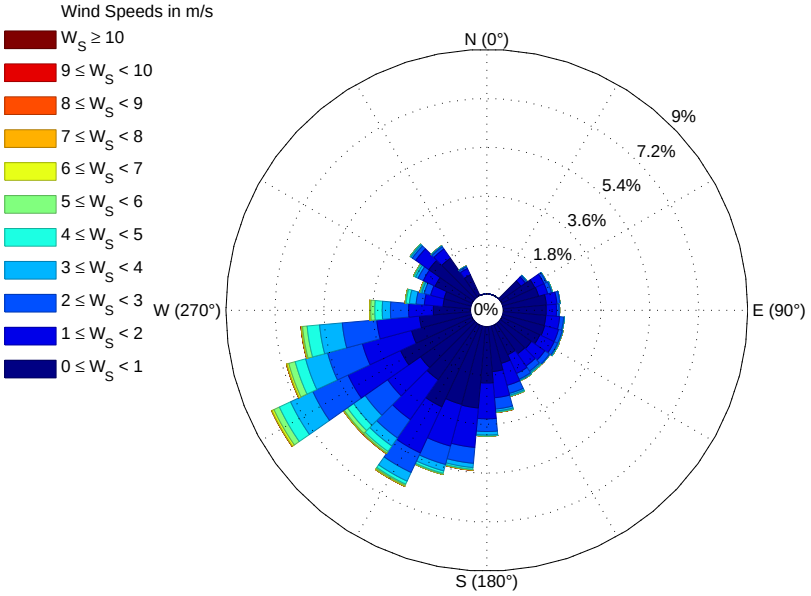

(A) Day time

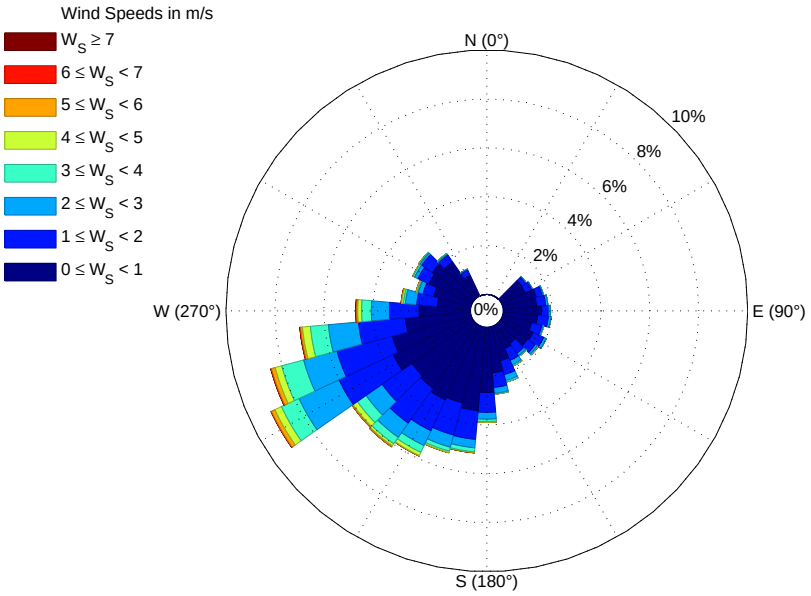

(B) Night time

FIGURE 5.12: Urban wind rose for entire study period

5.2.3 Radiation components and the UHI_{canopy}

Solar radiation and sensible heat flux being negligible during night time, the only source of heat into the canopy air is the longwave radiation. Thus, to understand the night time UHI_{canopy}, only the longwave radiation data was considered. For day time, both the longwave radiation as well as the modelled sensible heat flux data were taken into account. In both cases, the difference in outgoing and incoming longwave radiation between the urban and rural station was correlated with the UHI_{canopy} for ore-monsoon and monsoon. During night time, urban-rural longwave radiation differences (both incoming and outgoing) show strong correlations with the UHI_{canopy} magnitude (Fig. 5.13). As discussed earlier, the outgoing radiation difference is due to the existence of the $UHI_{surface}$ established during the day. At the same time, the incoming longwave radiation is also higher at the urban site because of the preexisting higher air temperature, presence of tall buildings that emit diffused radiation, and the increase in longwave radiation caused due to the high absorbing aerosol loading in the urban area [138].

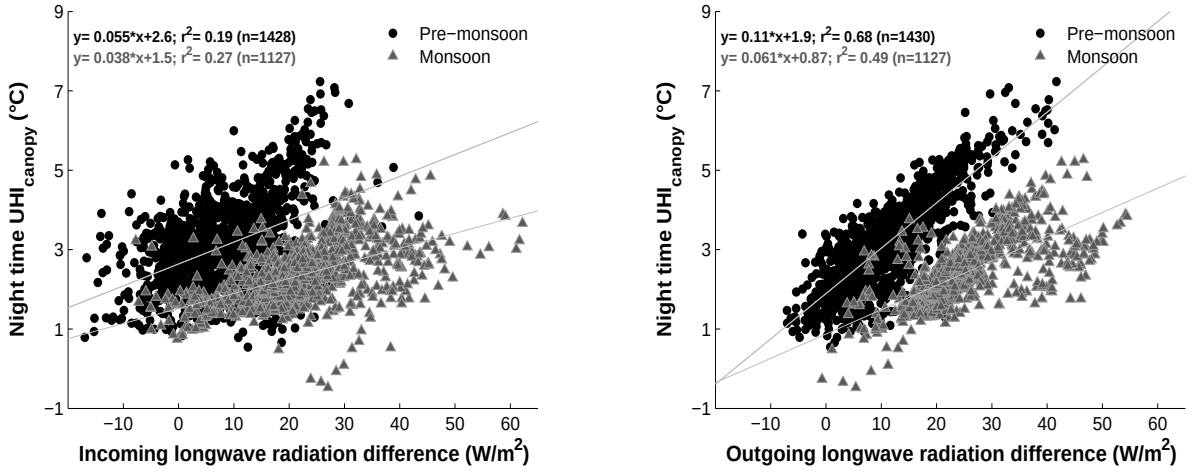

(A) Incoming longwave radiation vs night-time UHI_{canopy}

(B) Outgoing longwave radiation vs night time UHI_{canopy}

FIGURE 5.13: Longwave radiation difference vs night time UHI_{canopy}

The correlation between the outgoing radiation difference and the UHI_{canopy} is stronger during pre-monsoon nights, compared to monsoon nights (r^2=0.68 and slope=.11 vs r^2=0.49 and slope=0.06). Thus, the urban-rural outgoing longwave radiation difference has a stronger influence on the UHI_{canopy} during pre-monsoon. It also has a stronger effect on the variability of UHI_{canopy} for this season and thus largely controls the inter-seasonal difference in magnitude of the UHI_{canopy}.

The correlation between incoming longwave radiation difference and the UHI_{canopy} is weaker during pre-monsoon compared to monsoon, but the slope is greater (r^2=0.19 and slope=0.06 vs r^2=.27 and slope=0.04), albeit slightly. This indicates that the incoming longwave radiation difference has a stronger control on the UHI_{canopy} during pre-monsoon, though it has a lower influence on the variability of the phenomenon.

During the day, other factors, like sensible heat flux and conduction, also come into play, which limit the influence of longwave radiation on air temperatures (Fig. 5.14). However, a small degree of correlation is seen between the day time UHI_{canopy} and the longwave radiation differences (both outgoing and incoming). The correlation is even lower in case of pre-monsoon, mainly due to the greater turbulence in the atmosphere, which is also suggested by the NOAH model results (Fig. 5.26).

5.2.4 Sensible heat flux and the UHI_{canopy}

5.2.4.1 Model validation

To gain confidence about the NOAH-modelled sensible heat flux trends, the skin temperature and the temperature of the first soil layer simulated by NOAH is compared with measurements for both the urban and the rural site (Fig. 5.15, 5.16).

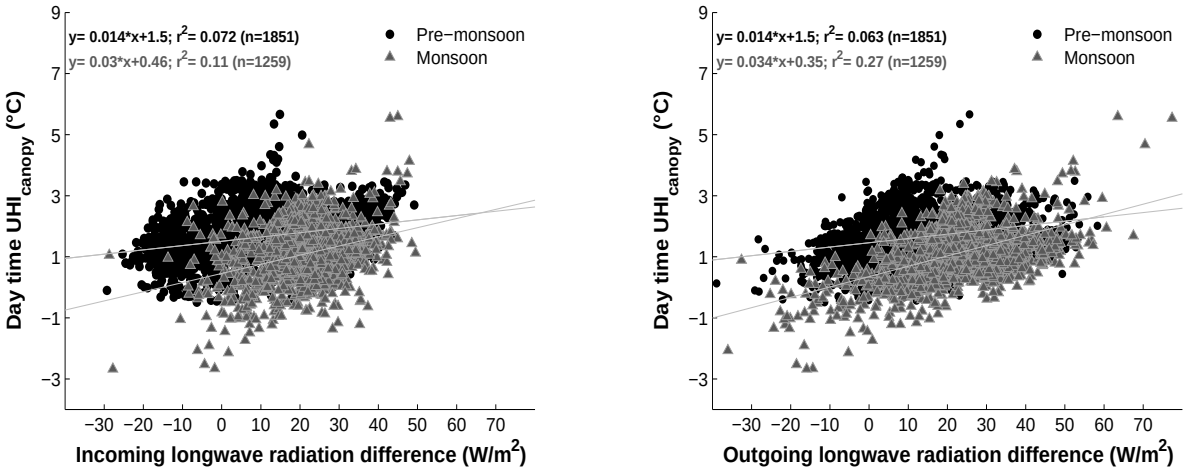

(A) Incoming longwave radiation vs day time UHI_{canopy}

(B) Outgoing longwave radiation vs day time UHI_{canopy}

FIGURE 5.14: Longwave radiation difference vs day time UHI_{canopy}

Field measurements indicate that both of these parameters increase throughout pre-monsoon and then start decreasing with the onset of monsoon. This trend is well-predicted by the model and even the magnitude of the modelled and observed values are close for the skin temperature (RMSE of 2.2 for the urban site and 3.8 for the rural site). The model slightly underestimates the skin temperature at both sites during pre-monsoon and overestimates it during monsoon. This overestimation of skin temperature by NOAH during Indian monsoon has been seen in a previous study [94]. Since the sensible heat flux depends on the surface-air temperature gradient, the model will overestimate the sensible heat flux during pre-monsoon and underestimate it during monsoon. Since this is systematic for both sites, there is reasonable certainty about the comparison between the urban-rural sensible heat flux trends using NOAH-simulated data. The modelled soil temperature is overestimated for the urban site and underestimated for the rural site during both seasons. Thus, the NOAH-simulated soil flux is underestimated for the urban area and overestimated for the rural area.

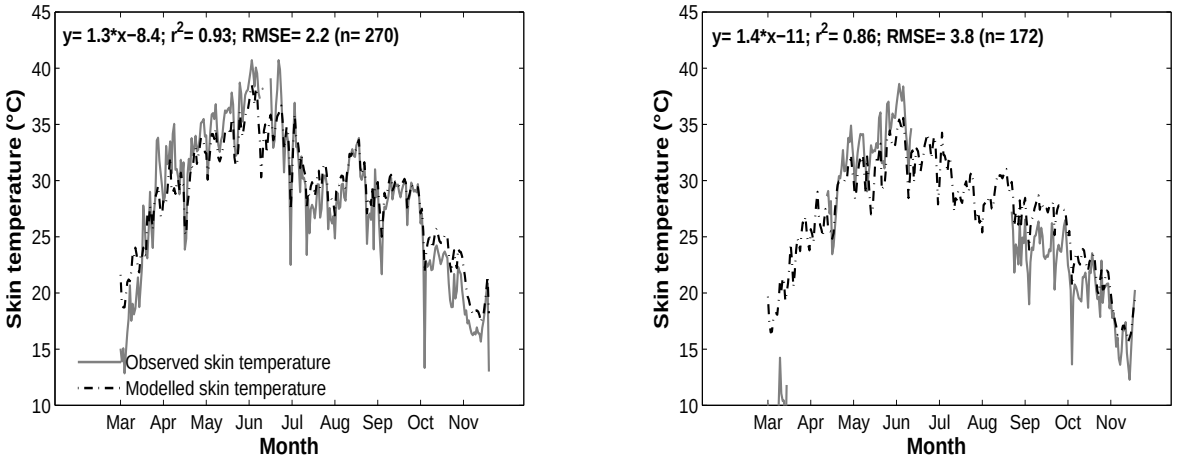

(A) Urban site (B) Rural site

FIGURE 5.15: Validation of NOAH-modelled daily skin temperature

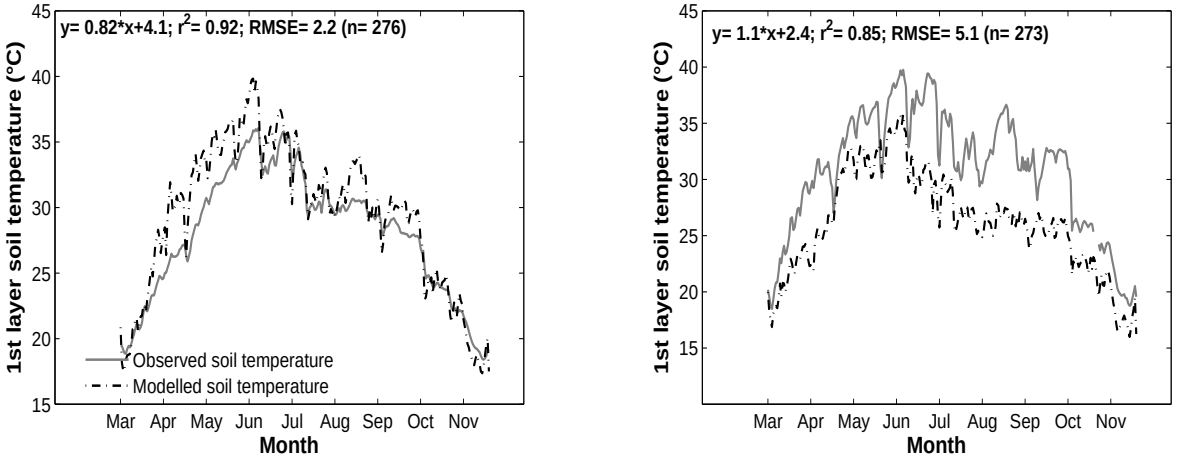

(A) Urban site (B) Rural site

FIGURE 5.16: Validation of NOAH-modelled daily 1st layer soil temperature

Given the scarcity of NOAH validation studies in the country, this evaluation of the model over a humid monsoonal region is important even beyond the scope of the present study - to improve model parameterization in such climate zones and contribute to the development of the model physics. Thus, evaluations are also performed for the daily soil temperature at the other depths, soil moisture at four depths and net radiation for both the sites.

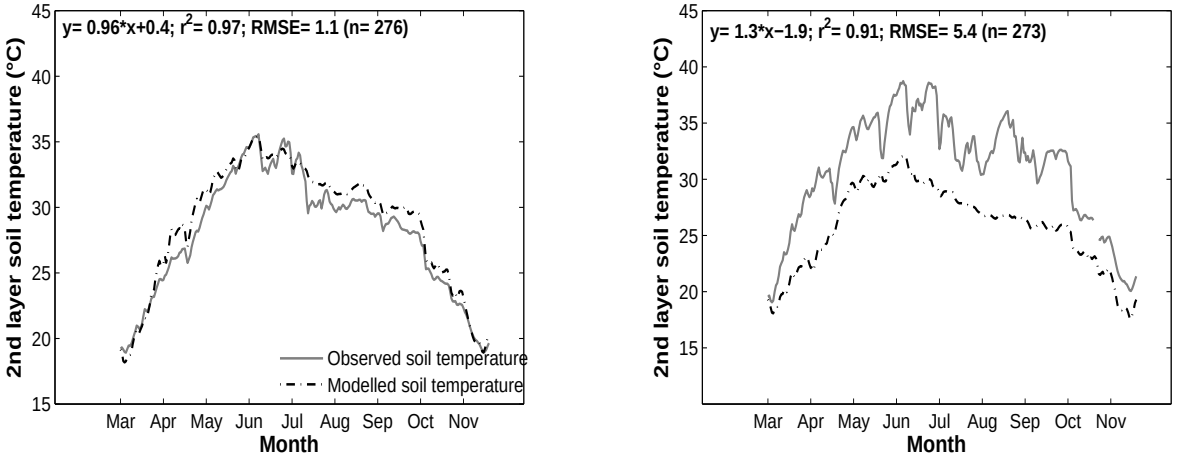

(A) Urban site (B) Rural site

FIGURE 5.17: Validation of NOAH-modelled daily 2nd layer soil temperature

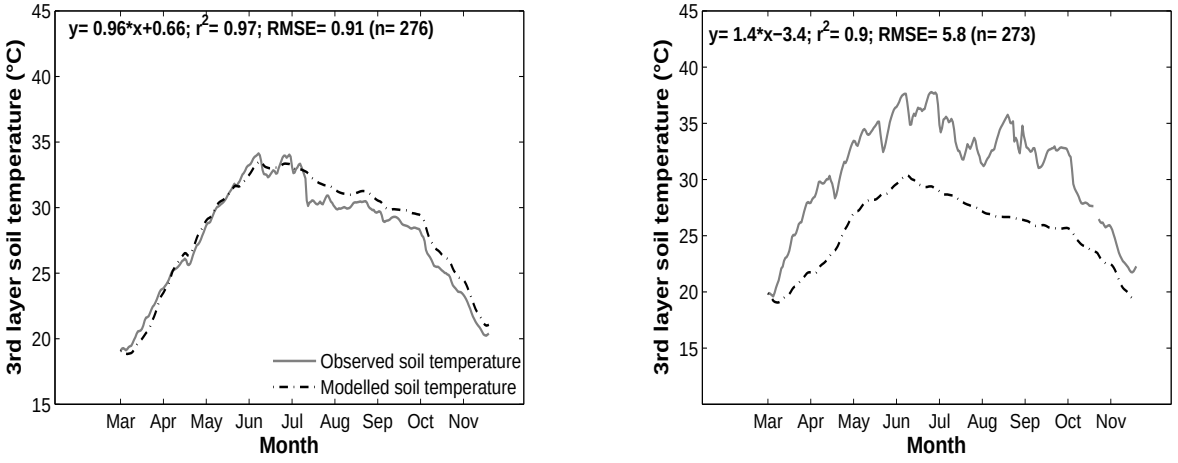

(A) Urban site (B) Rural site

FIGURE 5.18: Validation of NOAH-modelled daily 3rd layer soil temperature

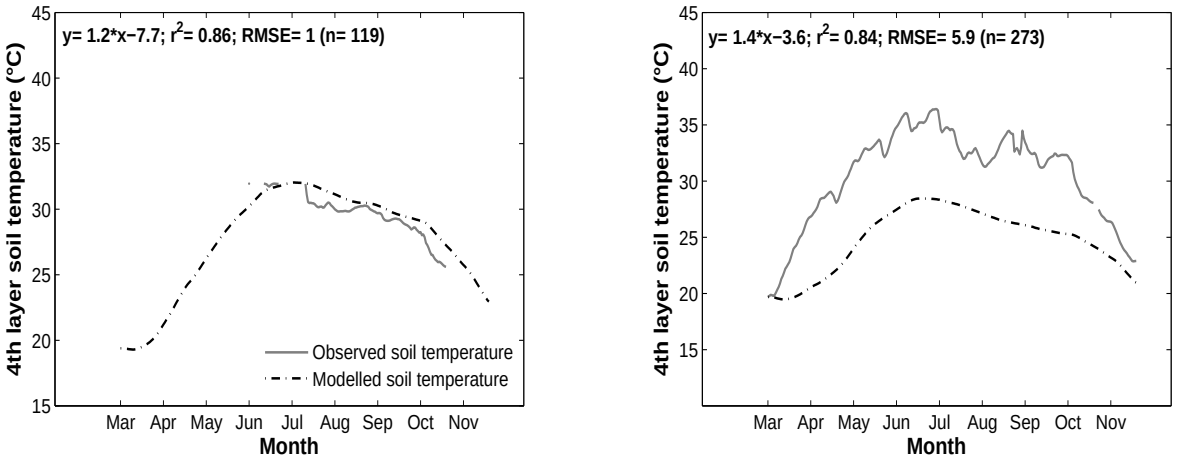

(A) Urban site (B) Rural site

FIGURE 5.19: Validation of NOAH-modelled daily 4th layer soil temperature

The soil temperature at the other depths also follow a similar trend, and are simulated well by the model. For the urban site, the simulation improves with depth, since the RMSE, which is a measure of the difference between the simulated and the observed values, decreases with depth. For the rural area, the opposite is seen.

For the urban area, the soil moisture trend shows a sharp increase at the onset of monsoon, following the rainy events during the period. For the rural site, the soil moisture does not exhibit such a sharp change, and remains more or less same for all three seasons. This could be due to the effect of irrigation on the soil moisture. NOAH simulates the 1st layer soil moisture at the urban area well, but underestimates the soil moisture at the rural site during the dry season. For the deeper layers, the soil moisture simulations do not match well with the observed data.

The simulated net-radiation values match well with the observed values for both the sites. The observed values show more peaks due to the effect of missing data on the daily averages.

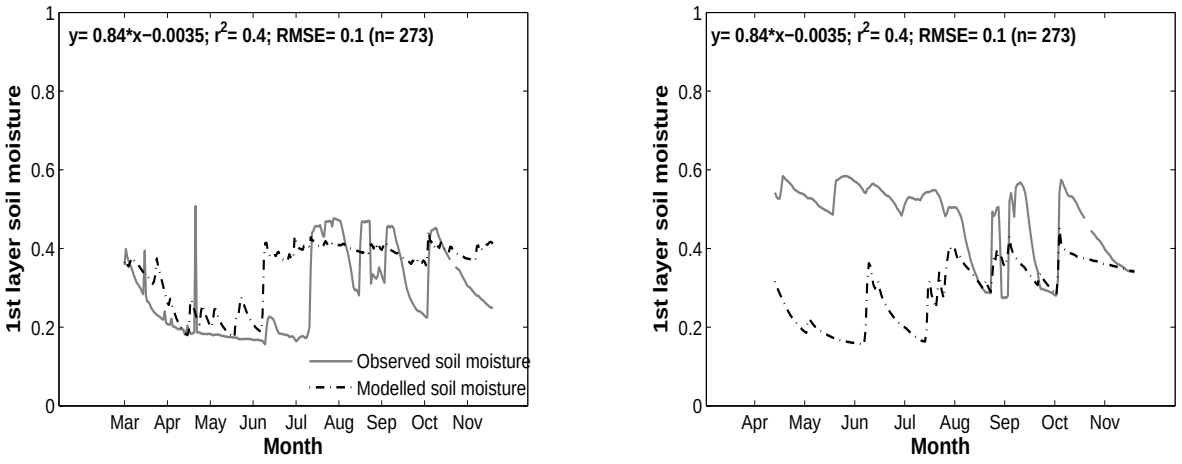

(A) Urban site (B) Rural site

FIGURE 5.20: Validation of NOAH-modelled daily 1st layer soil moisture

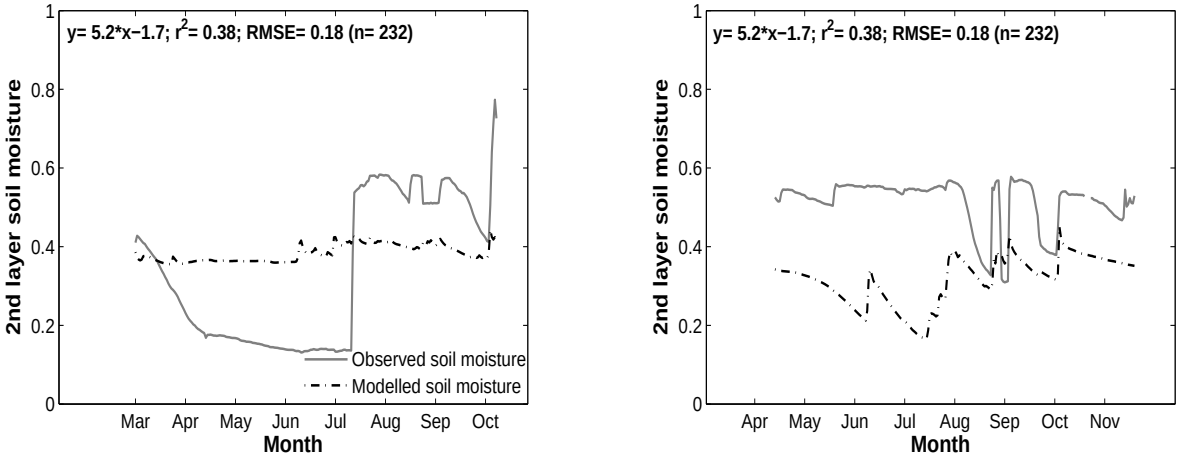

(A) Urban site (B) Rural site

FIGURE 5.21: Validation of NOAH-modelled daily 2nd layer soil moisture

5.2.4.2 Model results

The urban-rural sensible heat flux differences were correlated with the UHI_{canopy} for day time. Low correlations are found for both seasons (r^2=0.04 for pre-monsoon and r^2=0.03 for monsoon), possibly because the day time atmospheric factors, like advection and vertical mixing, make it harder to single out individual causes. The

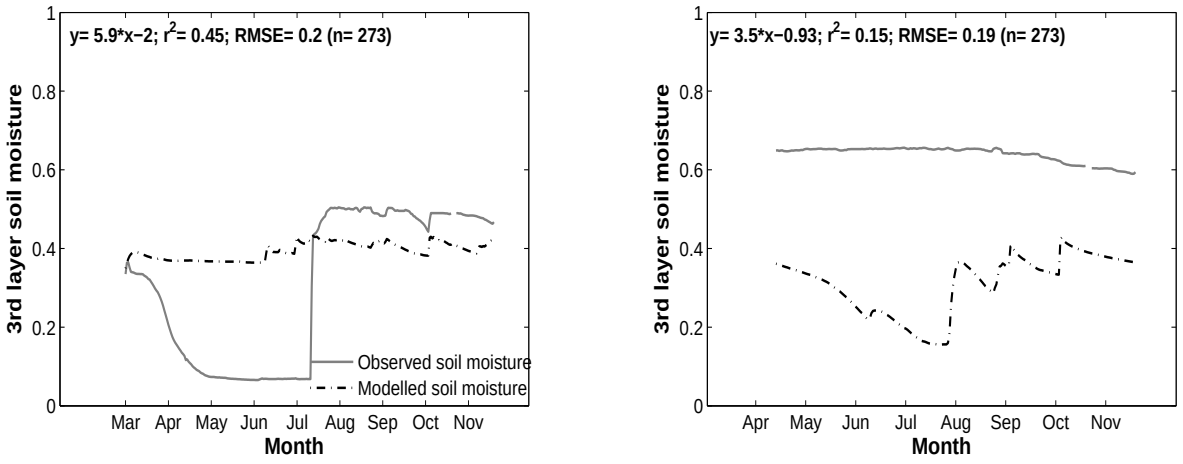

(A) Urban site (B) Rural site

FIGURE 5.22: Validation of NOAH-modelled daily 3rd layer soil moisture

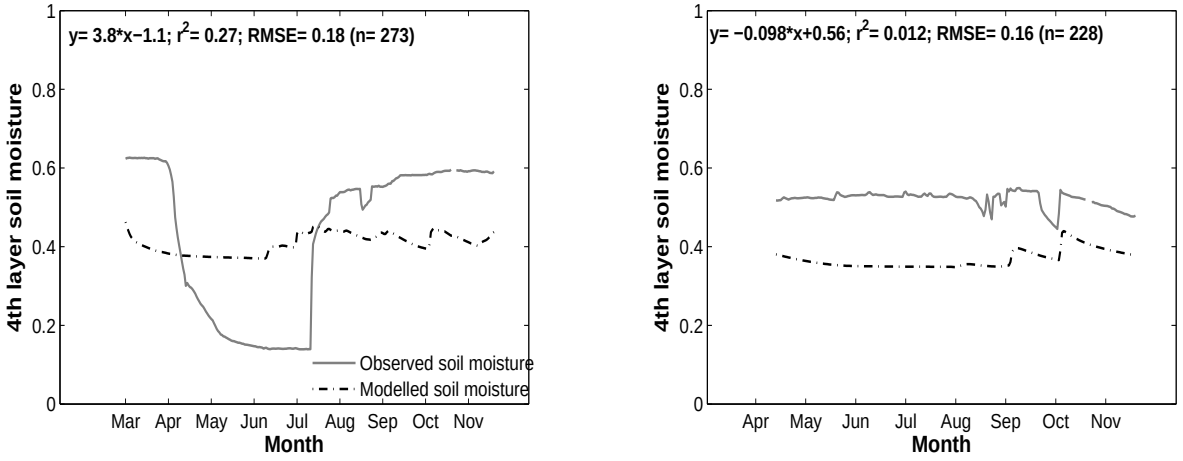

(A) Urban site (B) Rural site

FIGURE 5.23: Validation of NOAH-modelled daily 4th layer soil moisture

regression analysis (Fig. 5.25) and the diurnal plots suggest that there is an inverse relationship between the sensible heat flux difference and the UHI_{canopy}. This is in spite of a positive relation seen between sensible heat flux and day time canopy temperature (Fig. 5.26). The only exception is for the rural site during monsoon, where, no significant correlation is seen between sensible heat flux and the day time canopy temperature on account of the dominance of latent heat flux in the rural area

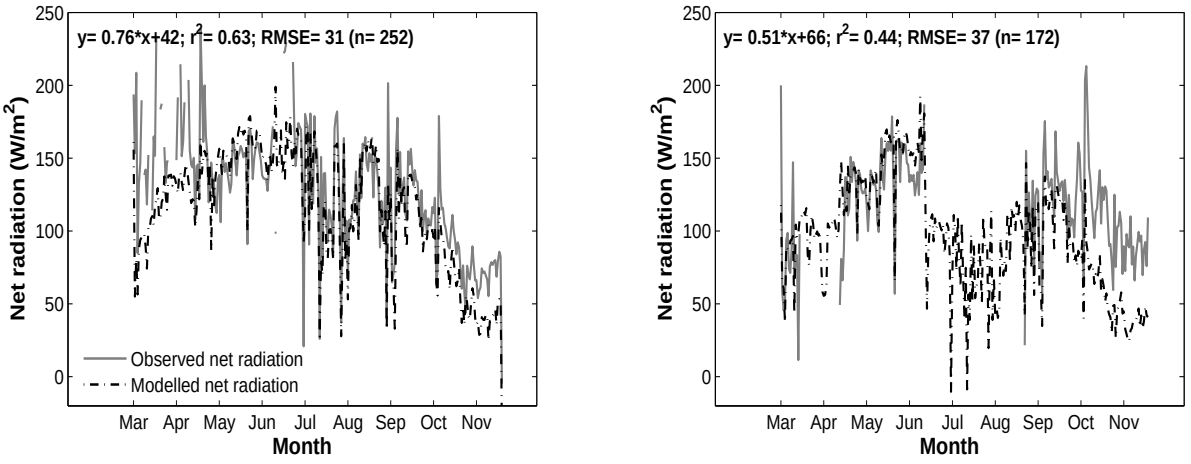

(A) Urban site (B) Rural site

FIGURE 5.24: Validation of NOAH-modelled daily net radiation

throughout the season. Thus, though the turbulent transfer of sensible heat leads to an overall heating of the boundary layer, there are caveats to this, especially when comparing an urban area to a rural one. On one hand, the relationship between the air temperature and the boundary layer heating is a function of the aerodynamic resistance of the surface layer [40]. On the other hand, the higher sensible heat flux at the urban site increases the height of the mixing layer, thus moderating the heating of air at a particular height from the surface [14]. These two factors lead to a difference in the convection efficiency between urban and rural areas, which diminishes UHI_{canopy} during day time, which was also suggested by Zhao [137].

Considering the decreasing UHI_{canopy} and the low correlations between the radiation terms and the heat island during the day, it is apparent that the UHI_{canopy} is primarily a night time phenomenon, and its residue is observed during the day.

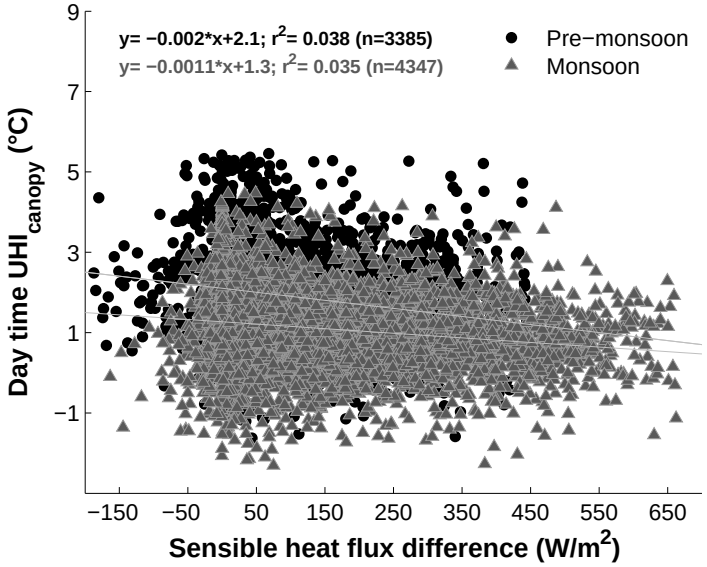

FIGURE 5.25: Sensible heat flux difference vs day time $\mathrm{UHI}_{\mathrm{canopy}}$

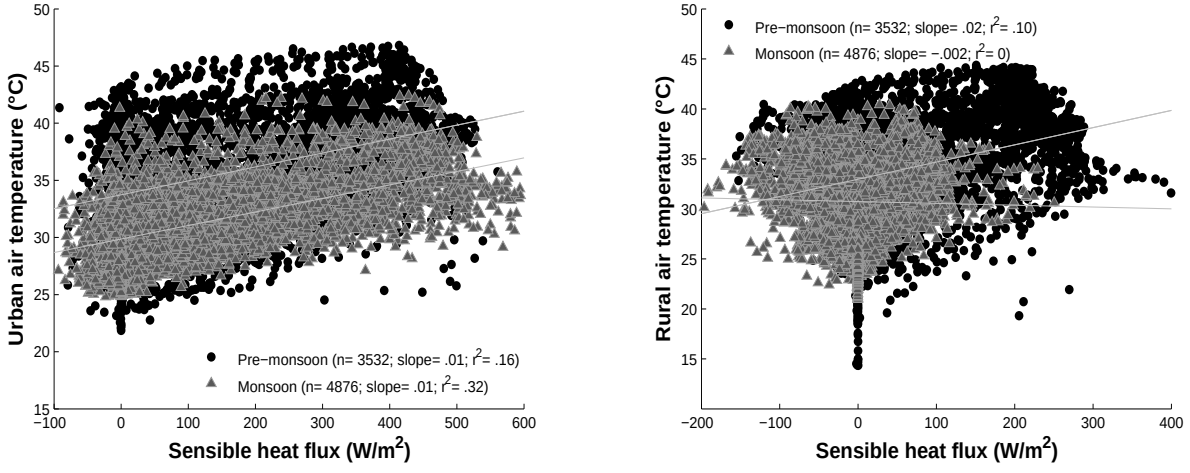

(A) Urban site (B) Rural site

FIGURE 5.26: Temperature response to sensible heat flux during night time

5.2.5 Factors responsible for the inter-seasonality of the UHI

To understand the factors affecting the inter-seasonality of the UHI_{canopy} between pre-monsoon and monsoon, the surface energy partitioning and the longwave radiation were investigated. The simulated partitioning from the NOAH runs show that the sensible heat flux dominates in the urban area for both monsoon (midday sensible heat flux of 314±179 W/m^2 vs latent heat flux of 105±90 W/m^2) and pre-monsoon (midday sensible heat flux of 378±108 W/m^2 vs latent heat flux of 93±75 W/m^2) (Fig. 5.27), while the latent heat flux dominates in the rural area during monsoon (midday latent heat flux of 322±163 W/m^2 vs sensible heat flux of 21±57 W/m^2); and to a lesser degree, during pre-monsoon (midday latent heat flux of 248±95 W/m^2 vs sensible heat flux of 169±100 W/m^2). This is primarily due to the lack of vegetation in the urban area, which limits the possible evapotranspiration from the surface. On the other hand, the rural area shows a greater variation in the partitioning between pre-monsoon and monsoon (midday Bowen ratio of 0.7 in pre-monsoon vs 0.07 in monsoon). This can be attributed to the seasonal land use changes in the rural area. During pre-monsoon, the rural surface is relatively barren, since the rabi crops are harvested between March to April [136]. Thus, the surface energy partitioning of both the sites are similar during this season. However, there is a stark difference between the vegetation amount between pre-monsoon and monsoon for the rural area. The beginning of the khariff cropping season in July and the wild, rapid growth of flora due to the monsoon rains contributes to this inter-seasonality. The model results confirm this, as the sensible heat flux remains almost zero throughout the day in the rural area, with almost all the energy being dissipated as latent heat flux during monsoon. This partitioning of the fluxes may be responsible for the lower UHI_{canopy} during this season, since latent heat flux dissipates the excess heat from the Earth's surface without increasing the temperature

of the air above it. Interestingly, the high latent heat flux may also account for the greater $UHI_{surface}$ during monsoon by cooling down the rural surface and creating a stronger surface temperature difference between the two locations.

The surface flux partitioning for the urban area during post-monsoon is the opposite, with the latent heat flux dominating over the sensible heat flux and a midday Bowen ratio of .15. This could be because the urban area responds late to the monsoon season, because the region remains dry through the major part of monsoon and starts showing vegetation growth at the end of the season, which affects the evapotranspiration during post-monsoon. Moreover, during 2014, there was an extreme rainfall event in September, which caused water-logging at the urban field where the AWS was located, which may also contribute to the high latent heat flux at the urban site during the season. The lower latent heat flux in the rural area in post-monsoon compared to monsoon, in spite of the heavy rainfall during that season, is a consequence of the reduction in vegetation cover in October with the harvesting of the khariff crops.

The response of the air temperature to the night time outgoing longwave radiation shows a greater inter-seasonal variation in case of the rural area (Fig. 5.28). This is on par with the inter-seasonality seen in the energy flux partitioning in the rural area and is due to the change in the rural landscape between pre-monsoon and monsoon. The range of the values of outgoing longwave radiation is similar in both the sites for pre-monsoon (approximately 400 W/m^2 to 600 W/m^2). However, for monsoon, the rural site shows much lower value (as low as 370 W/m^2 vs over 400 W/m^2 for the urban site). Since emitted longwave radiation is proportional to the surface temperature, this supports the proposition that the high $UHI_{surface}$ during monsoon is primarily due to the much lower temperature of the rural surface, possibly due to the high dissipation of heat through evapotranspiration. Evidently,

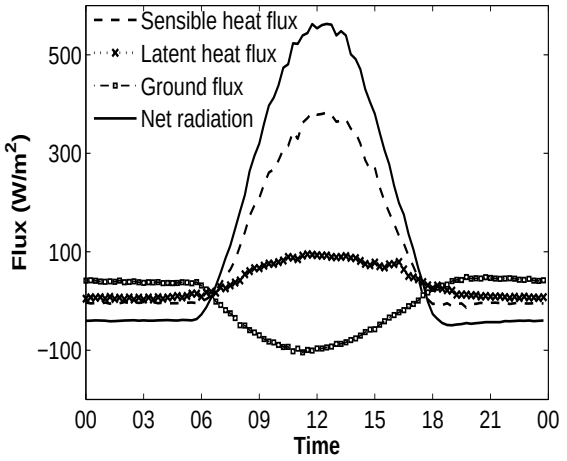

(A) Pre-monsoon-urban site

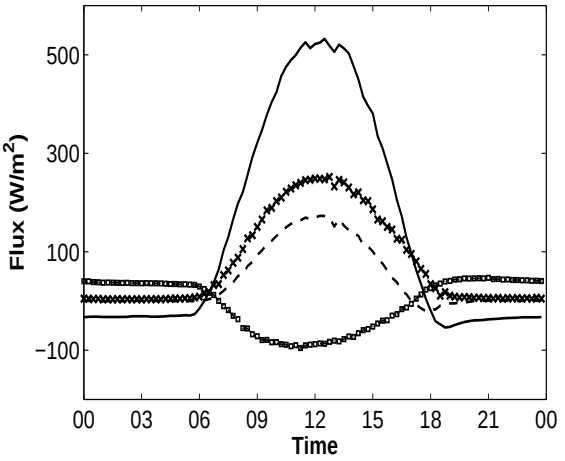

(B) Pre-monsoon-rural site

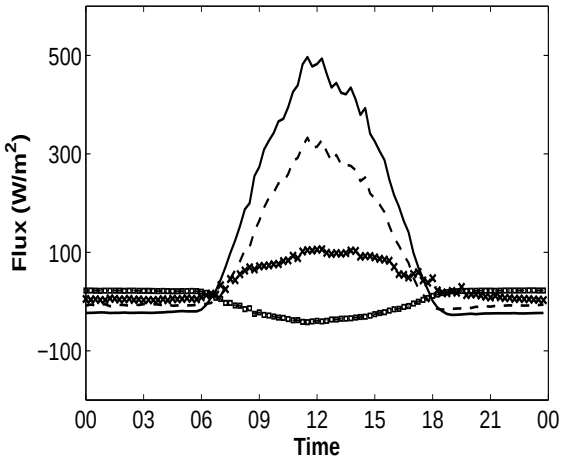

(C) Monsoon-urban site

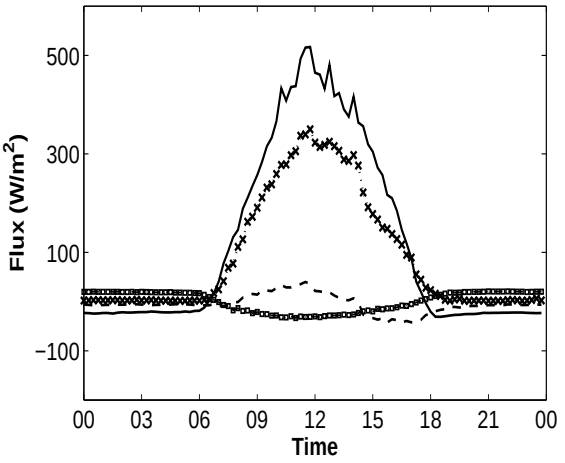

(D) Monsoon- rural site

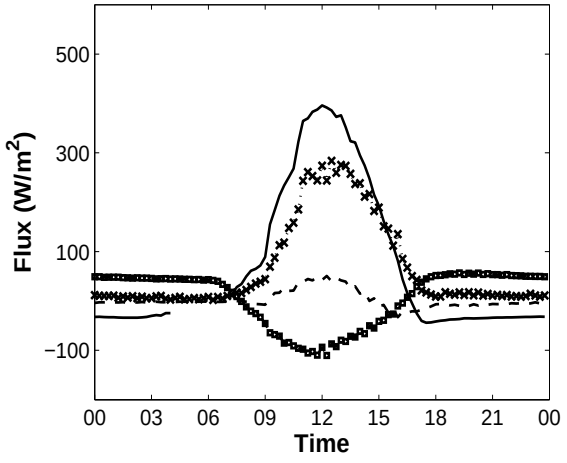

(E) Post-monsoon-urban site

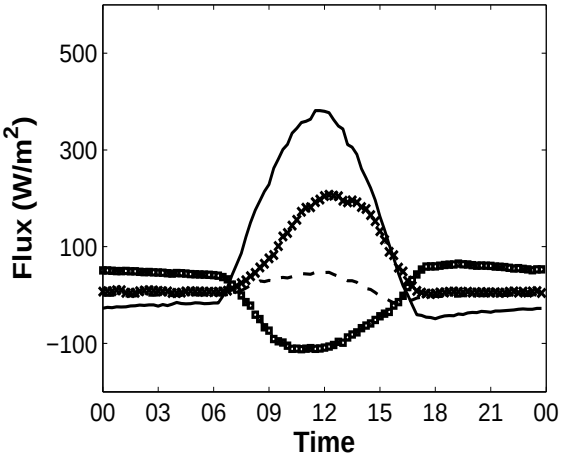

(F) Post-monsoon-rural site

FIGURE 5.27: Diurnal variation in surface flux terms

the inter-seasonality in the night time UHI_{canopy} and $UHI_{surface}$ magnitude is largely controlled by the seasonal characteristics of the rural area.

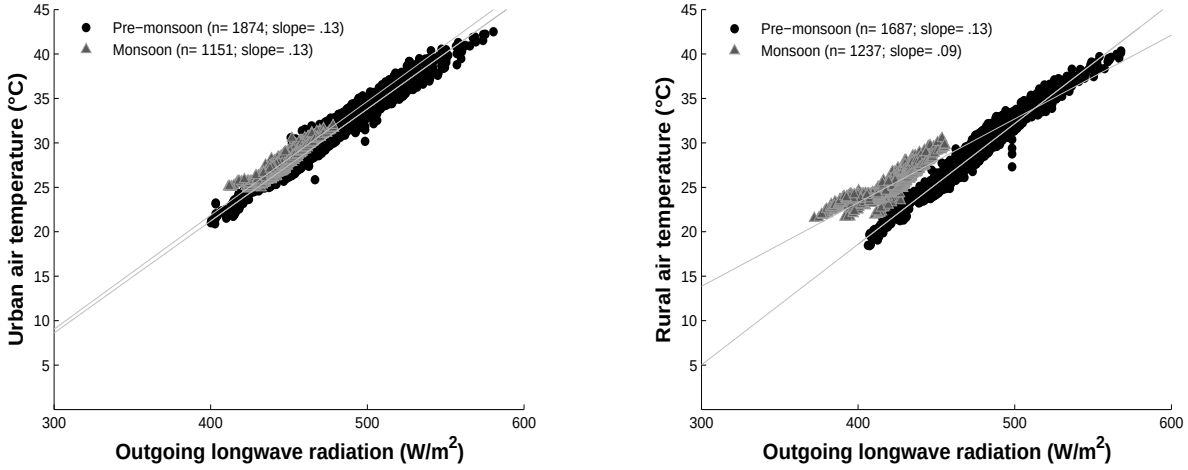

(A) Urban site (B) Rural site

FIGURE 5.28: Temperature response to outgoing longwave radiation during night time

5.3 Surface flux partitioning - temporal and spatial aspects

The concluding part of this study investigates the surface fluxes over both the urban and the rural site, from March, 2014 to November, 2014, and the intra-urban variance in surface energy partitioning. The results from the NOAH runs were used for the first part of the study, while simultaneous BREB measurements over an asphalt surface, an urban park and a rural field were used for the second part.

10-day averaged time-series plots of the modelled (for sensible, latent and ground flux) and measured (for net radiation) energy fluxes are shown in Figure 5.29. The energy partitioning in the rural site is typical of a humid subtropical region like

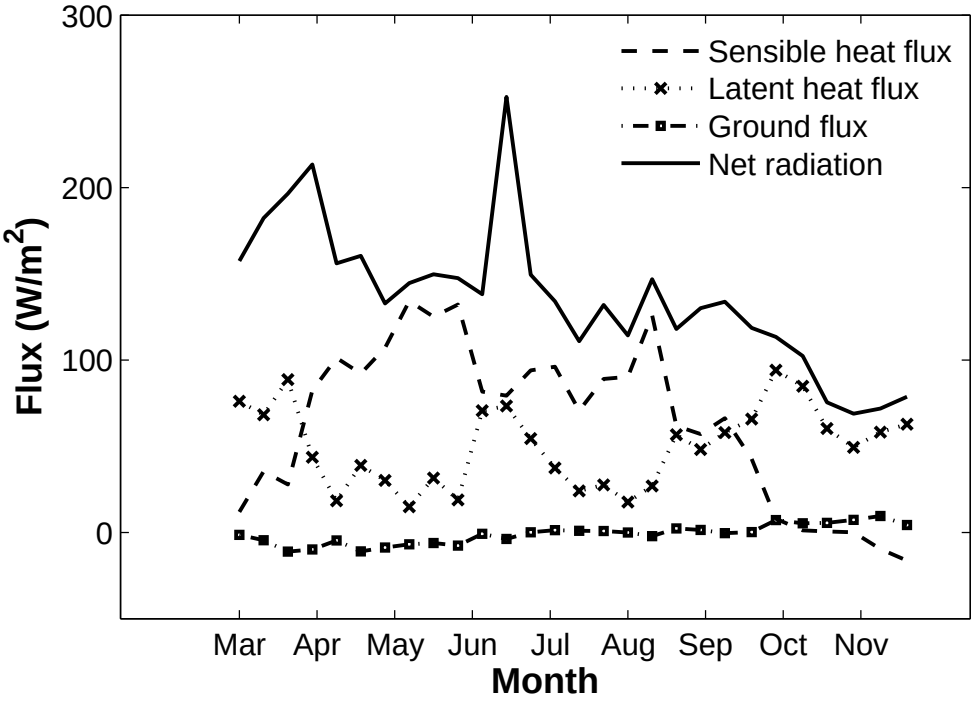

(A) Urban site

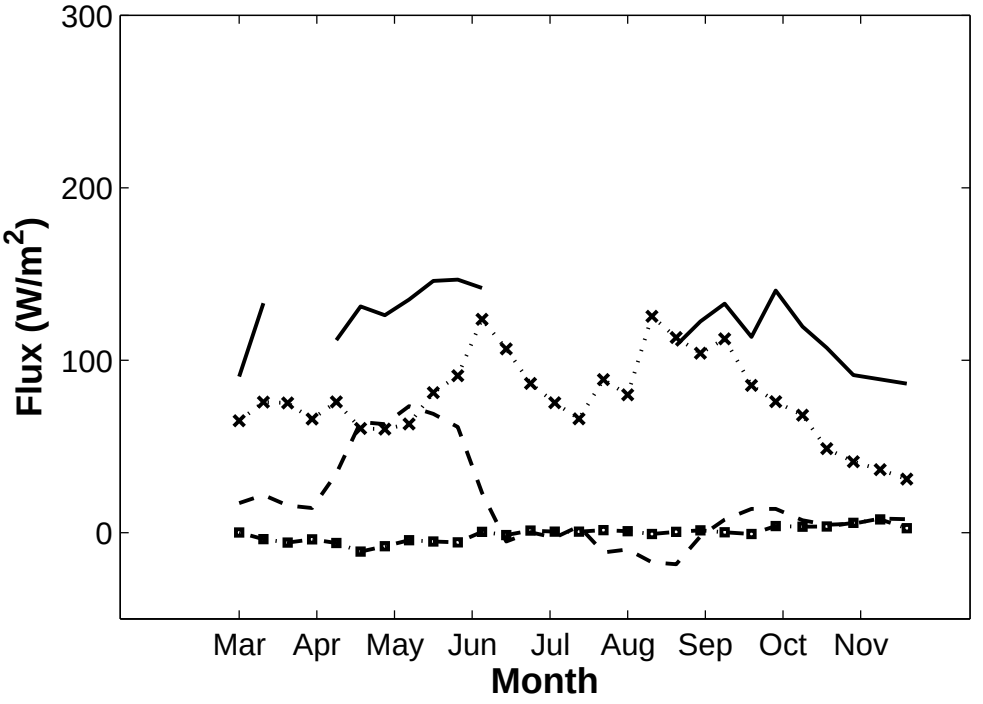

(B) Rural site

FIGURE 5.29: Variation of surface fluxes over the study period

Kanpur [128]. The latent heat flux dominates for almost throughout the study period, with a short-term reversal in May during the dry pre-monsoon. For the other seasons included in the study, the sensible heat flux remains almost negligible. The partitioning for the urban site shows that the sensible heat flux dominates from the beginning of the dry season up to the end of monsoon. During post-monsoon, the latent heat flux starts dominating. This is consistent with the diurnal pattern of the fluxes during the three seasons (Fig. 5.27). The urban area, being drier and less vegetated compared to the rural site, shows lower latent heat. However, during post-monsoon, when the park starts water-logging due to the extreme rainfall event, the latent heat flux increases and becomes comparable to that at the rural site.

Both the urban and the rural grasslands show similar surface energy partitioning during this period (Fig. 5.30). This is because the experiments were performed in October, during which, as mentioned earlier, the urban site was waterlogged. On the other hand, the asphalt showed a much higher sensible heat flux, and a Bowen ratio value close to unity. The asphalt surface remains relatively dry, since water is removed via surface drainage, causing higher sensible heat flux. This suggests that the dissipation of energy from the urban surface is dynamic and dependent on the particulars of the surface type. So, both the atmospheric as well as the land forcing becomes important in the context of urban studies since both of them influence the near-surface atmospheric dynamics.

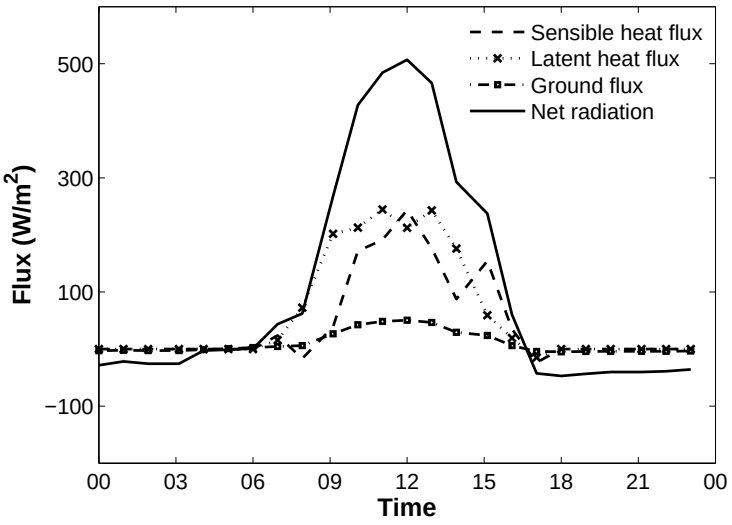

(A) Asphalt

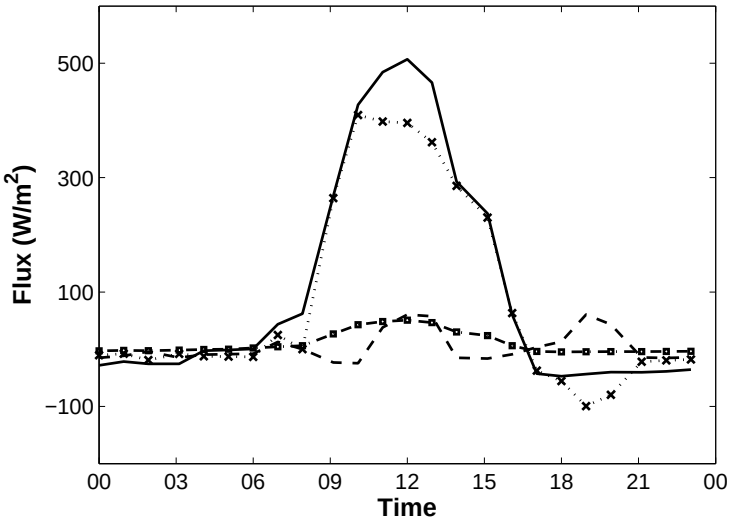

(B) Urban park

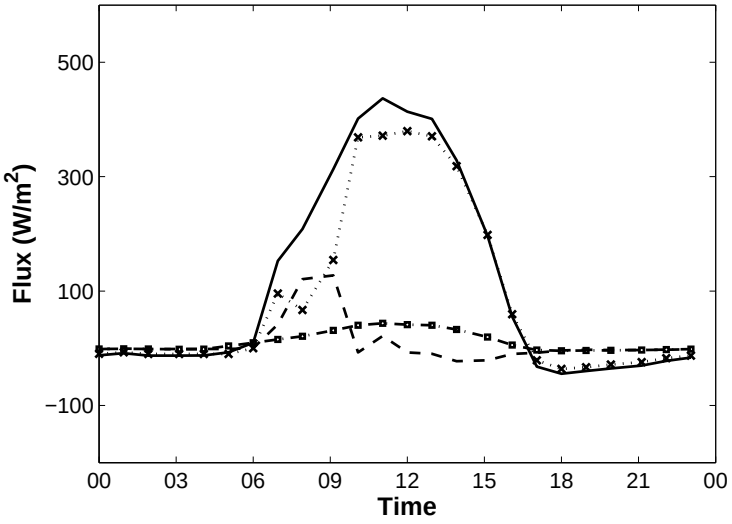

(C) Rural field

FIGURE 5.30: Surface flux partitioning over different land use types

Chapter 6

Conclusions and future work

6.1 Conclusions

Kanpur city shows a significant UHI_{canopy}, mainly during the night, with values being higher during the pre-monsoon season. The $UHI_{surface}$ also shows the same diurnality, except during pre-monsoon. The $UHI_{surface}$ forms due to the difference in net radiation between the urban and the rural site, which, in turn, is due to the difference in albedo, the difference in cloud cover and higher aerosol radiative forcing over the urban zone. The surface temperature gets dissipated at night as longwave radiation, and leads to differential cooling between the rural and the urban area, thus establishing the UHI_{canopy}. The temperature anomaly persists throughout the day, but may get reduced due to the difference in convective efficiency between the urban and the rural area, as well as advection, which is more prominent during the day time. Since air temperature is affected by horizontal as well as vertical gradients (through advection and convection respectively), the measure of the UHI_{canopy} magnitude is an aggregate of the nearby area, and varies throughout the city. This is seen in the results from the seasonal mobile campaigns and also evident from the BREB

experiment over two different surface types within an urban zone. The surface temperature derived from the MODIS Terra and Aqua LST datasets also shows a similar spatial pattern, and confirm that $UHI_{surface}$ is also a night time phenomenon and dependent on the faster heat dissipation in the rural area. Consequently, the rural area also heats up faster, leading to an urban cool island during the early part of the day.

The inter-seasonality of the canopy heat island is ascribed to the seasonal land use change of the rural area between pre-monsoon and monsoon. This is seen in both the outgoing longwave radiation, which plays a major role in the canopy air temperature, and the surface flux partitioning during the daytime, which controls the form in which the heat is dissipated from the surface to the canopy air. The surface flux partitioning also affects the inter-seasonality of the $UHI_{surface}$, with higher values during monsoon due to the dissipation of energy in the rural area through latent heat flux.

6.2 Scope of future work

The study did not attempt to quantify the factors responsible for the UHI during post-monsoon and winter, mainly due to the lack of data, though some relation was seen between the net radiation difference and the $UH_{surface}$. The effect of foggy winter nights on the UHI magnitude could be another interesting topic of investigation. Since the study concentrated on the fundamental micrometeorological factors affecting the UHI intensity, the effects of the city and its contributions, like anthropogenic heat flux, urban canyon effect, pollution loading, etc. were not directly investigated.

Studying the contribution of these factors to the UHI effect can improve understanding of the phenomenon and provide a more complete picture of its influences

on Kanpur city. The radiative forcing being dependent on both aerosols (direct) and clouds (indirect), a study on the relative contribution of the two will be highly informative. Similarly, understanding the urban geometry of Kanpur city and how that dictates the absorption and release of radiation from the urban fabric should also yield some interesting results. Lastly, given the huge population, the vehicle load and the industrial nature of the city, the impact of the anthropogenic heat flux on the temperature anomaly is also important.

Appendix A

Sensor calibration and correction

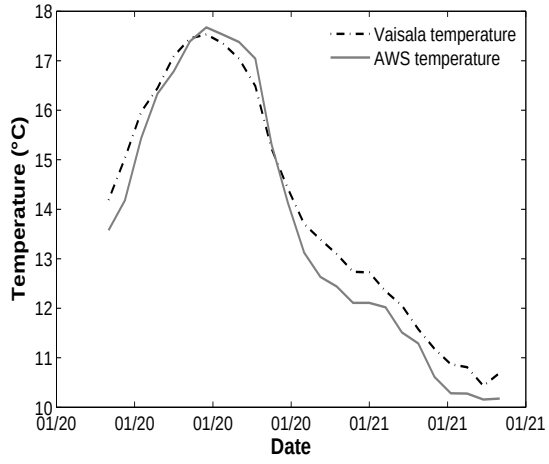

(A) Variation - temperature

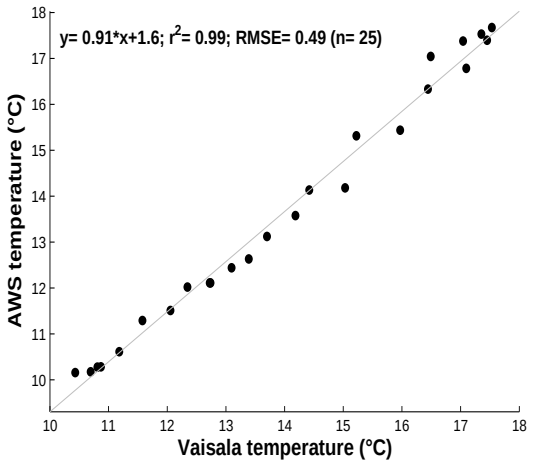

(B) Correlation - temperature

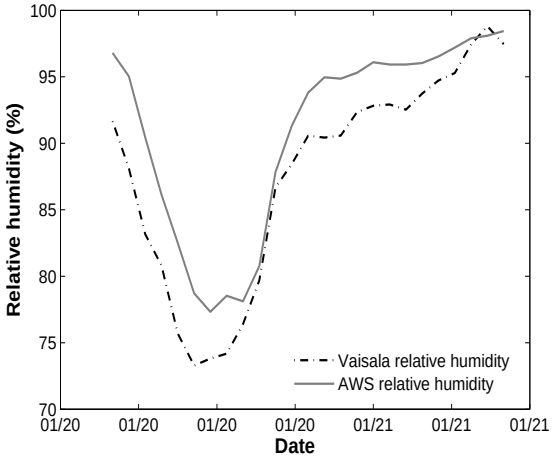

(C) Variation - relative humidity

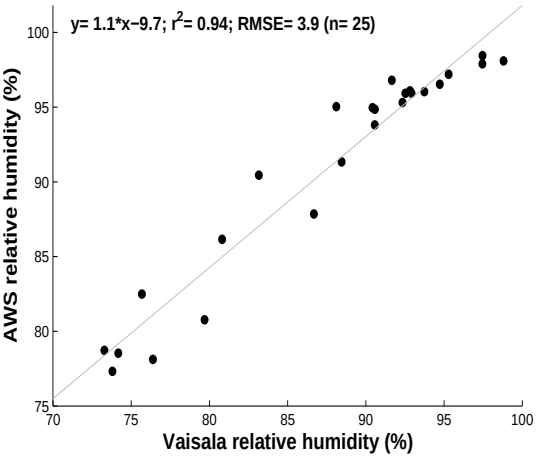

(D) Correlation - relative humidity

FIGURE A.1: Calibration of upper sensor - urban site (January)

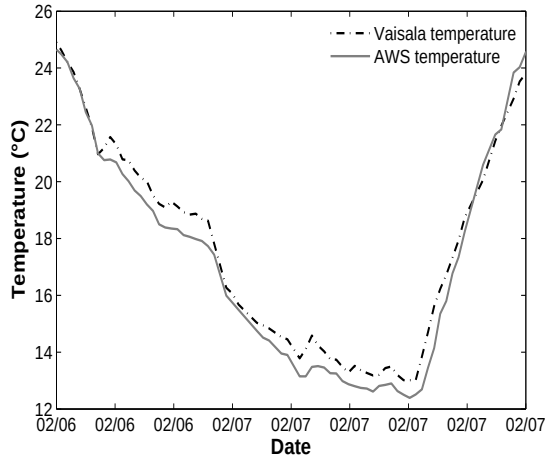

(A) Variation - temperature

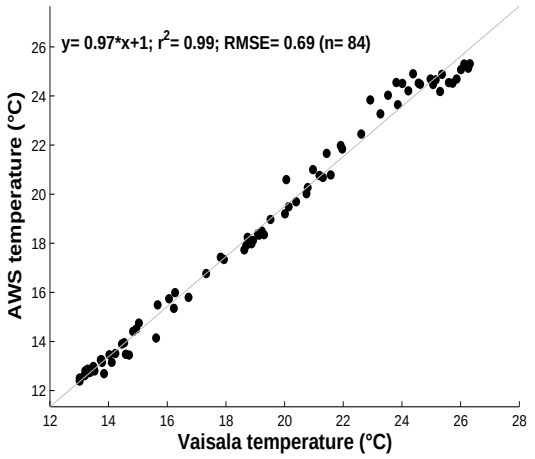

(B) Correlation - temperature

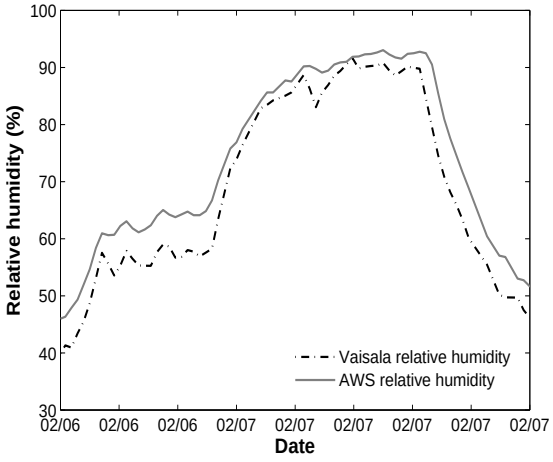

(C) Variation - relative humidity

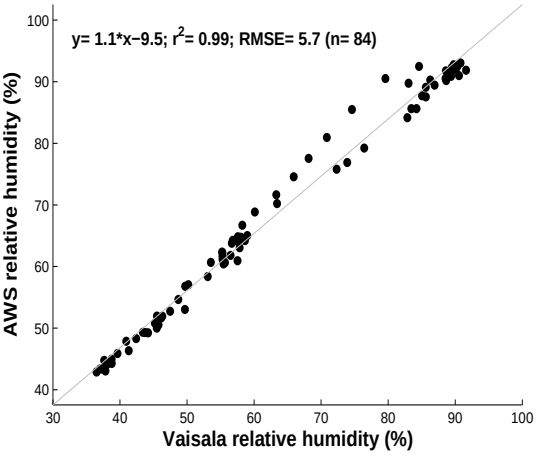

(D) Correlation - relative humidity

FIGURE A.2: Calibration of upper sensor - urban site (February)

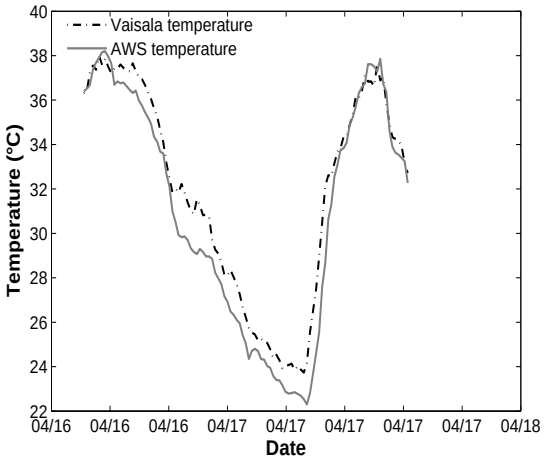

(A) Variation - temperature

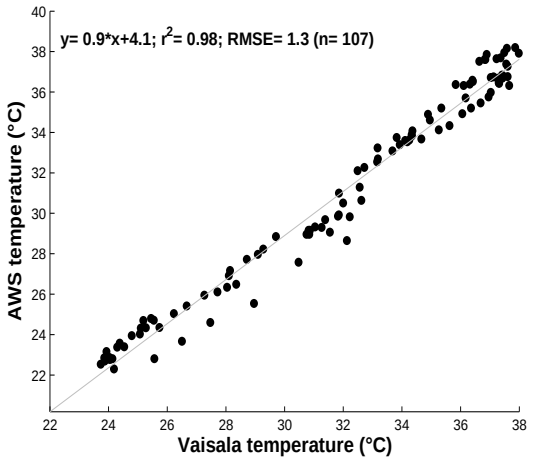

(B) Correlation - temperature

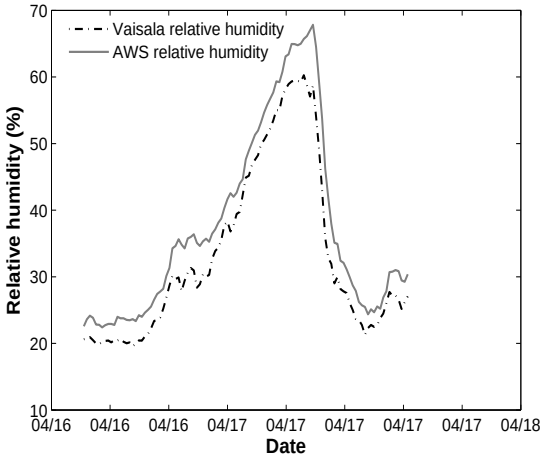

(C) Variation - relative humidity

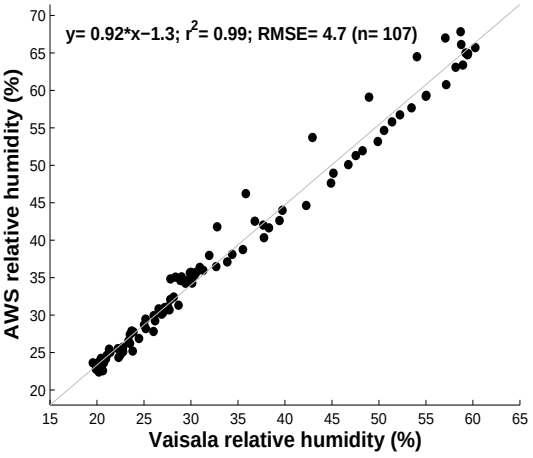

(D) Correlation - relative humidity

FIGURE A.3: Calibration of upper sensor - urban site (April)

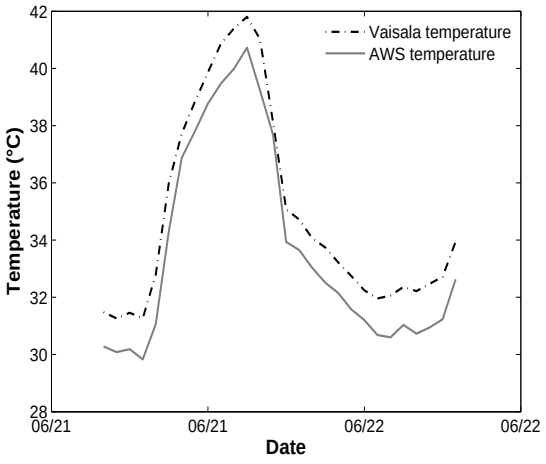

(A) Variation - temperature

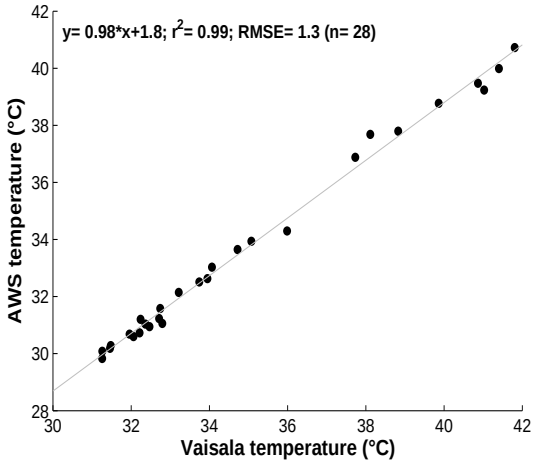

(B) Correlation - temperature

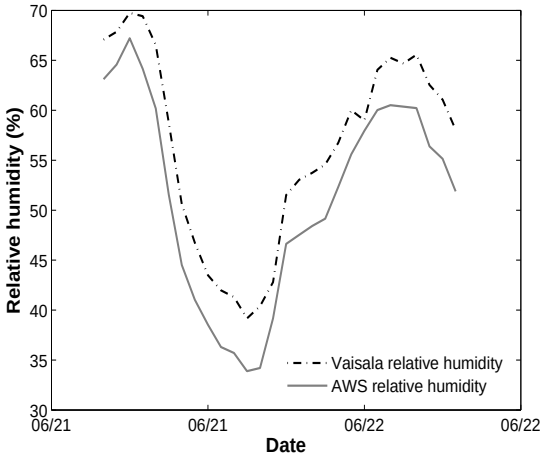

(C) Variation - relative humidity

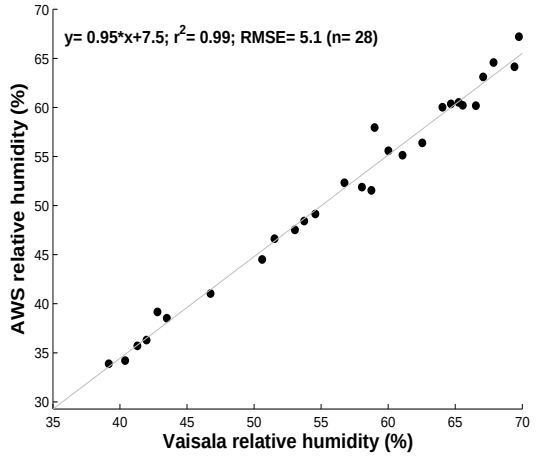

(D) Correlation - relative humidity

FIGURE A.4: Calibration of upper sensor - urban site (June)

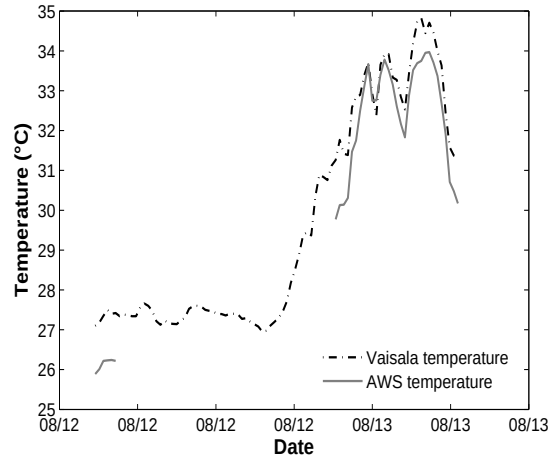

(A) Variation - temperature

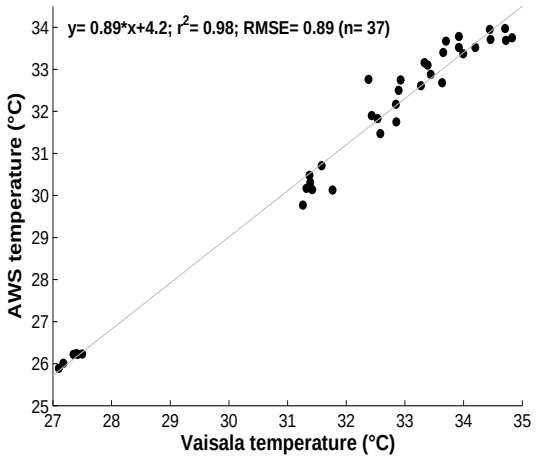

(B) Correlation - temperature

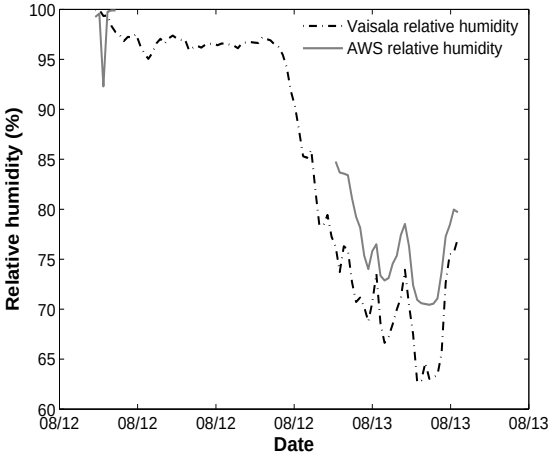

(C) Variation - relative humidity

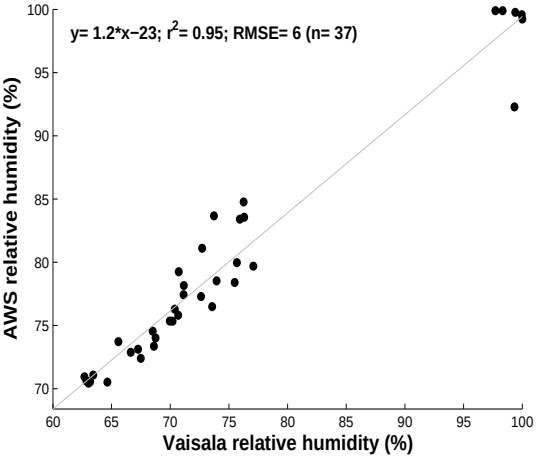

(D) Correlation - relative humidity

FIGURE A.5: Calibration of upper sensor - urban site (August)

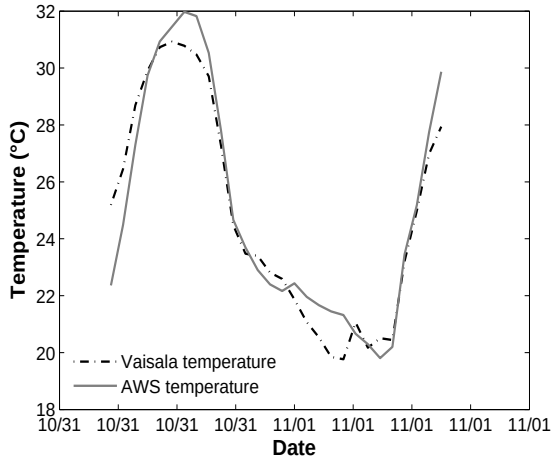

(A) Variation - temperature

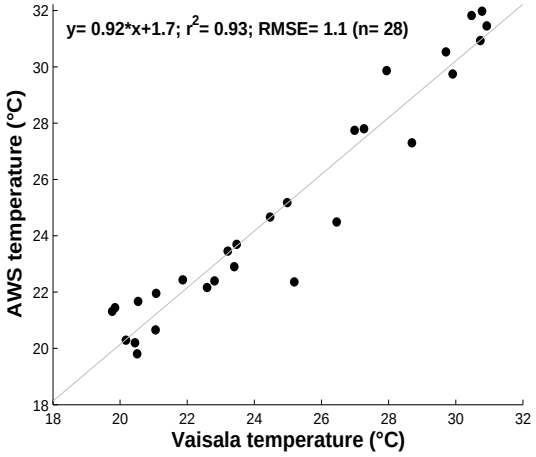

(B) Correlation - temperature

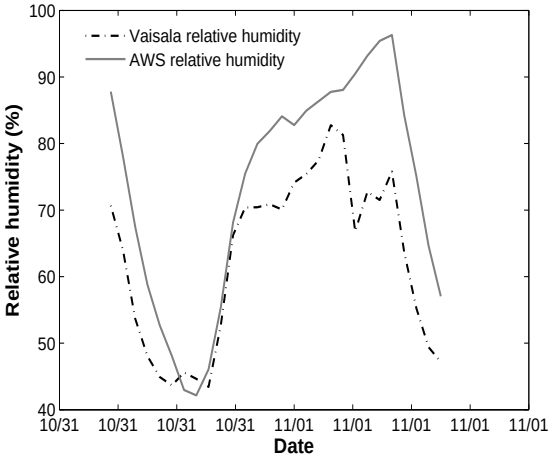

(C) Variation - relative humidity

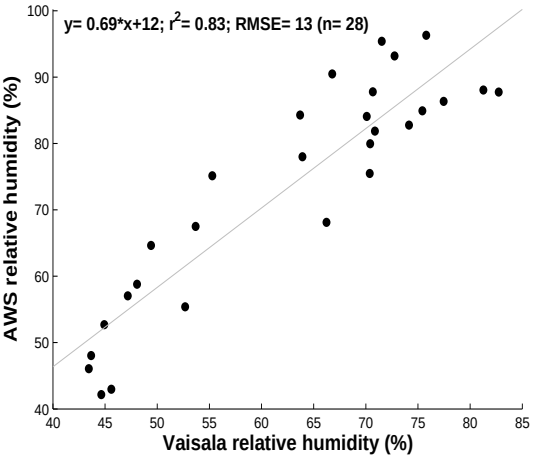

(D) Correlation - relative humidity

FIGURE A.6: Calibration of upper sensor - urban site (October)

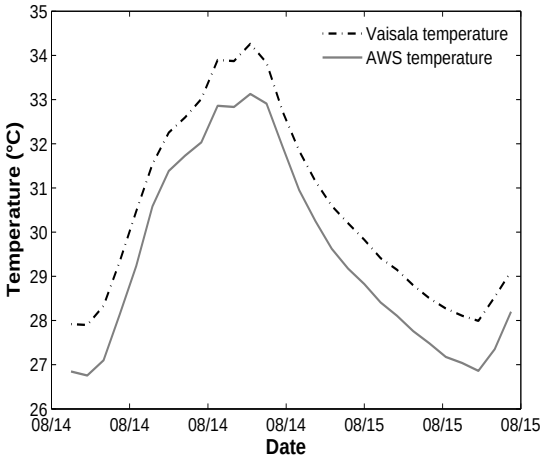

(A) Variation - temperature

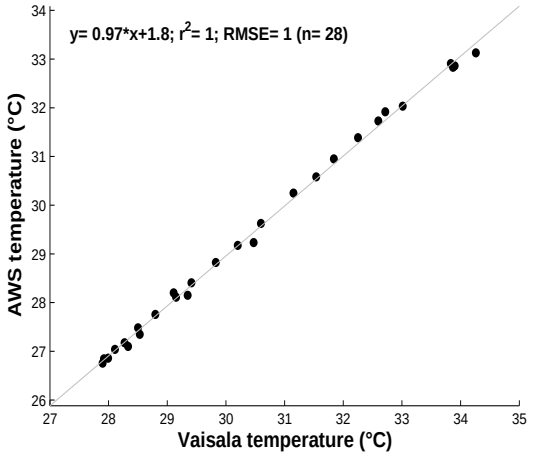

(B) Correlation - temperature

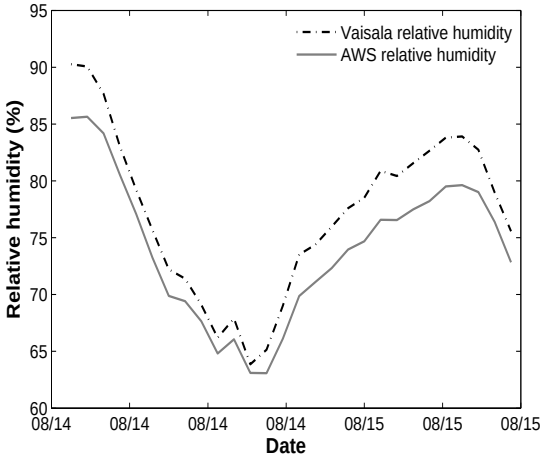

(C) Variation - relative humidity

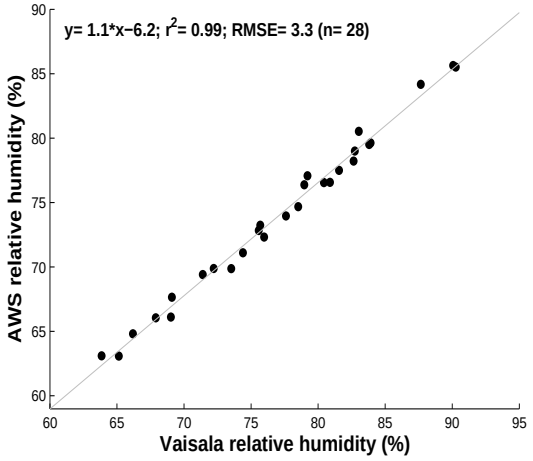

(D) Correlation - relative humidity

FIGURE A.7: Calibration of lower sensor - rural site (August)

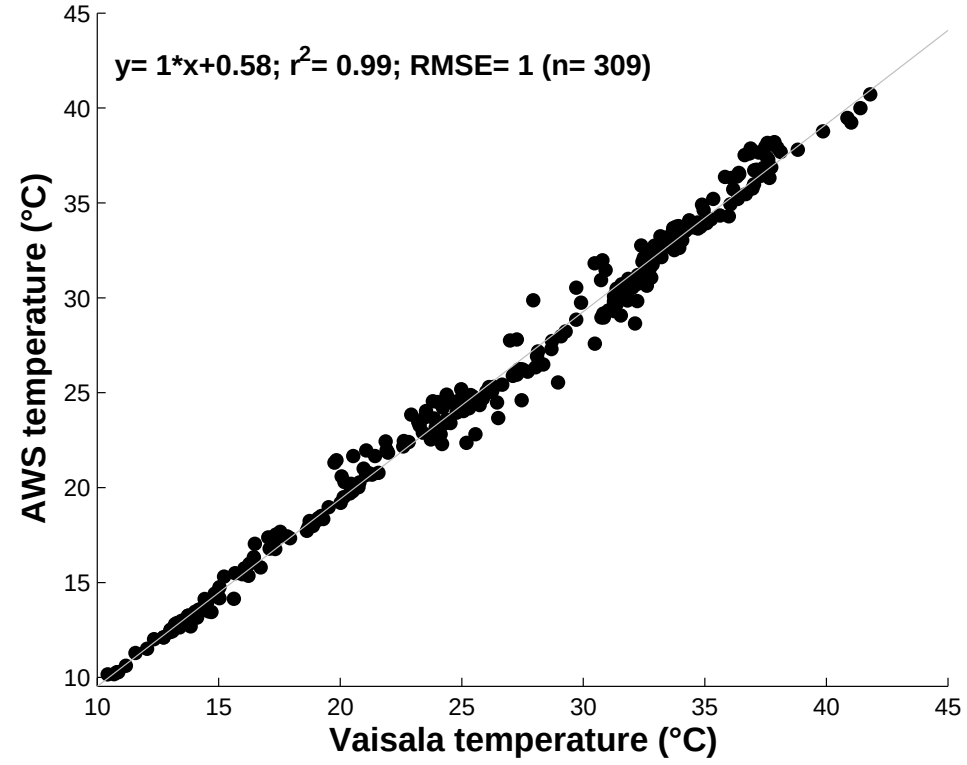

(A) Temperature

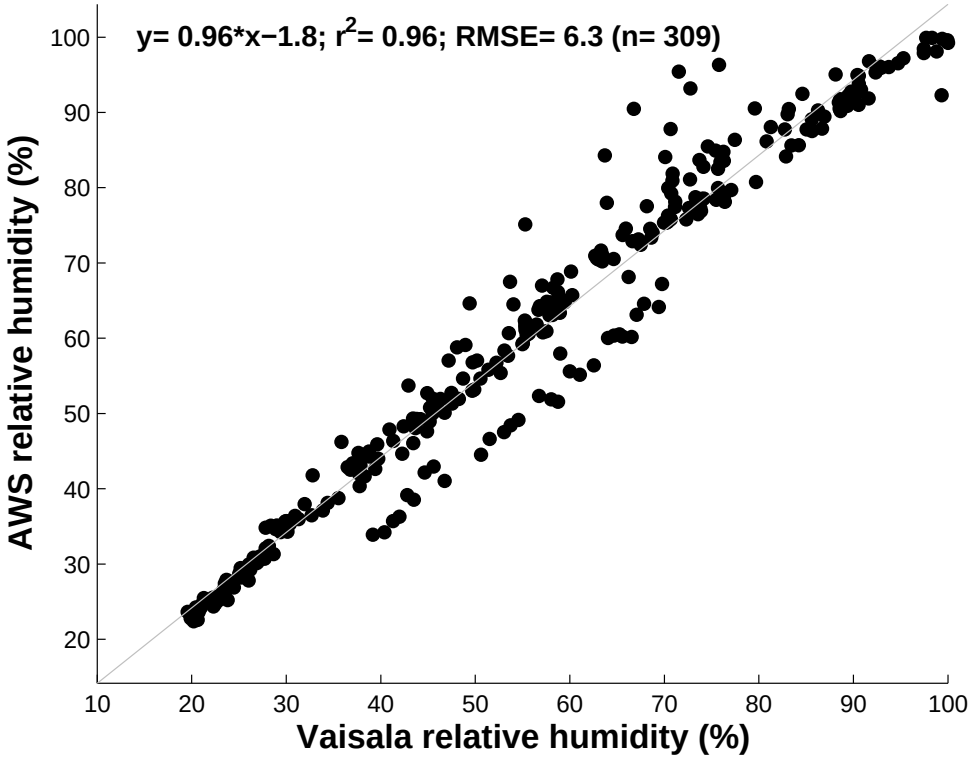

(B) Relative humidity

FIGURE A.8: Overall calibration of upper sensor - urban site

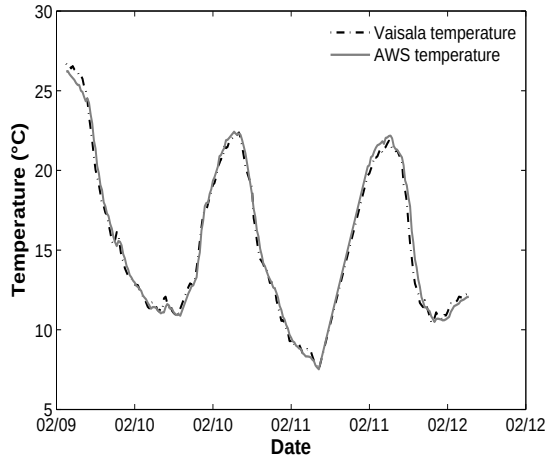

(A) Variation - temperature

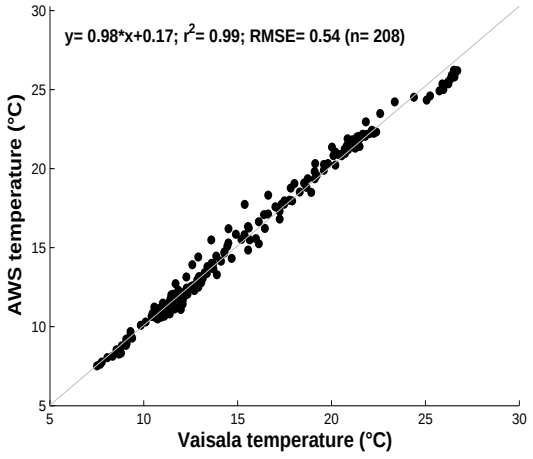

(B) Correlation - temperature

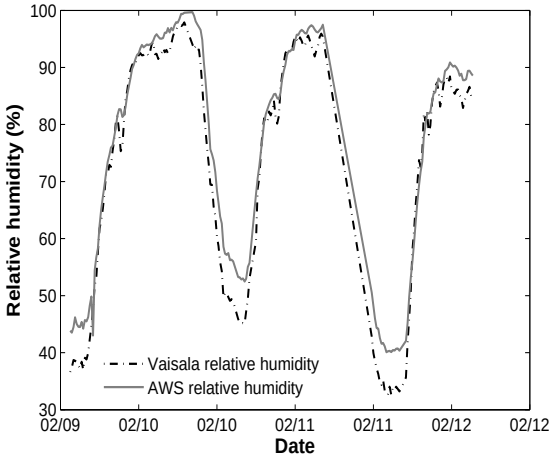

(C) Variation - relative humidity

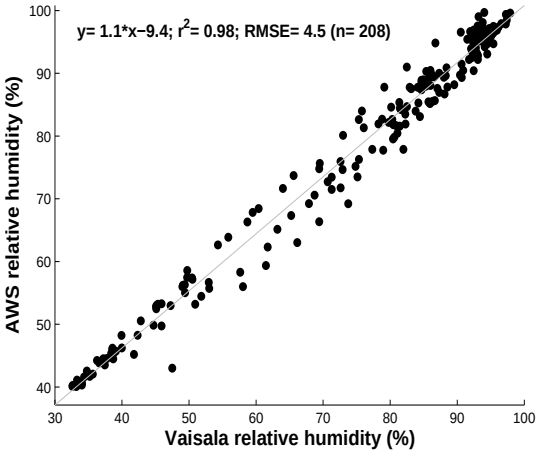

(D) Correlation - relative humidity

FIGURE A.9: Calibration of upper sensor - rural site (February)

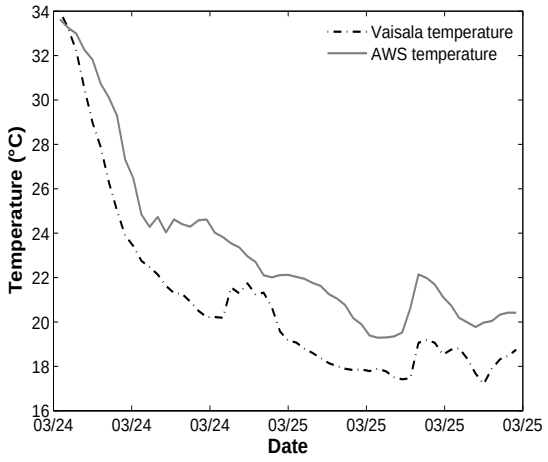

(A) Variation - temperature

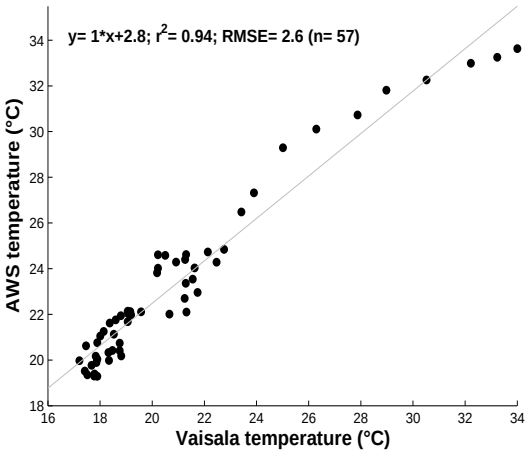

(B) Correlation - temperature

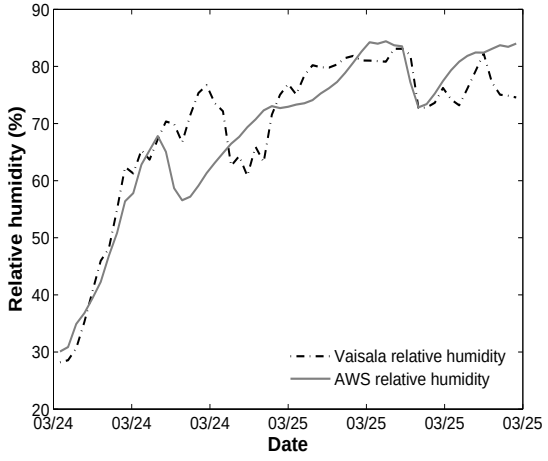

(C) Variation - relative humidity

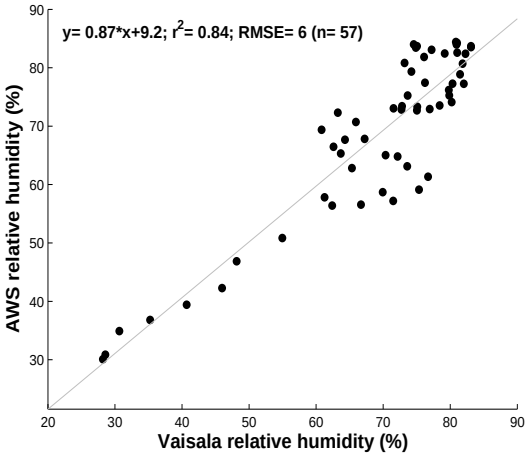

(D) Correlation - relative humidity

FIGURE A.10: Calibration of upper sensor - rural site (March)

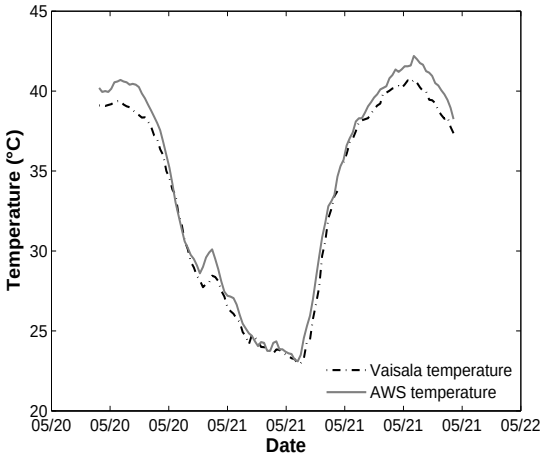

(A) Variation - temperature

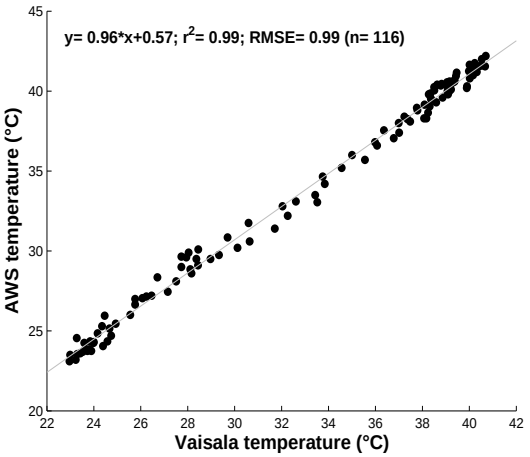

(B) Correlation - temperature

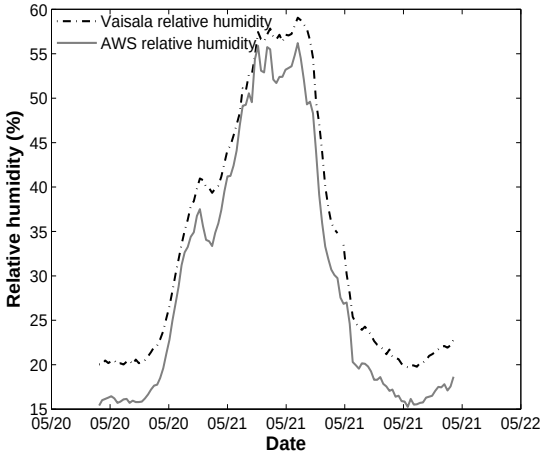

(C) Variation - relative humidity

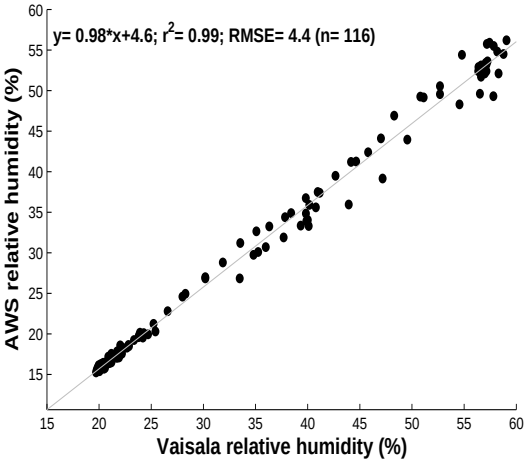

(D) Correlation - relative humidity

FIGURE A.11: Calibration of upper sensor - rural site (May)

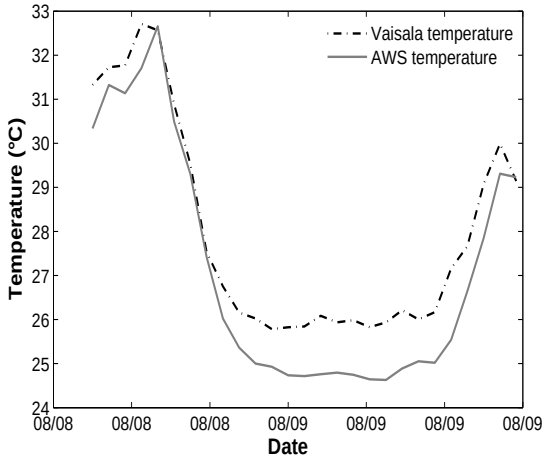

(A) Variation - temperature

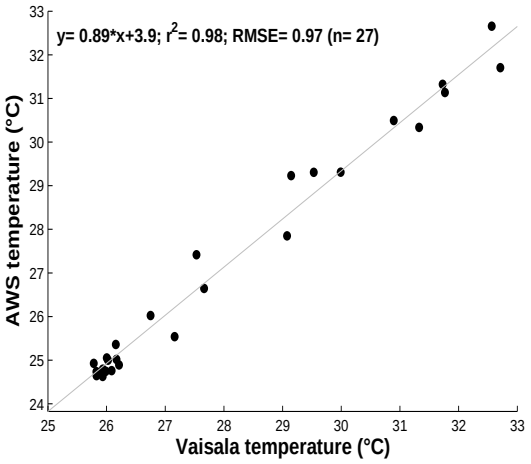

(B) Correlation - temperature

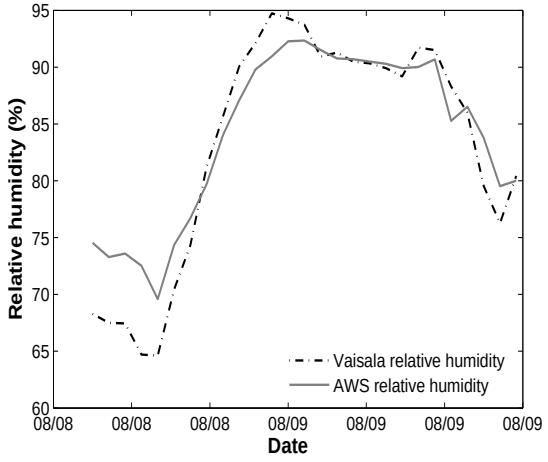

(C) Variation - relative humidity

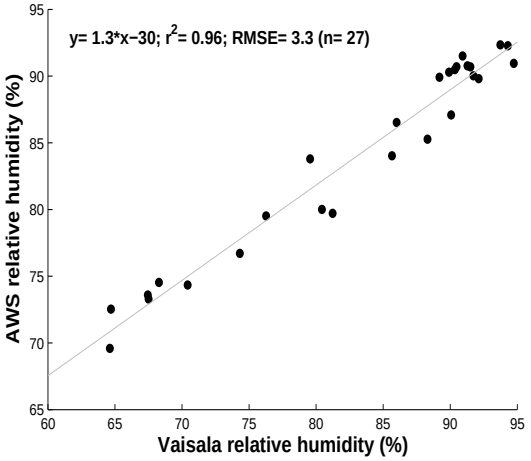

(D) Correlation - relative humidity

FIGURE A.12: Calibration of upper sensor - rural site (August)

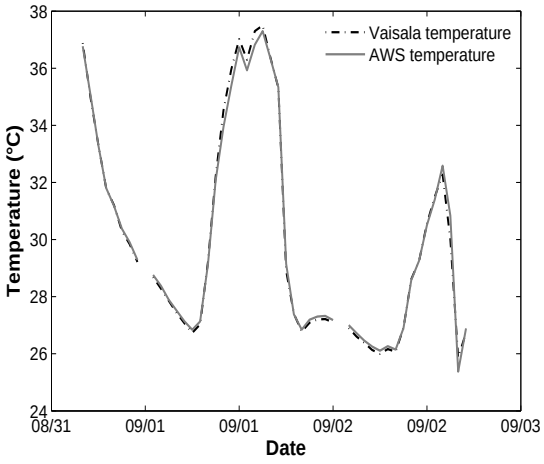

(A) Variation - temperature

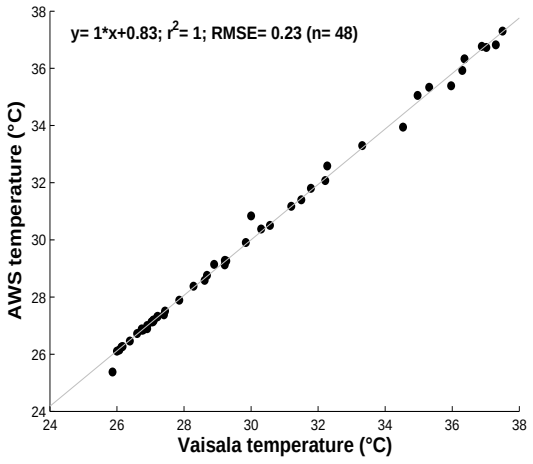

(B) Correlation - temperature

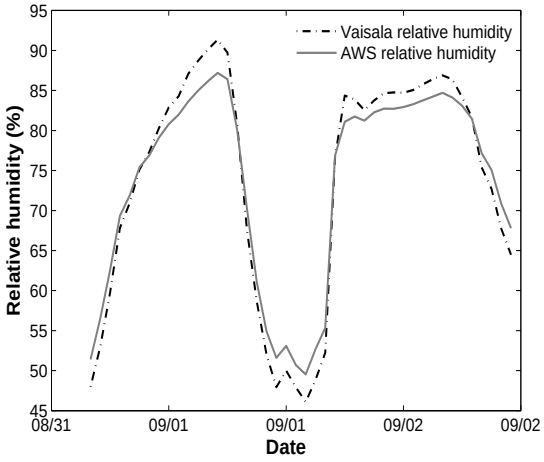

(C) Variation - relative humidity

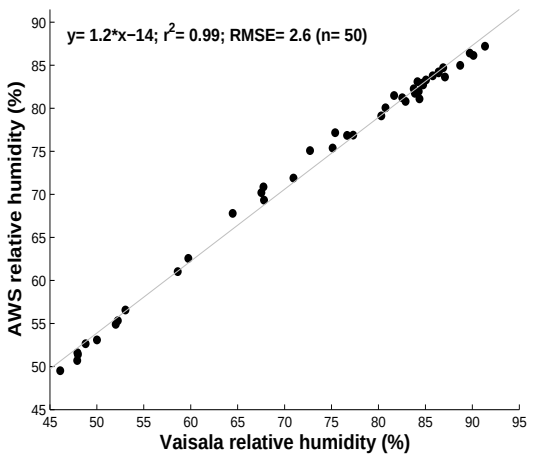

(D) Correlation - relative humidity

FIGURE A.13: Calibration of lower sensor - rural site (August)

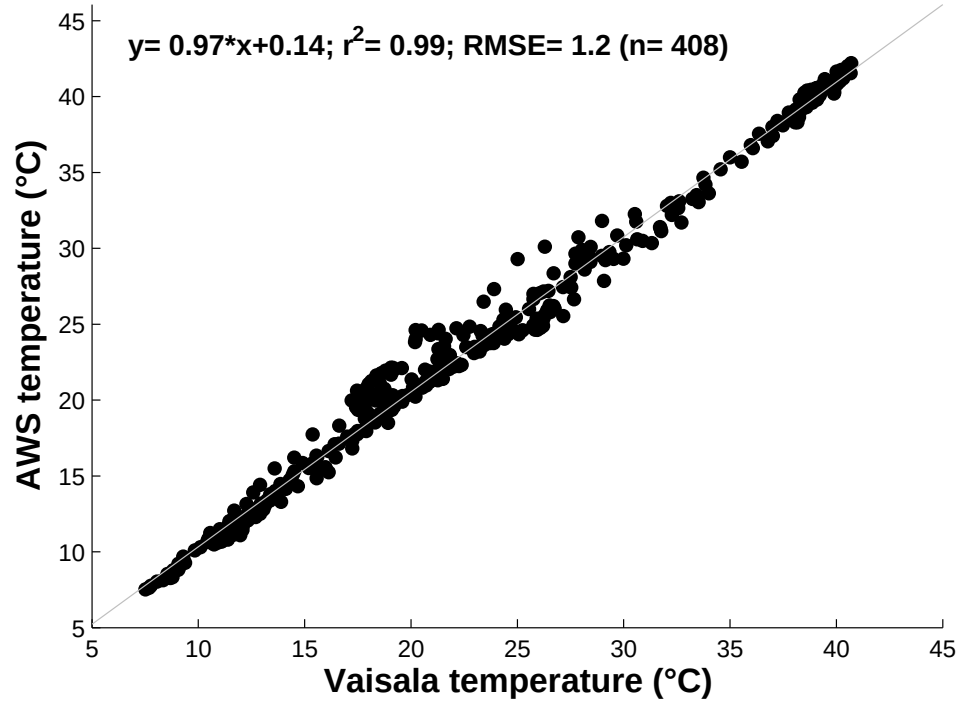

(A) Temperature

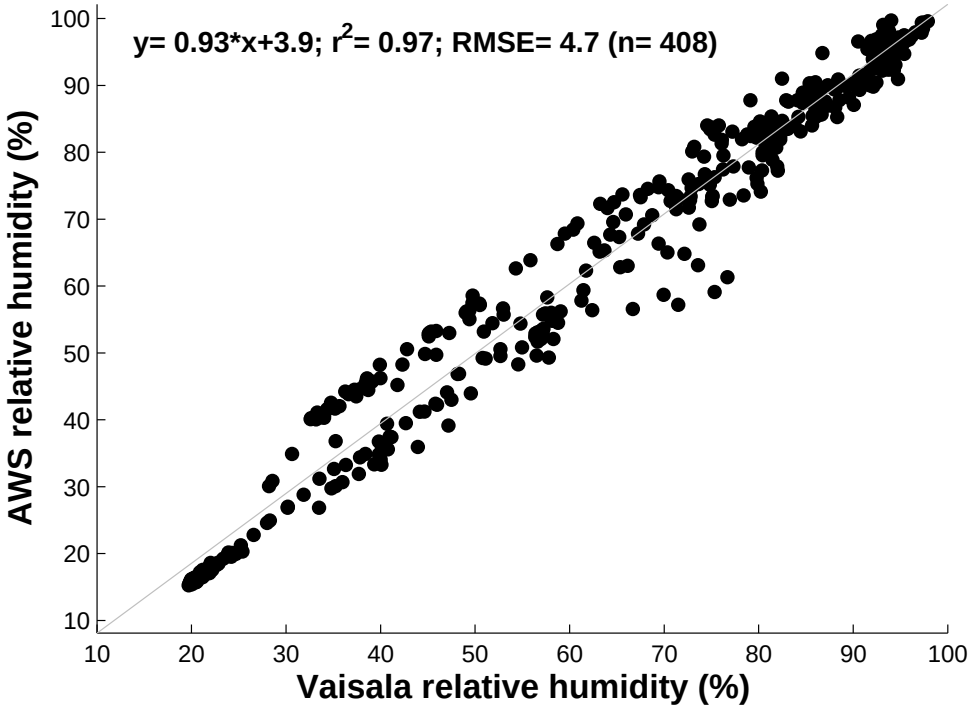

(B) Relative humidity

FIGURE A.14: Overall calibration of upper sensor - rural site

Appendix B

Mobile campaign routes

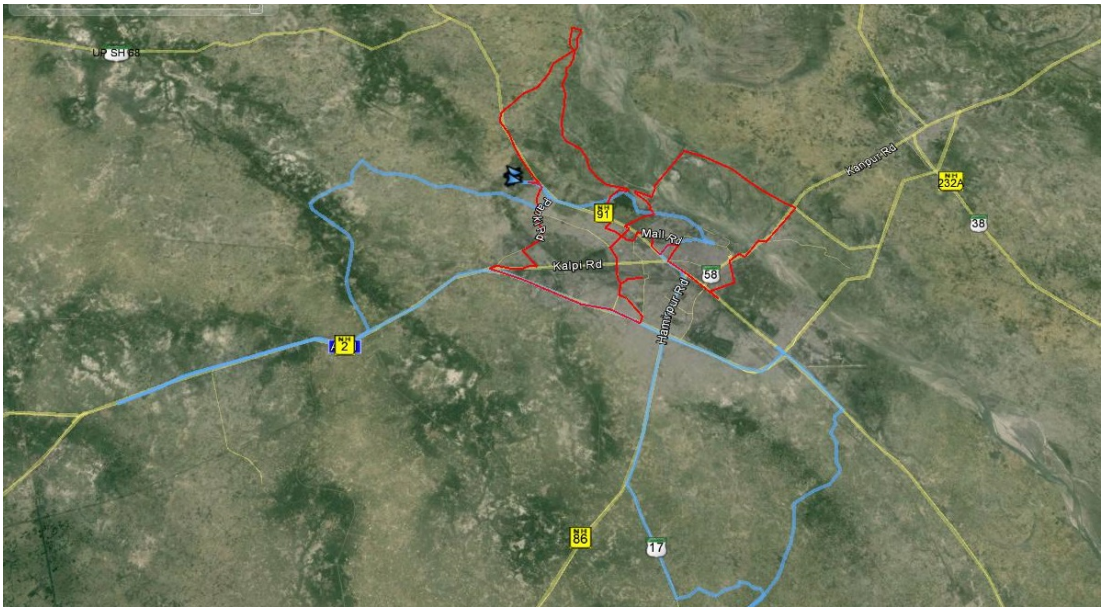

FIGURE B.1: Route of 1st mobile campaign (23rd May, 2014)

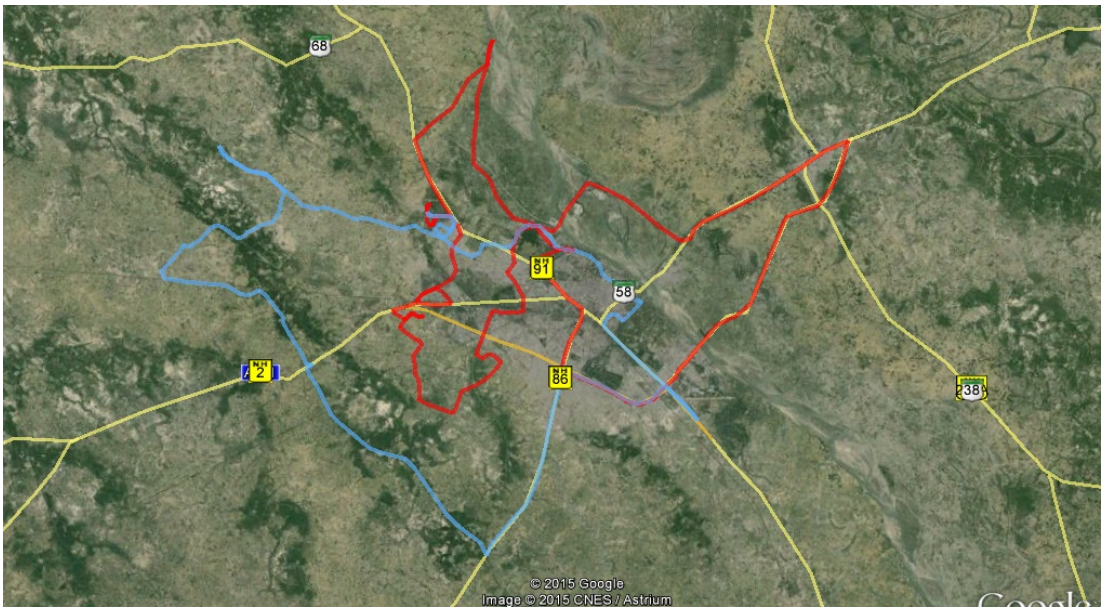

FIGURE B.2: Route of 2nd mobile campaign (6th June, 2014)

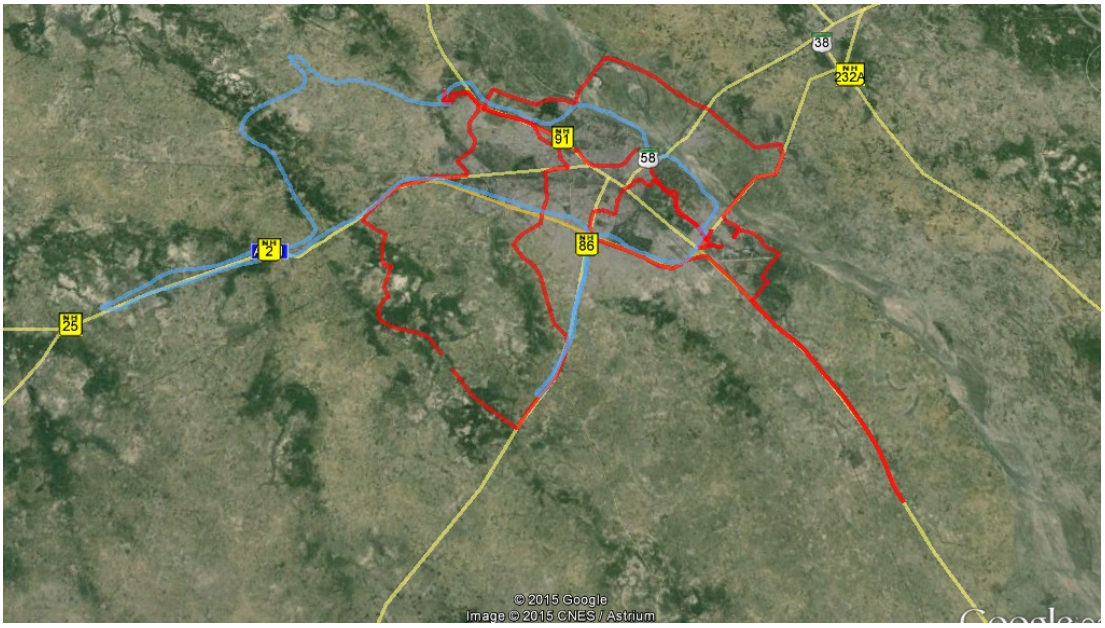

FIGURE B.3: Route of 3rd mobile campaign (5th September, 2014)

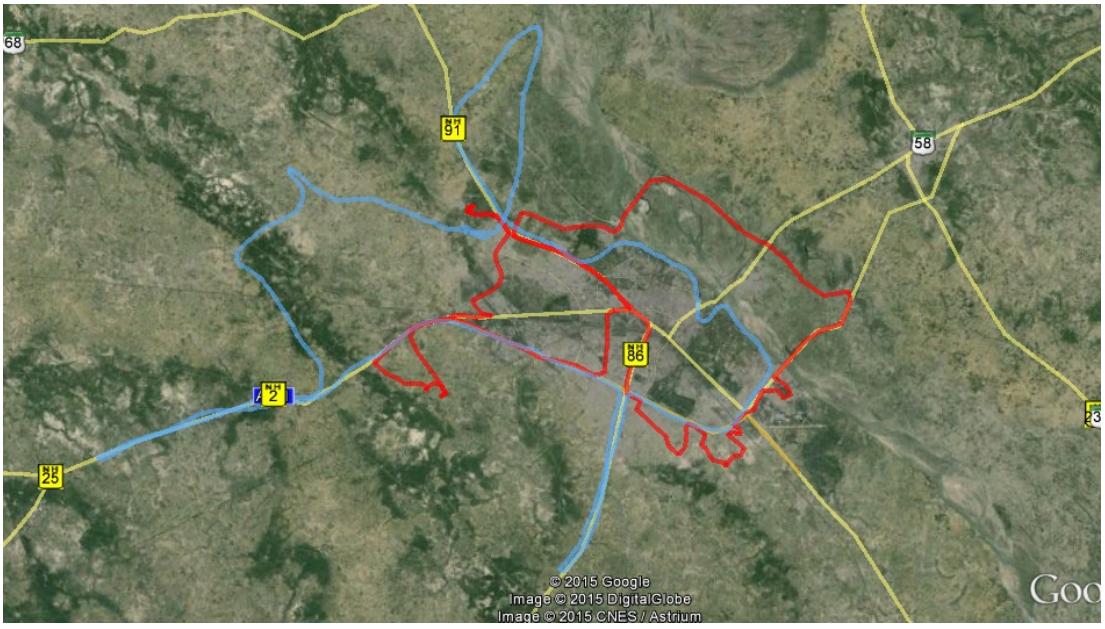

FIGURE B.4: Route of 4th mobile campaign (28th January, 2015)

Appendix C

Vaisala comparison and correction

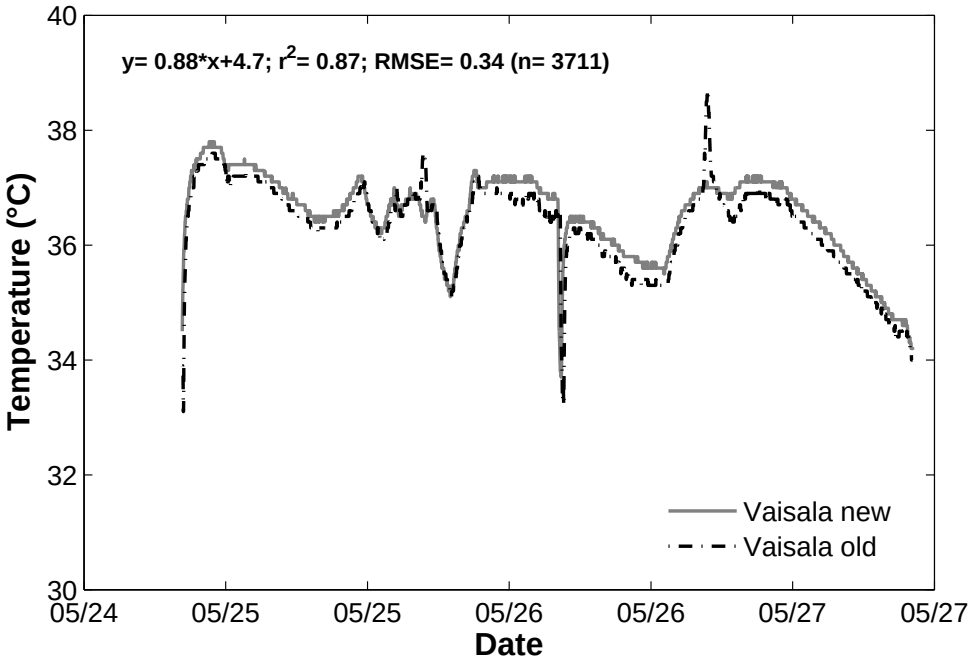

(A) For temperature

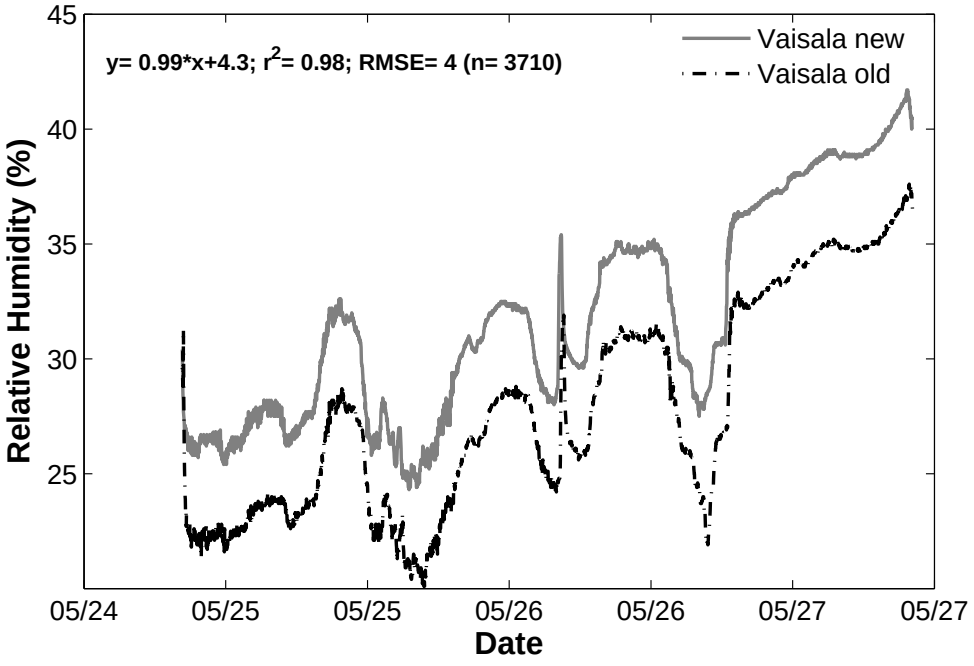

(B) For humidity

FIGURE C.1: Correlation between two Vaisalas

Appendix D

NOAH model specifications and parameterization

TABLE D.1: General parameters in NOAH

Parameter name	Parameter description
$SLOPEDATA$	Linear reservoir coefficient
$SBETADATA$	Parameter used to calculate vegetation effect on soil heat
$FXEXPDATA$	Soil evaporation exponent used in Direct evapotranspiration calculation
$CSOILDATA$	Soil heat capacity
$SALPDATA$	Shape parameter for snow cover
$REFDKDATA$	1st parameter in the surface runoff parameterization
$REFKDTDATA$	2nd parameter in the surface runoff parameterization
$FRZKDATA$	Frozen ground parameter
$ZBOTDATA$	Depth of lower boundary soil temperature
$CZILDATA$	Parameter used in the calculation of the roughness length for heat
$SMLOWDATA$	Soil moisture wilt, soil moisture reference parameter 1
$SMHIGHDATA$	Soil moisture wilt, soil moisture reference parameter 2
Reference	[1]

Table D.2: Soil parameters in NOAH

Parameter name	Parameter description
BB	B parameter
DRYSMC	Dry soil moisture threshold at which direct evaporation from top soil layer ends
F11	Soil thermal diffusivity/conductivity coefficient
MAXSMC	Saturation soil moisture content
REFSMC	Field capacity of soil
SATPSI	Saturation soil matric potential
SATDK	Saturation soil conductivity
SATDW	Saturation soil diffusivity
WLTSMC	Wilting point of soil
QTZ	Soil quartz fraction
Reference	[1]

Table D.3: Vegetation parameters in NOAH

Parameter name	Parameter description
SHDFAC	Green vegetation fraction
NROOT	Rooting depth
RS	Stomatal resistance
RGL	Parameter used in radiation stress function
HS	Parameter used in vapor pressure deficit function
SNUP	Threshold water-equivalent snow depth that implies 100% snow cover
MAXALB	Upper bound on maximum albedo over deep snow
LAIMIN	Minimum leaf area index through the year
LAIMAX	Maximum leaf area index through the year
EMISSMIN	Minimum background emissivity through the year
EMISSMAX	Maximum background emissivity through the year
ALBEDOMIN	Minimum background albedo through the year
ALBEDOMAX	Maximum background albedo through the year
Z0MIN	Minimum background roughness length through the year
Z0MAX	Maximum background roughness length through the year
TOPTDATA	Optimum transpiration air temperature
CMCMAXDATA	Maximum canopy water capacity
CFACTRDATA	Parameter used in the canopy interception calculation
RSMAXDATA	Maximal stomatal resistance
BARE	The land-use category representing bare ground
NATURAL	The land-use category representative of the non-urban portion of urban land-use points
Reference	[1]

TABLE D.4: Soil types in NOAH

USGS and USGS-RUC soil types
Sand
Loamy sand
Sandy loam
Silt loam
Silt
Loam
Sandy clay loam
Silty clay loam
Clay loam
Sandy clay
Silty clay
Clay Organic material
Water
Bedrock
Other(land-ice)
Playa
Lava
White sand
Reference [1]

Table D.5: Vegetation types in NOAH

STAS and STAS-RUC soil types	MODIFIED_IGBP_MODIS_NOAH soil types
Urban and Built-Up Land	Evergreen Needleleaf Forest
Dryland Cropland and Pasture	Evergreen Broadleaf Forest
Irrigated Cropland and Pasture	Deciduous Needleleaf Forest
Mixed Dryland/Irrigated Cropland	Deciduous Broadleaf Forest
Cropland/Grassland Mosaic	Mixed Forests
Cropland/Woodland Mosaic	Closed Shrublands
Grassland	Open Shrublands
Shrubland	Woody Savannas
Mixed Shrubland/Grassland	Savannas
Savanna	Grasslands
Deciduous Broadleaf Forest	Permanent wetlands
Deciduous Needleleaf Forest	Croplands
Evergreen Broadleaf Forest	Urban and Built-Up
Evergreen Needleleaf Forest	Cropland/natural vegetation mosaic
Mixed Forest	Snow and Ice
Water Bodies	Barren or Sparsely Vegetated
Herbaceous Wetland	Water
Wooded Wetland	Wooded Tundra
Barren or Sparsely Vegetated	Mixed Tundra
Herbaceous Tundra	Barren Tundra
Wooded Tundra	
Mixed Tundra	
Bare Ground Tundra	
Snow or Ice	
Playa	
Lava	
White Sand	
Reference	[1]

Table D.6: Parameters used in model run - urban

Parameter name	Parameter used	Justification
Vegetation parameter	Urban and Built-Up Land	Surrounding land use class
Soil parameter	Silty clay	Previous hydrometer analysis in the region
Slope type	1	Flat plain
Deep soil temperature	295 K	Mean annual air temperature
Air temperature level	1.5m	Instrument height
Wind level	2m	Instrument height
Urban vegetation category	2	To prevent use of urban canopy

Table D.7: Parameters used in model run - rural

Parameter name	Paremeter used	Justification
Vegetation parameter	Irrigated Cropland and Pasture	Surrounding land use class
Soil parameter	Silty clay	Previous hydrometer analysis in the region
Slope type	1	Flat plain
Deep soil temperature	293 K	Mean annual air temperature
Air temperature level	1.5m	Instrument height
Wind level	2m	Instrument height
Urban vegetation category	1	Default

Appendix E

Interpolation of missing radiation data for rural site

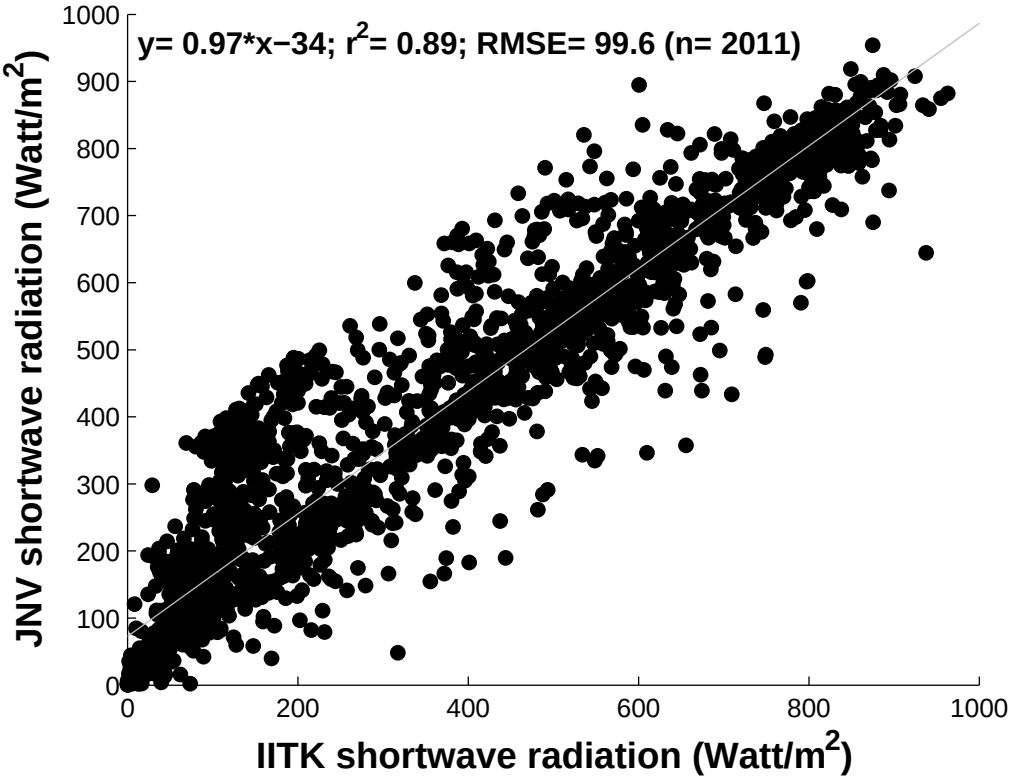

(A) Shortwave radiation

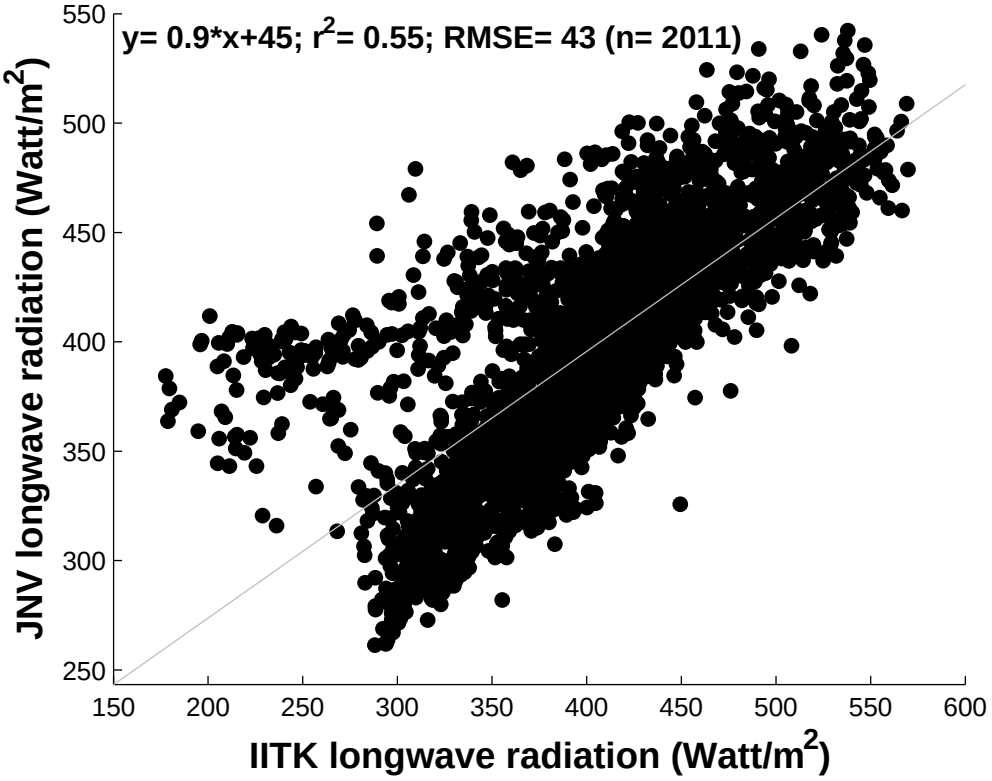

(B) Longwave radiation

FIGURE E.1: Correlation of radiation components during two for rural data interpolation

Appendix F

Specifications of instruments used in the study

Table F.1: Temperature sensor specification

iTMS 101 [6]	
Sensor Type	Band gap
Measurement Range	-40°C to +120°C
Resolution	0.01°C
Accuracy	± 0.2 °C (with radiation shield)
Repeatability	± 0.1°C
Response Time	1 sec
Power Supply	3.3 V, 0.55 mA, 0.3 μA Standby
Power consumption	$80\mu W$
Long term drift	< 0.04°C/yr

Table F.2: Relative humidity sensor specification

iHMS101 [6]	
Sensor Type	Solid State thin film capacitive Sensor
Measurement Range	0 to 100 %RH
Resolution	0.03 %RH
Accuracy	±3.0 %RH or better
Repeatability	± 0.1%RH
Hysteresis	± 0.1° %RH
Output Format	< 1 % RH
Response Time	1 sec
Power Supply	3.3 V, 0.55 mA, 0.3 μA Standby
Power Consumption	80 μW
Long term drift	<0.5 %RH/yr

Table F.3: Anemometer specification

iWMS1013 [6]	
Sensor Type	Optically scanned cup anemometer
Range	0 to 60 m/sec
Resolution	0.1 m/s
Accuracy	± 0.5 m/s
Threshold	1.3 m/sec
Response Time	immediate
Survival Range	80 m/s

Table F.4: Wind direction sensor specification

iWMS1021 [6]	
Sensor Type	Propeller Vane
Range	0 to 359 °
Resolution	1 °
Accuracy	± 5 °
Threshold	0.5 m/s
Response Time	immediate
Survival Range	80 m/s

Table F.5: Rain guage specification

iRMS101 [6]	
Sensor Type	Tipping bucket rain gauge or suitable
Range	0.5 mm to 900 mm or 450 mm (per hour)
Resolution	0.2mm - 0.25 mm
Accuracy	± 3% up to 300-350 mm/ hr intensity; ± 5% for higher range

Table F.6: Soil moisture sensor specification

WaterScout SM 100 [3]	
Sensor type	Capacitance
Range	0% VWC to saturation
Resolution	0.1% VWC
Accuracy	3% VWC
Sensing Area	2.4 in (6 cm) x 0.8 in (2 cm)
Power Requirements	3 to 5V @ 6 to 10 mA

Table F.7: Soil temperature sensor specification

Watchdog 3667 [4]	
Range	-30 °C to 100 °C
Power Requirements	3 to 5V @ 6 to 10 mA
Accuracy	±1 °C

Table F.8: Net radiometer specification

CNR4 [2]	
Sensor type	Thermophile
Bubble level sensitivity	$< 0.5°$
Operating temperature	-40°C to +80°C
Spectral range for pyranometer	300 nm - 2800 nm
Spectral range for pyrgeometer	4.5 μm to 42 μm

Table F.9: Vaisala HMT330 specification

Vaisala HMT330 [5]	
Temperature measurement accuracy	±0.2 °C
Relative humidity meausrement accuracy	±1.0%RH
Relative humidity range	0% to 100% RH
Power consumption	Maximum of 20mA
Logging interval	10 sec

Bibliography

[1] NOAH LSM specifications and resources. http://www.ral.ucar.edu/research/land/technology/lsm.php. Accessed: 2015-05-02.

[2] Radiometer specifications. http://www.kippzonen.com/Product/85/CNR-4-Net-Radiometer#.VUXGgfkirIU. Accessed: 2015-05-02.

[3] Soil moisture sensor specifications. http://www.specmeters.com/weather-monitoring/sensors-and-accessories/sensors/soil-moisture-sensors/sm100/. Accessed: 2015-05-02.

[4] Soil temperature sensor specifications. http://www.specmeters.com/assets/1/22/3667ExtTmp.pdf. Accessed: 2015-05-02.

[5] Vaisala HMT 330 sensor specifications. http://www.vaisala.com/Vaisala%20Documents/Brochures%20and%20Datasheets/HMT330-Datasheet-B210951EN-H.pdf. Accessed: 2015-05-02.

[6] AWS brochure. https://www.google.com/url?sa=t&rct=j&q=&esrc=s&source=web&cd=1&cad=rja&uact=8&ved=0CB4QFjAA&url=http%3A%2F%2Fwww.weather-risk.com%2FWeatherSensor%2FSensorPdf%2FIngenAWS%2520Brochure%2520V6.01_1.pdf&ei=GsVFVcbBJ8G4uAT-_YDgCA&usg=AFQjCNFvrGM3SQ5rLplwbuypi2Ucm_6QpQ&sig2=attR6e6NUqdS5iEO5yHObg, 2014.

[7] Ansar, S., Dhanya, C., Thomas, G., Chandran, A., John, L., Prasanthi, S., Vishnu, R., and Zachariah, E. A study of urban/rural cooling rates in thiruvananthapuram, kerala. *J. Ind. Geophys. Union (January 2012) 16*, 1 (2012), 29–36.

[8] Arnfield, A. J. Micro-and mesoclimatology. *Progress in physical geography 22*, 4 (1998), 103–113,533–544.

[9] Arnfield, A. J. Micro-and mesoclimatology. *Progress in Physical Geography 24*, 2 (2000), 261–271.

[10] Arnfield, A. J. Micro-and mesoclimatology. *Progress in physical geography 25*, 1 (2001), 123–133,560–569.

[11] Arnfield, A. J. Two decades of urban climate research: a review of turbulence, exchanges of energy and water, and the urban heat island. *International journal of climatology 23*, 1 (2003), 1–26.

[12] Badarinath, K., Chand, T. K., Madhavilatha, K., and Raghavaswamy, V. Studies on urban heat islands using envisat aatsr data. *Journal of the Indian Society of Remote Sensing 33*, 4 (2005), 495–501.

[13] Bahl, H., and Padmanabhamurty, B. Heat island studies at delhi. *Mausam 30* (1979), 119–122.

[14] Barlow, J. F. Progress in observing and modelling the urban boundary layer. *Urban Climate 10* (2014), 216–240.

[15] Bhattacharya, A., and Mandal, M. Evaluation of noah land-surface models in predicting soil temperature and moisture at two tropical sites in india. *Meteorological Applications* (2014).

[16] Bonan, G. Ecological climatology: Principles and applications, 2008.

[17] Borbora, J., and Das, A. K. Summertime urban heat island study for guwahati city, india. *Sustainable Cities and Society 11* (2014), 61–66.

[18] Bornstein, R. D. Observations of the urban heat island effect in new york city. *Journal of Applied Meteorology 7*, 4 (1968), 575–582.

[19] Brazel, A. J., Arnfield, J. A., Greenland, D. E., and Willmott, C. J. Physical and boundary-layer climatology. *Physical Geography 12*, 3 (1991), 189–206.

[20] Carrico, C. M., Bergin, M. H., Xu, J., Baumann, K., and Maring, H. Urban aerosol radiative properties: Measurements during the 1999 atlanta supersite experiment. *Journal of Geophysical Research: Atmospheres (1984–2012) 108*, D7 (2003).

[21] Cermak, J. E. *Wind climate in cities*, vol. 277. Springer Science & Business Media, 1995.

[22] Chakraborty, S. D., Kant, Y., and Mitra, D. Assessment of land surface temperature and heat fluxes over delhi using remote sensing data. *Journal of environmental management 148* (2015), 143–152.

[23] Chand, T. K., Latha, K. M., and Badarinath, K. Studies on urban heat islands using envisat aatsr data.

[24] Chang, C. H., and Goh, K. C. The relationship between height to width ratios and the heat island intensity at 22: 00 h for singapore.

[25] Changnon, S. A. Inadvertent weather modification in urban areas: Lessons for global climate change. *Bulletin of the American Meteorological Society 73*, 5 (1992), 619–627.

[26] Chen, F., Janjić, Z., and Mitchell, K. Impact of atmospheric surface-layer parameterizations in the new land-surface scheme of the ncep mesoscale eta model. *Boundary-Layer Meteorology 85*, 3 (1997), 391–421.

[27] Chen, F., Mitchell, K., Schaake, J., Xue, Y., Pan, H.-L., Koren, V., Duan, Q. Y., Ek, M., and Betts, A. Modeling of land surface evaporation by four schemes and comparison with fife observations. *Journal of Geophysical Research: Atmospheres (1984–2012) 101*, D3 (1996), 7251–7268.

[28] Crutzen, P. J. New directions: the growing urban heat and pollution "island" effect—impact on chemistry and climate. *Atmospheric environment 38*, 21 (2004), 3539–3540.

[29] Deosthali, V. Impact of rapid urban growth on heat and moisture islands in pune city, india. *Atmospheric Environment 34*, 17 (2000), 2745–2754.

[30] Devadas, M. D., and Lilly Rose, A. Urban factors and the intensity of heat island in the city of chennai. In *Proceedings of the seventh International Conference on Urban Climate* (2009).

[31] Devi, S. S. Urban heat islands and environmental impact. In *86th AMS annual meeting. http://www. scopus. com/inward/record. url* (2006).

[32] Douglas, I. The urban environment.

[33] Ek, M., Mitchell, K., Lin, Y., Rogers, E., Grunmann, P., Koren, V., Gayno, G., and Tarpley, J. Implementation of noah land surface model advances in the national centers for environmental prediction operational mesoscale eta model. *Journal of Geophysical Research: Atmospheres (1984–2012) 108*, D22 (2003).

[34] Fritschen, L. J., and Simpson, J. R. Surface energy and radiation balance systems: General description and improvements. *Journal of Applied Meteorology 28*, 7 (1989), 680–689.

[35] Gago, E., Roldan, J., Pacheco-Torres, R., and Ordóñez, J. The city and urban heat islands: A review of strategies to mitigate adverse effects. *Renewable and Sustainable Energy Reviews 25* (2013), 749–758.

[36] Garratt, J. Sensitivity of climate simulations to land-surface and atmospheric boundary-layer treatments-a review. *Journal of Climate 6*, 3 (1993), 419–448.

[37] Goldreich, Y. Urban climate studies in johannesburg, a sub-tropical city located on a ridge—a review. *Atmospheric Environment. Part B. Urban Atmosphere 26*, 3 (1992), 407–420.

[38] Goldreich, Y. Urban climate studies in israel—a review. *Atmospheric Environment 29*, 4 (1995), 467–478.

[39] Goward, S. N. Thermal behavior of urban landscapes and the urban heat island. *Physical Geography 2*, 1 (1981), 19–33.

[40] Grimmond, C., and Oke, T. R. Aerodynamic properties of urban areas derived from analysis of surface form. *Journal of applied meteorology 38*, 9 (1999), 1262–1292.

[41] Guhathakurta, S., and Gober, P. The impact of the phoenix urban heat island on residential water use. *Journal of the American Planning Association 73*, 3 (2007), 317–329.

[42] Gupta, R. Temporal and spatial variations of urban heat island effect in jaipur city using satellite data. *Environment and Urbanization Asia 3*, 2 (2012), 359–374.

[43] Harlan, S. L., Brazel, A. J., Prashad, L., Stefanov, W. L., and Larsen, L. Neighborhood microclimates and vulnerability to heat stress. *Social Science & Medicine 63*, 11 (2006), 2847–2863.

[44] Hogan, A. W., and Ferrick, M. G. Observations in nonurban heat islands. *Journal of Applied Meteorology 37*, 2 (1998), 232–236.

[45] Howard, L. *The climate of London: deduced from meteorological observations made in the metropolis and at various places around it*, vol. 2. Harvey and Darton, J. and A. Arch, Longman, Hatchard, S. Highley [and] R. Hunter, 1833.

[46] Huang, J., Zhou, C., Lee, X., Bao, Y., Zhao, X., Fung, J., Richter, A., Liu, X., and Zheng, Y. The effects of rapid urbanization on the levels in tropospheric nitrogen dioxide and ozone over east china. *Atmospheric Environment 77* (2013), 558–567.

[47] Huang, L., Li, J., Zhao, D., and Zhu, J. A fieldwork study on the diurnal changes of urban microclimate in four types of ground cover and urban heat island of nanjing, china. *Building and environment 43*, 1 (2008), 7–17.

[48] Indian Meteorological Department. Ever recorded maximum and minimum temperatures up to 2010. `http://www.imdpune.gov.in/Temp_Extremes/histext2010.pdf`, 2015. Accessed: 2015-05-02.

[49] Jacobson, M. Z., and Ten Hoeve, J. E. Effects of urban surfaces and white roofs on global and regional climate. *Journal of climate 25*, 3 (2012), 1028–1044.

[50] Jaregui, E. Tropical urban climates: review and assessment. *Proc. of Technical Con [erence on Urban Climatology and its Applications with Special Regard to Tropical Areas* (1986), 26–45.

[51] Jiang, X., Wiedinmyer, C., Chen, F., Yang, Z.-L., and Lo, J. C.-F. Predicted impacts of climate and land use change on surface ozone in the houston, texas, area. *Journal of Geophysical Research: Atmospheres (1984–2012) 113*, D20 (2008).

[52] Johnson, D. Urban modification of diurnal temperature cycles in birmingham, uk. *Journal of climatology 5*, 2 (1985), 221–225.

[53] Kalnay, E., and Kanamitsu, M. Time schemes for strongly nonlinear damping equations. *Monthly weather review 116*, 10 (1988), 1945–1958.

[54] Kishtawal, C. M., Niyogi, D., Tewari, M., Pielke, R. A., and Shepherd, J. M. Urbanization signature in the observed heavy rainfall climatology over india. *International Journal of Climatology 30*, 13 (2010), 1908–1916.

[55] Klysik, K., and Fortuniak, K. Temporal and spatial characteristics of the urban heat island of lodz, poland. *Atmospheric Environment 33* (1999), 3885–3895.

[56] Kolokotroni, M., and Giridharan, R. Urban heat island intensity in london: An investigation of the impact of physical characteristics on changes in outdoor air temperature during summer. *Solar energy 82*, 11 (2008), 986–998.

[57] Kolokotroni, M., Zhang, Y., and Watkins, R. The london heat island and building cooling design. *Solar Energy 81*, 1 (2007), 102–110.

[58] Koren, V., Schaake, J., Mitchell, K., Duan, Q.-Y., Chen, F., and Baker, J. A parameterization of snowpack and frozen ground intended for ncep weather and climate models. *Journal of Geophysical Research: Atmospheres (1984–2012) 104*, D16 (1999), 19569–19585.

[59] Landsberg, H. City climate. *General Climatology 3* (1981), 299–334.

[60] Landsberg, H. E. *The urban climate*, vol. 28. Academic press, 1981.

[61] Lee, D., Lee, J., and Wang, Z.-H. Urban climate. *Progress in Physical Geography 8* (1984), 1–31.

[62] Lei, M., Niyogi, D., Kishtawal, C., Pielke Sr, R., Beltrán-Przekurat, A., Nobis, T., and Vaidya, S. Effect of explicit urban land surface representation on the simulation of the 26 july 2005 heavy rain event over mumbai, india. *Atmospheric Chemistry and Physics 8*, 20 (2008), 5975–5995.

[63] Li, H., Sun, D., Yu, Y., Wang, H., Liu, Y., Liu, Q., Du, Y., Wang, H., and Cao, B. Evaluation of the viirs and modis lst products in an arid area of northwest china. *Remote Sensing of Environment 142* (2014), 111–121.

[64] Lockerby, R. W. *The Climate of Cities*. Vance Bibliographies, 1983.

[65] Lowry, W. P. Urban effects on precipitation amount. *Progress in Physical Geography 22*, 4 (1998), 477–520.

[66] Mahrt, L., and Ek, M. The influence of atmospheric stability on potential evaporation.

[67] Mahrt, L., and Pan, H. A two-layer model of soil hydrology. *Boundary-Layer Meteorology 29*, 1 (1984), 1–20.

[68] Maske, S., Nand, K., Behere, P., and Kachare, S. Characteristics of heat island at pune. *Prepublished Scienti" c Report*, 78112 (1978).

[69] Michael, M., Yadav, A., Tripathi, S., Kanawade, V., Gaur, A., Sadavarte, P., and Venkataraman, C. Simulation of trace gases and aerosols over the indian domain: evaluation of the wrf-chem model. *Atmospheric Chemistry and Physics Discussions 13*, 5 (2013), 12287–12336.

[70] Mohan, M., and Kandya, A. Impact of urbanization and land-use/land-cover change on diurnal temperature range: A case study of tropical urban airshed of india using remote sensing data. *Science of The Total Environment 506* (2015), 453–465.

[71] Mohan, M., Kandya, A., Battiprolu, A., et al. Urban heat island effect over national capital region of india: a study using the temperature trends. *Journal of Environmental Protection 2*, 04 (2011), 465.

[72] Mohan, M., Kikegawa, Y., Gurjar, B., Bhati, S., Kandya, A., and Ogawa, K. Assessment of urban heat island intensities over delhi. In *7th International Conference on Urban Climate* (2009), pp. 1–4.

[73] Mohan, M., Kikegawa, Y., Gurjar, B., Bhati, S., Kandya, A., and Ogawa, K. Urban heat island assessment for a tropical urban airshed in india.

[74] Mohan, M., Kikegawa, Y., Gurjar, B., Bhati, S., and Kolli, N. R. Assessment of urban heat island effect for different land use–land cover from

micrometeorological measurements and remote sensing data for megacity delhi. *Theoretical and applied climatology 112*, 3-4 (2013), 647–658.

[75] Morris, C., Simmonds, I., and Plummer, N. Quantification of the influences of wind and cloud on the nocturnal urban heat island of a large city. *Journal of Applied Meteorology 40*, 2 (2001), 169–182.

[76] Mukherjee, A., and Daniel, C. Temperature distribution over bombay during a cold night. *Indian J. Met. Hydrol. Geophys 27* (1976), 37–41.

[77] Nand, K., and Maske, S. Mean heat island intensities at delhi-assessed from urban climatological data. *Mausam 32* (1981), 269–272.

[78] National Aeronautics and Space Administration (NASA). `http://science-edu.larc.nasa.gov/energy_budget/`, 2014. Accessed: 2015-05-02.

[79] National Snow and Ice Data Center. `https://nsidc.org/data/modis/terra_aqua_differences`, 2005. Accessed: 2015-05-02.

[80] Ngie, A., Abutaleb, K., Ahmed, F., Darwish, A., and Ahmed, M. Assessment of urban heat island using satellite remotely sensed imagery: a review. *South African Geographical Journal 96*, 2 (2014), 198–214.

[81] Niyogi, D., Holt, T., Zhong, S., Pyle, P. C., and Basara, J. Urban and land surface effects on the 30 july 2003 mesoscale convective system event observed in the southern great plains. *Journal of Geophysical Research: Atmospheres (1984–2012) 111*, D19 (2006).

[82] Noilhan, J., and Planton, S. A simple parameterization of land surface processes for meteorological models. *Monthly Weather Review 117*, 3 (1989), 536–549.

[83] Oke, T. Towards a more rational understanding of the urban heat island. *Climat. Bull.(McGill) 5* (1969), 1–20.

[84] Oke, T. *Bibliography of urban climate 1977-1980*. World Meteorological Organization, World Climate Programme Department, 1983.

[85] Oke, T. R. *Review of urban climatology, 1973-1976*. Secretariat of the World Meteorological Organization Geneva, 1979.

[86] Oke, T. R. The energetic basis of the urban heat island. *Quarterly Journal of the Royal Meteorological Society 108*, 455 (1982), 1–24.

[87] Oke, T. R. Towards better scientific communication in urban climate. *Theoretical and Applied Climatology 84*, 1-3 (2006), 179–190.

[88] Oke, T. R., et al. Urban climatology and its applications with special regard to tropical areas. In *WMO*, vol. 652. WMO, 1986.

[89] Padmanabhamurty, B. Isotherms and isohumes in pune on clear winter nights: a mesometeorological study. *Mausam 80*, 1 (1979), 134–138.

[90] Padmanabhamurty, B., and Bahl, H. Isothermal and isohyetal patterns of delhi as a sequel of urbanization. *Mausam 35* (1984), 539–541.

[91] Pan, H.-L., and Mahrt, L. Interaction between soil hydrology and boundary-layer development. *Boundary-Layer Meteorology 38*, 1-2 (1987), 185–202.

[92] Pandey, A. K., Singh, S., Berwal, S., Kumar, D., Pandey, P., Prakash, A., Lodhi, N., Maithani, S., Jain, V. K., and Kumar, K. Spatio–temporal variations of urban heat island over delhi. *Urban Climate 10* (2014), 119–133.

[93] Pandey, P., Kumar, D., Prakash, A., Masih, J., Singh, M., Kumar, S., Jain, V. K., and Kumar, K. A study of urban heat island and its association with particulate matter during winter months over delhi. *Science of the Total Environment 414* (2012), 494–507.

[94] Patil, M., Kumar, M., Waghmare, R., Dharmaraj, T., and Mahanty, N. Evaluation of noah-lsm for soil hydrology parameters in the indian summer monsoon conditions. *Theoretical and Applied Climatology 118*, 1-2 (2014), 47–56.

[95] Patil, M., Waghmare, R., Halder, S., and Dharmaraj, T. Performance of noah land surface model over the tropical semi-arid conditions in western india. *Atmospheric Research 99*, 1 (2011), 85–96.

[96] Peng, S., Piao, S., Ciais, P., Friedlingstein, P., Ottle, C., Breon, F.-M., Nan, H., Zhou, L., and Myneni, R. B. Surface urban heat island across 419 global big cities.

[97] Peters-Lidard, C., Blackburn, E., Liang, X., and Wood, E. The effect of soil thermal conductivity parameterization on surface energy fluxes and temperatures. *Journal of the Atmospheric Sciences 55*, 7 (1998), 1209–1224.

[98] Peterson, T. C., and Owen, T. W. Urban heat island assessment: Metadata are important. *Journal of Climate 18*, 14 (2005), 2637–2646.

[99] Pitman, A. J., Narisma, G. T., Pielke, R., and Holbrook, N. Impact of land cover change on the climate of southwest western australia. *Journal of Geophysical Research: Atmospheres (1984–2012) 109*, D18 (2004).

[100] Rajeevan, M., Kesarkar, A., Thampi, S., Rao, T., Radhakrishna, B., and Rajasekhar, M. Sensitivity of wrf cloud microphysics to simulations of a severe thunderstorm event over southeast india. In *Annales Geophysicae* (2010), vol. 28, European Geosciences Union, pp. 603–619.

[101] Ramachandra, T., and Kumar, U. Greater bangalore: Emerging urban heat island. *GIS Development 14*, 1 (2010), 86–104.

[102] Rizwan, A. M., Dennis, L. Y., and Chunho, L. A review on the generation, determination and mitigation of urban heat island. *Journal of Environmental Sciences 20*, 1 (2008), 120–128.

[103] Roth, M. Review of atmospheric turbulence over cities. *Quarterly Journal of the Royal Meteorological Society 126*, 564 (2000), 941–990.

[104] Roth, M. Review of urban climate research in (sub) tropical regions. *International Journal of Climatology 27*, 14 (2007), 1859–1873.

[105] Roth, M., and Chow, W. T. A historical review and assessment of urban heat island research in singapore. *Singapore Journal of Tropical Geography 33*, 3 (2012), 381–397.

[106] Santamouris, M. Analyzing the heat island magnitude and characteristics in one hundred asian and australian cities and regions. *Science of The Total Environment 512* (2015), 582–598.

[107] Santamouris, M., Papanikolaou, N., Livada, I., Koronakis, I., Georgakis, C., Argiriou, A., and Assimakopoulos, D. On the impact of urban climate on the energy consumption of buildings. *Solar energy 70*, 3 (2001), 201–216.

[108] Shastri, H., Paul, S., Ghosh, S., and Karmakar, S. Impacts of urbanization on indian summer monsoon rainfall extremes. *Journal of Geophysical Research: Atmospheres* (2015).

[109] Singh, R., Dey, S., Tripathi, S., Tare, V., and Holben, B. Variability of aerosol parameters over kanpur, northern india. *Journal of Geophysical Research: Atmospheres (1984–2012) 109*, D23 (2004).

[110] Singh, R. B., Grover, A., and Zhan, J. Inter-seasonal variations of surface temperature in the urbanized environment of delhi using landsat thermal data. *Energies 7*, 3 (2014), 1811–1828.

[111] Slater, A., Bohn, T., McCreight, J., Serreze, M., and Lettenmaier, D. A multimodel simulation of pan-arctic hydrology. *Journal of Geophysical Research: Biogeosciences (2005–2012) 112*, G4 (2007).

[112] Smithson, P. Micro-and mesoclimatology. *Progress in Physical Geography 14*, 1 (1990), 97–108.

[113] Sodoudi, S., Shahmohamadi, P., Vollack, K., Cubasch, U., and Che-Ani, A. Mitigating the urban heat island effect in megacity tehran. *Advances in Meteorology 2014* (2014).

[114] Spittlehouse, D., and Black, T. Evaluation of the bowen ratio/energy balance method for determining forest evapotranspiration. *Atmosphere-Ocean 18*, 2 (1980), 98–116.

[115] Steinecke, K. Urban climatological studies in the reykjavık subarctic environment, iceland. *Atmospheric Environment 33*, 24 (1999), 4157–4162.

[116] Stewart, I. D. A systematic review and scientific critique of methodology in modern urban heat island literature. *International Journal of Climatology 31*, 2 (2011), 200–217.

[117] Stull, R. B. *Meteorology for scientists and engineers: a technical companion book with Ahrens' Meteorology Today*. Brooks/Cole, 2000.

[118] Sturman, A. P. Applied climatology. *Progress in physical geography 24*, 1 (2000), 129–139.

[119] Sundersingh, S. D. Effect of heat islands over urban madras and measures for its mitigation. *Energy and Buildings 15*, 1 (1991), 245–252.

[120] Tang, B., Bi, Y., Li, Z.-L., and Xia, J. Generalized split-window algorithm for estimate of land surface temperature from chinese geostationary fengyun meteorological satellite (fy-2c) data. *Sensors 8*, 2 (2008), 933–951.

[121] Tereshchenko, I., and Filonov, A. Air temperature fluctuations in guadalajara, mexico, from 1926 to 1994 in relation to urban growth. *International Journal of Climatology 21*, 4 (2001), 483–494.

[122] Thomas, G., Sherin, A., Ansar, S., and Zachariah, E. Analysis of urban heat island in kochi, india, using a modified local climate zone classification. *Procedia Environmental Sciences 21* (2014), 3–13.

[123] Thomas, G., and Zachariah, E. Urban heat island in a tropical city interlaced by wetlands. *Environmental Science and Engineering 5* (2011), 234–240.

[124] Tso, C. A survey of urban heat island studies in two tropical cities. *Atmospheric Environment 30*, 3 (1996), 507–519.

[125] Unger, J., Sümeghy, Z., and Zoboki, J. Temperature cross-section features in an urban area. *Atmospheric Research 58*, 2 (2001), 117–127.

[126] United Nations. Department of Economic and Social Affairs. Population Division. *World urbanization prospects: The 2014 revision*. UN, 2014.

[127] United Nations Statistics Division. Demographic yearbook. `http://unstats.un.org/unsd/demographic/products/dyb/dybsets/2013.pdf`, 2013. Accessed: 2015-05-02.

[128] Urankar, G., Prabha, T., Pandithurai, G., Pallavi, P., Achuthavarier, D., and Goswami, B. Aerosol and cloud feedbacks on surface energy balance over selected regions of the indian subcontinent. *Journal of Geophysical Research: Atmospheres (1984–2012) 117*, D4 (2012).

[129] Velazquez-Lozada, A., Gonzalez, J. E., and Winter, A. Urban heat island effect analysis for san juan, puerto rico. *Atmospheric Environment 40*, 9 (2006), 1731–1741.

[130] Waghmare, R., Dharmaraj, T., and Patil, M. Noah-lsm simulation on various soil textures in tropical semi-arid regions. *Soil Science 177*, 11 (2012), 664–673.

[131] Wan, Z. Modis land-surface temperature algorithm theoretical basis document (lst atbd). *Institute for Computational Earth System Science, Santa Barbara 75* (1999).

[132] Wong, K. V., Paddon, A., and Jimenez, A. Review of world urban heat islands: Many linked to increased mortality. *Journal of Energy Resources Technology 135*, 2 (2013), 022101.

[133] Yoshino, M. Development of urban climatology and problems today. *Energy and buildings 15*, 1 (1991), 1–10.

[134] Zhang, C. L., Chen, F., Miao, S. G., Li, Q. C., Xia, X. A., and Xuan, C. Y. Impacts of urban expansion and future green planting on summer precipitation in the beijing metropolitan area. *Journal of Geophysical Research: Atmospheres (1984–2012) 114*, D2 (2009).

[135] Zhang, P., Bounoua, L., Imhoff, M., Wolfe, R., and Thome, K. Comparing land surface and air temperature urban heat islands over the contiguous usa. In *AGU Fall Meeting Abstracts* (2013), vol. 1, p. 0441.

[136] Zhao, G., and Siebert, S. Season-wise irrigated and rainfed crop areas for india around year 2005, Jan 2015.

[137] Zhao, L., Lee, X., Smith, R. B., and Oleson, K. Strong contributions of local background climate to urban heat islands. *Nature 511*, 7508 (2014), 216–219.

[138] Zhou, Y., and Savijärvi, H. The effect of aerosols on long wave radiation and global warming. *Atmospheric Research 135* (2014), 102–111.